UNIVERSITY OF
Southampton

University of Southampton Research Repository

Copyright © and Moral Rights for this thesis and, where applicable, any accompanying data are retained by the author and/or other copyright owners. A copy can be downloaded for personal non-commercial research or study, without prior permission or charge. This thesis and the accompanying data cannot be reproduced or quoted extensively from without first obtaining permission in writing from the copyright holder/s. The content of the thesis and accompanying research data (where applicable) must not be changed in any way or sold commercially in any format or medium without the formal permission of the copyright holder/s.

When referring to this thesis and any accompanying data, full bibliographic details must be given, e.g.

Thesis: Author (Year of Submission) "Full thesis title", University of Southampton, name of the University Faculty or School or Department, PhD Thesis, pagination.

Data: Author (Year) Title. URI [dataset]

UNIVERSITY OF SOUTHAMPTON

Faculty of Engineering and Physical Sciences
Optoelectronics Research Centre

Diamond micromachining of photonic materials: dynamics and the limits of precision

by

Matthew D'Souza
MPhys
ORCiD: 0000-0002-0165-3244

A thesis for the degree of
Doctor of Philosophy

June 2025

University of Southampton

Abstract

Faculty of Engineering and Physical Sciences
Optoelectronics Research Centre

Doctor of Philosophy

Diamond micromachining of photonic materials: dynamics and the limits of precision

by Matthew D'Souza

This thesis investigates the ultra-precision diamond micromachining of brittle photonic materials, focusing on optimising machining processes to achieve high-quality surfaces for applications in optical and quantum devices. It explores the dynamics of physical machining in materials such as lithium niobate, silica, and silicon, which are crucial in photonics due to their optical properties. By physically machining within the ductile regime, chip-free surfaces were achieved, offering nanometre-scale roughness and high uniformity, without requiring costly post-processing. Ridge waveguides, optical facets, and alignment structures were fabricated with a focus on minimising surface roughness, form errors, and defects. Surface roughness measurements for ridge waveguide sidewalls reached as low as 0.16 nm when using a 100 µm square-profiled blade. The impact of feed rate on blade wear rate and resulting surface roughness was investigated over a range of 0.1 mm s^{-1} to 10 mm s^{-1}, revealing a critical shift at 2 mm s^{-1} in blade wear rate and a similar shift in surface roughnesses at 4 mm s^{-1} in lithium niobate. A comparison of blade wear, surface finish, and waveguide performance provides insights into deterministic machining.

A novel confocal probe-based scanner has been developed to profile the long-term variation of ridge waveguide uniformity, indicating an approximate 1.2 µm curvature across all of the ridge waveguides fabricated. A comparison of ridge waveguides fabricated with 300 µm and 100 µm wide dicing blades was performed, resulting in a significant improvement in optical conversion efficiency — an increase of 226% for the ridges machined with a 300 µm wide blade over a 100 µm wide blade. Plotting the accumulative width variation using the confocal probe traces reveals that the ridges machined with the 300 µm wide blade were significantly more consistent in their widths, confirming the cause of the improved optical conversion efficiencies.

The development of a novel 3D passive alignment structure based around machined U-Grooves and optical fibres has been proposed; however, due to inconsistent machine stepper backlash, practical success has been limited. V-Grooves and U-Grooves have been compared from a general coupling alignment perspective, with U-Grooves resulting in a 30% improvement in fibre-to-fibre alignment over an unsupported gap of 3 mm compared to V-Grooves. This has resulted in improvement of coupling efficiency from 97% to 99%.

Contents

List of Figures **ix**

List of Tables **xiii**

List of Additional Material **xv**

Declaration of Authorship **xvii**

Acknowledgements **xix**

1 Introduction and Motivation **1**
1.1 Synopsis 2
References 4

2 Background **7**
2.1 Microfabrication Overview 7
2.2 Ultra-Precision Machining 9
2.3 Physical Machining 10
2.3.1 Dicing 11
2.4 Ductile Machining 14
2.5 Lithium Niobate Ridge Waveguide Fabrication 15
2.6 Diamond Micro-Machining of Optical Materials 15
2.6.1 Lithium Niobate 16
2.6.2 Other Optical Materials 18
2.6.3 Machining Parameters 20
2.7 Conclusion 21
References 21

3 Metrology **29**
3.1 Introduction 29
3.2 Definitions 30
3.2.1 2D Surface Parameters 30
3.2.2 3D Surface Parameters 31
3.2.3 Filtering 31
3.2.4 Top Side Chipping 33
3.3 Equipment 35
3.3.1 Scanning Electron Microscopy 36
3.3.2 Coherent Scanning Interferometry 36

3.3.2.1 Limitations of CSI 37
3.4 Confocal Probe Scanner 39
3.4.1 Laser Confocal Probe 39
3.4.2 Principles of Confocal Chromatography 40
3.4.3 Confocal Scanner Development 42
3.4.4 Verification 46
3.4.4.1 Confocal probe artifacts 47
3.5 Conclusion 49
References 49

4 Machining Dynamics in Brittle Materials for Device Based Photonics 51
4.1 Introduction 51
4.2 Parameter Definitions 52
4.3 Evolution of Shape and Depth of Cut 53
4.3.1 Experimental Methodology 53
4.3.2 Results & Discussion 54
4.4 Blade Wear Rate as an Indicator of Ductile Physical Machining 59
4.4.1 Experimental Methodology 59
4.4.2 Results & Discussion 60
4.5 Conclusion 62
References 63

5 Machining for Photonic Waveguides 65
5.1 Introduction 65
5.2 Performance of Wide vs Narrow Blade Machined Ridge Waveguides . . 66
5.2.1 Nonlinear Frequency Conversion 66
5.2.1.1 Phase Matching 67
5.2.1.2 Waveguide Uniformity 68
5.2.2 Experimental 71
5.2.3 Results & Discussion 71
5.3 Conclusion 77
References 80

6 Machining for Precision Alignment 83
6.1 Introduction 83
6.2 Passive Alignment in Optics & Photonics 84
6.3 Assembly Principles 86
6.3.1 Fibre V & U-Grooves 87
6.4 Assembly Design & Discussion 88
6.5 Assembly Results 92
6.6 Assembly V vs U 94
6.6.1 Assembly Results 94
6.7 Swansea SWIFT Trap 97
6.7.1 Fabrication 97
6.7.2 Comparison of V- & U- Grooves 98
6.7.3 Conclusions 101
References 101

7 Conclusion & Outlook **107**

Appendix A Publications **111**
Appendix A.1 Journal Papers 111
Appendix A.2 Conference Publications 111

List of Figures

2.1 A limited comparison of the different dimension regimes of microfabrication techniques . . . 8

2.2 Taniguichi timeline of machining precision over the past century. The precision is defined as random + systematic errors. Based on [1–3] and extended. . . . 10

2.3 Annotated photos of the MicroAce 3 (top) and DAD 3430 (bottom) dicing saws. . . . 13

2.4 Chart displaying the ductile-brittle threshold on a representative stress-strain curve [12]. . . . 14

2.5 Schematic showing the process flow of ridge waveguide formation for the purpose of secondary harmonic generation; 1) Periodic poling is created in a lithium wafer 2) Formation of a planar guiding layer by indiffusion 3) Physical machining of ridges, facets and finally singulation into devices. . . . 16

3.1 Diagram indicating the 2D surface roughness parameters, Ra and Rq on an example surface with form removed. . . . 30

3.2 a) Raw sample surface data taken from a Zygo Zegage scan of a ridge waveguide sidewall b) Corrected of data removed by performing a plane fit removal, then a cylindrical fit removal . . . 32

3.3 Microscope image of ridge waveguide facet with an optical mode drawn on as representation. . . . 33

3.4 Diagram illustrating the advantage of a 45° scan over a pixelized horizontal cut scan. The red dashed lines represent the line of best fit for the data. a) Horizontal Edge Scan: In this case, the physical edge falls between pixels, resulting in a poor line of best fit. b) Rotated Edge Scan: Here, the pixels align more accurately with the edge, providing a better line of best fit and a more precise estimate of the chipping area. . . . 34

3.5 Diagram displaying the top side chipping processing method. a) A pixel bitmap of a chipped edge. b) A line is fitted to the average edge gradient of multiple scans. c) The edge line is fitted to the specific edge of the current scan. d) The number of missing pixels below the line and to the left of the edge are marked (blue) and counted. This is is then converted to an area missing per unit length statistic for the current scan. . . . 35

3.6 a) Labelled schematic of a Mirau interferometer based CSI tool. In Michelson based CSI, the reference mirror is positioned next to the beam splitter, rather than within the objective. b) An interferogram representation of a line through the surface. Various algorithms can be used to fit the interferogram; peak value, envelope convolution or phase convolution c) The obtained surface profile of the scan. 37
3.7 a) b) A height map of the diffraction artifact, characterised by the blue band along the edges c) A line trace of the diffraction artifact. 38
3.8 a) Grey scale image of the resulting batwing artifact bands. b) Heightmap of the batwing artifacts, the red bands indicating the batwing artifact location. c) A line trace of the batwing artifact, characterised by the sudden peak drops on either side (points A and B), indicating a phase-shift. . . . 38
3.9 Photograph of the confocal scanner setup. The schematic is displayed in Figure 3.12 40
3.10 Labelled schematic displaying the laser point probe setup 41
3.11 Labelled schematic displaying the principles of confocal chromatography 41
3.12 Schematic of the travelling confocal probe. 42
3.13 Diagram indicating the reported data of the confocal probe per exposure sample. 43
3.14 Example data from a confocal scan line across four cuts, two made with a 100 µm blade and two with a 300 µm blade, resulting in two waveguide ridges. 44
3.15 Confocal line trace with up (red) and down (blue) edge points marked. Each edges will have multiple up and down points. 44
3.16 Diagram displaying how up and down points are processed for a typical step down edge. Starting from the left-most Down point, all of the Downs within a set distance are averaged over in both X and Y axes to get the a single edge location location with standard errors. This is repeated for the following Up points, allowing for pairing to be carried out. 45
3.17 An example topographical map with data provided by the confocal probe. This consists of a line of edge points. The gap in the middle represents a section where the software could not match the column of points to a set of lines due to dirt on the sample, resulting in missing data. 45
3.18 Figure displaying the precision graticule grid shape. The lines in blue were the profiled lines to obtain the stage squareness. 46
3.19 Charts displaying the scanned points of the graticule. Orange and blue represent the Y and X lines (relative to the stage axes) respectively, with each point consisting of multiple x and y edge positions. 47
3.20 Line trace of a confocal probe step scan indicating the confocal artifacts resulting from optical effects. a) Diffraction over top edge with a preference for blue light. b) Scattering from bottom edge and sidewall with a red light preference 48

4.1 Illustration of the trench shape evolution quantification. 52
4.2 Grayscale image of a ”w” worn blade cut. The red line is drawn on to illustrate the ”w”. 53
4.3 Microscope images of a square (left) and round (right) machined trenches 54

4.4 Chart displaying the evolution of cut depth over 10 m of machining distance for the initially 100 µm deep square and round, and the 50 µm deep square and round blades. 55
4.5 Chart displaying the evolution of cut width over 10 m of machining distance for the initially 100 µm deep square and round, and the 50 µm deep square and round blades. 56
4.6 Chart displaying the evolution of squareness width over 10 m of machining distance for the initially 100 µm deep square and round, and the 50 µm deep square and round blades. 56
4.7 Chart displaying the evolution of cut symmetry over 10 m of machining distance for the initially 100 µm deep square and round, and the 50 µm deep square and round blades. 57
4.8 Chart displaying the evolution of cut "W-ratio" over 10 m of machining distance for the initially 100 µm deep square and round, and the 50 µm deep square and round blades. 58
4.9 Schematic of vertical and horizontal Ra and Rq measured on a ridge waveguide. 59
4.10 Chart displaying the roughness and blade wear rate for a range of machining feed rates for lithium niobate. 60
4.11 Chart displaying the roughness and blade wear rate for a range of machining feed rates for silicon. 61
4.12 Chart displaying the blade wear rate for a range of machining feed rates for silica. 62

5.1 a) Phasor diagrams indicating the energy transfer direction and magnitude as a result of phase matching, quasi phase matching and no-phase matching. b) Chart displaying the resulting SHG intensity as a result of the three phasors displayed in a). c) Corresponding poling diagram for the phase matching in b). 68
5.2 Diagrams displaying the modelled waveguide shapes by Gray. a) is the ideal 6.8 µm wide ridge waveguide, b) is a linear width variation and c) is a parabolic curve. Taken from [8] 69
5.3 Charts displaying Grays modelled resulting phase matching spectra [8]. The left and right columns represent the linear width variation and the parabolic curve respectively, as displayed in e) and f). $\delta\beta$ represents the width change along the length. Two maximum width variations are modelled per shape variation, the top spectra consider a 60 nm variation, and the middle spectra represent 540 nm variation. 70
5.4 Labelled microscope image of 100 µm and 300 µm kerf blade machined ridge waveguides. The facets are machined at 7° to minimise coupling losses by enabling a wider angle of acceptance relative to the input beam [10]. 72
5.5 Schematic of the experimental setup for the wide vs narrow temperature sweeps. 73
5.6 Chart displaying the resulting fundamental to fundamental phase matching efficiency vs temperature waveguide sweeps. Left column is the absolute efficiency. The right is normalised efficiency for the purpose of spectra comparison. Data collection performed by Noelia Palomar Davidson. 74

5.7 Width uniformity along the length of the working ridge waveguides (1-3). A rolling average over 30 points is used to smooth the points for analysis. Data obtained with the confocal scanner. 75
5.8 Chart of accumulative width variation along the waveguide lengths. . . 76
5.9 Chart of straightness along the length of the working ridge waveguides (1-3). A rolling average over 30 points is used to smooth the points for analysis. 0 represents the mean y position of the ridge. Data obtained with the usage of the confocal scanner. 78
5.10 Chart displaying the chipping results for the three wide vs narrow blade cut data. Starting at approximately 2 mm from the start of the waveguide, with sites evenly spread out along the length of the waveguide. Top and bottom represent the relative sides of the waveguide to indicate differences between the blade cuts. 79
5.11 Diagram displaying the CSI scan sites for Table 5.1. 80

6.1 Diagram displaying the key principle of the passive alignment using fibre dowels in U-Grooves to align components to a base-plate 87
6.2 Schematic displaying the principles of an optical-fibre in a V-Groove and a U-Groove. The top row displays the idealised U- and V-Grooves, with the bottom row displaying fibres sat in worn U- and V-Grooves. The dashed line indicates the initial position of the fibre in the V-groove indicating a displacement, whereas the fibre on top U-Groove fibre remains fixed in place. 89
6.3 U-grooves in a "n" (top) and "T" (bottom) layout, as highlighted in green. 89
6.4 Fabrication steps of the passive alignment platform. Red dashed lines are machined grooves and the green dashed line is a singulation cut. a) Initial U-grooving step for creating the 3D lateral alignment features b) Fibre array component fabrication for alignment testing c) Fibre array construction d) Singulation of fibre array e) Reconstruction of fibre array to test alignment platform 91
6.5 Diagram displaying the two relevant offsets for the parallel equation in Equation 6.1 92
6.6 Diagram displaying the angles discussed in Table 6.4. 96
6.7 Schematic of the Swansea SWIFT trap fabrication process. a) A hexagon is singulated out of a silicon wafer b) U-Grooves or V-Grooves are machined into the surface c) A hole is milled in the middle for trapping purposes. 98
6.8 Schematic of the Swansea trap U-Groove vs V-Groove comparison setup. The numbers indicate the entry/exit pair of the butt-coupled fibre. . . . 99
6.9 Photo of the Swansea swift trap alignment rig. The left and right power meters are the reference and signal fibres respectively. 99

List of Tables

2.1 Table of physical machining parameters in optical materials 28

4.1 Table displaying the average surface roughness of initially both 100 µm and the 50 µm square machined trenches. See Figure 4.9 for measurement schematic. 58
4.2 Table displaying the mean chip density for initially 100 µm and 50 µm round and square 58

5.1 Table of the average sidewall roughness (Sq) of the 300 and 100 µm machined ridges. The ridge values are the ridge sidewall values, the non-ridge are the opposing sides of the same cut for comparison as displayed in Figure 5.11. 80

6.1 Table displaying notable alignment test results of the assembly. 93
6.2 Table displaying the results of the V-Groove vs U-Groove transmission tests. NA represents sufficient mode to mode offset that no coupling was possible. 95
6.3 Table of the RMS deviation from the nominal position and end to end slope variation relative to the first trench. 96
6.4 Table of alignment errors in the assembly measured by the confocal probe, 1-4 represent the positions drawn in Figure 6.6. 97
6.5 Table displaying the butt-coupled U vs V groove fibre transmission results. Due to the assumptions made, the parallel offsets are the upper bound, and the true offset may be better. 100

List of Additional Material

Dataset supporting this work: https://doi.org/10.5258/SOTON/D3547

Declaration of Authorship

I declare that this thesis and the work presented in it is my own and has been generated by me as the result of my own original research.

I confirm that:

1. This work was done wholly or mainly while in candidature for a research degree at this University;
2. Where any part of this thesis has previously been submitted for a degree or any other qualification at this University or any other institution, this has been clearly stated;
3. Where I have consulted the published work of others, this is always clearly attributed;
4. Where I have quoted from the work of others, the source is always given. With the exception of such quotations, this thesis is entirely my own work;
5. I have acknowledged all main sources of help;
6. Where the thesis is based on work done by myself jointly with others, I have made clear exactly what was done by others and what I have contributed myself;
7. None of this work has been published before submission

Signed:.. Date:..................

Acknowledgements

Firstly, I would like to thank my supervisors, James Gates, Paul Gow, Corin Gawith, and Peter Smith, for their support and many opportunities throughout. Your guidance and encouragement, both academically and personally, have been greatly appreciated over the past few years.

A special thank you goes to Glenn Topley - your patience in the lab, our conversations, and your constant willingness to help have meant a great deal to me.

Thank you to the wider OEQP group and other members in the department for your help with equipment, experiments, listening to my grumbling about failed experiments, entertainment, and laughter along the way.

To my friends in Southampton and beyond, thank you for your unwavering support, for the much-needed social distractions, and for making the PhD experience truly enjoyable.

Lastly, I would like to thank my family, especially my parents, for their endless encouragement and support throughout my life.

Thank you to everyone who has made this journey an enjoyable and memorable one.

Chapter 1

Introduction and Motivation

Ultra-precision diamond micromachining of brittle crystalline materials has become a topic of growing interest in optics and quantum fabrication research in recent years. This technique enables the fabrication of centimeter-scale structures with nanometer-scale roughness, which are difficult to achieve through etching or cleanroom processes. It also bypasses certain limitations, such as byproduct contamination generated by etching as in lithium niobate ridge waveguide fabrication [1, 2], the inability to etch resistant materials, or being restricted to etching along crystal axes [3, 4], allowing for machining of arbitrary shapes. However, unlike in the semiconductor industry, where silicon is a universal material, no equivalent exists in photonics. As a result, multiple crystalline materials must be considered, each with significantly different physical properties. As device sizes shrink and tolerances tighten, the demand for high-quality surfaces, free from defects such as cracks or chips, has dramatically increased. In particular, machining processes for brittle materials like lithium niobate, silicon, and silica must maintain structural integrity. Machining brittle materials requires processing in the ductile regime, which enables plastic deformation up to the material's yield point, thereby providing a chip-free finish [5].

There are three primary research areas of interest in optical and photonic machining due to their importance in device fabrication: alignment, waveguides, and facets. The alignment of the tool with the workpiece is critical and influences the other two areas. Many optical and photonic devices have extremely small alignment tolerances from both a machining and component perspective, especially as miniaturisation progresses. Waveguides provide a path for high-intensity light propagation and can enable high-efficiency nonlinear processes; however, stringent requirements are placed on waveguide uniformity [6–8]. Facets have been physically machined successfully in several crystalline materials, including lithium niobate [9, 10], $KTiOPO_4$ [11], and Nd:YAG [12]. However, many other crystalline materials still need to be machined with sufficiently low surface roughness and increasingly tight form consistencies.

The fabrication of ridge waveguides in lithium niobate has attracted the most attention because of the material's high optical transparency and nonlinear optical properties. Previous work by Carpenter demonstrated that physical machining could be performed on the brittle material silica in the ductile regime, enabling chip-free material removal and producing smooth surfaces. For silica, surface roughness values of $\leq$ 14 nm Sa were reported [13], while for lithium niobate, Carpenter et al. achieved a significantly lower roughness of 0.29 nm Sa [9]. This exceptionally low roughness is comparable to results obtained by etching, which is one of the reasons why Covesion Ltd., a University of Southampton spin-out focusing on lithium niobate non-linear ridge waveguides, utilises dicing saws to machine optical waveguides and facets. Building on this work, this research focuses on improving the uniformity of lithium niobate ridge waveguides, utilising their non-linear characterisation processes for optical testing.

The motivation for this work lies in the need to develop reliable, reproducible methods for machining brittle materials, such as silicon, sapphire and lithium niobate, that meet the stringent demands of modern photonic device fabrication, while minimising energy consumption and reducing costly cleanroom processes [14–16]. Prior work has largely demonstrated proof-of-concept dicing of lithium niobate ridge waveguides with limited focus on achieving deterministic manufacturing efficient devices at scale. This work aims to address that gap by enabling the deterministic machining of brittle materials with sub-nanometre surface roughnesses and tight uniformity, specifically, dimensional deviations of less than 0.1 µm over tens of millimetres. Achieving this level of control will enable the creation of high-performance waveguides and other photonic components that are crucial for telecommunications, sensing, and quantum applications.

This thesis focuses on the exploration and optimisation of ductile machining in brittle materials, with a primary emphasis on lithium niobate ridge waveguides. However, materials such as silicon and silica are also discussed. By investigating machining parameters, this research contributes to the body of knowledge on ultra-precise physical machining, offering insights into how to advance towards deterministic machining of brittle materials while addressing the limitations of the dicing machines used in this work.

1.1 Synopsis

Chapter 2 provides an overview of microfabrication techniques, with a special focus on physical machining. It introduces physical machining using a dicing saw, emphasising the growing interest in photonic and optical fabrication, particularly in lithium niobate. Ridge waveguides are introduced, with an outline of the generic

fabrication steps. The concept of ductile machining of brittle materials is also presented. Additionally, the chapter reviews the physical machining of other optical materials, highlighting the current limitations of this fabrication method, primarily issues with uniformity defects.

Chapter 3 explores the metrology techniques used throughout this work. It introduces key 2D and 3D surface parameters, such as surface roughness and peak-to-valley measurements, alongside the metrology equipment utilised. Coherent scanning interferometry (CSI) and confocal chromatic probes are discussed, with an explanation of their measurement limitations. The development and verification of a confocal probe scanner for large-scale profiling of machined features is also examined.

Chapter 4 discusses the dynamics of machining brittle materials, such as lithium niobate, silicon, and silica, in the context of achieving smoother and more uniform ridge waveguides and optical facets. It examines the evolution of cut shapes and surface roughness during extended machining, introducing parameters to quantify the shape. Blade wear rates and surface roughness are compared to identify a possible link between wear rates and ductile machining.

Chapter 5 investigates the nonlinear optical conversion performance of wide and narrow-blade machined ridge waveguides and compares these to waveguide uniformity. The chapter introduces accumulative width variation as a quality factor affecting the effective refractive index and phase matching. It also compares the subsurface damage between polished and machined facets, discussing photorefractive damage and surface roughness.

Chapter 6 explores the utilisation of physical machining for precision alignment in optical and photonic devices. A review of different assembly designs is presented, followed by an examination of a novel platform based on the use of optical fibres in U-grooves for 3D alignment of components. The limitations of physical machining in this context are discussed. A detailed comparison of U-groove and V-groove alignment precision and the resulting transmission efficiencies is also provided, with applications in an atom trap as part of a collaboration with Swansea University.

The final chapter summarises the findings from this research and outlines areas for future work. It emphasises the need for further optimisation of physical machining parameters and blade selection, particularly for non-lithium niobate materials. The importance of addressing these challenges and gaining a deeper understanding of blade evolution for deterministic machining of optical features and photonic devices is highlighted.

References

1. Chen G, Li N, Ng JD, Lin HL, Zhou Y, Fu YH, Lee LYT, Yu Y, Liu AQ, and Danner AJ. Advances in lithium niobate photonics: development status and perspectives. Advanced Photonics 2022; 4:34003–3
2. Qi Y and Li Y. Integrated lithium niobate photonics. Nanophotonics 2020; 9:1287–320. DOI: doi:10.1515/nanoph-2020-0013
3. Pal P and Sato K. A comprehensive review on convex and concave corners in silicon bulk micromachining based on anisotropic wet chemical etching. Micro and Nano Systems Letters 2015; 3:1–42
4. Hedlund C, Strandman C, Katardjiev I, Bäcklund Y, Berg S, and Blom HO. Method for the determination of the angular dependence during dry etching. Journal of Vacuum Science & Technology B: Microelectronics and Nanometer Structures Processing, Measurement, and Phenomena 1996; 14:3239–43
5. Bifano TG, Dow TA, and Scattergood RO. Ductile-Regime Grinding: A New Technology for Machining Brittle Materials. Journal of Engineering for Industry 1991 May; 113:184–9. DOI: 10.1115/1.2899676
6. Gray AC. Nonlinear optical components and systems for quantum technologies and communications. en. PhD thesis. Zepler Institute for Photonics and Nanoelectronics, 2021 :184
7. Chauvet M, Henrot F, Bassignot F, Devaux F, Gauthier-Manuel L, Pêcheur V, Maillotte H, and Dahmani B. High efficiency frequency doubling in fully diced $LiNbO_3$ ridge waveguides on silicon. Journal of Optics. 2016 Jul; 18. Publisher: IOP Publishing:085503. DOI: 10.1088/2040-8978/18/8/085503
8. Santandrea M, Stefszky M, and Silberhorn C. General framework for the analysis of imperfections in nonlinear systems. Optics Letters 2019 Nov; 44:5398–401. DOI: 10.1364/OL.44.005398
9. Carpenter L, Berry S, and Gawith C. Ductile dicing of $LiNbO_3$ ridge waveguide facets to achieve 0.29 nm surface roughness in single process step. Electronics Letters 2017; 53. eprint: https://onlinelibrary.wiley.com/doi/pdf/10.1049/el.2017.2863:1672–4. DOI: 10.1049/el.2017.2863
10. Suntsov S, Rüter CE, Brüske D, and Kip D. Watt-level 775 nm SHG with 70% conversion efficiency and 97% pump depletion in annealed/reverse proton exchanged diced PPLN ridge waveguides. Optics Express. 2021 Apr 12; 29. Publisher: Optical Society of America:11386–93. DOI: 10.1364/OE.416723

11. Vernay A, Boutou V, Boutou V, Félix C, Jegouso D, Bassignot F, Chauvet M, Boulanger B, and Boulanger B. Birefringence phase-matched direct third-harmonic generation in a ridge optical waveguide based on a $KTiOPO_4$ single crystal. Optics Express. 2021 Jul 5; 29. Publisher: Optical Society of America:22266–74. DOI: 10.1364/OE.432636
12. Zha H, Yao Y, Wang M, Chen N, Zhang L, Bai C, Liu T, Ren Y, and Jia Y. Bending 90° Waveguides in Nd:YAG Crystal Fabricated by a Combination of Femtosecond Laser Inscription and Precise Diamond Blade Dicing. Crystals. 2023 Jan 20; 13:188. DOI: 10.3390/cryst13020188
13. Carpenter L. Precision dicing and micromilling of silica for photonics. PhD thesis. University of Southampton, 2013 Oct. 210 pp.
14. Aurich J, Linke B, Hauschild M, Carrella M, and Kirsch B. Sustainability of abrasive processes. CIRP Annals 2013; 62:653–72
15. Schneider F, Das J, Kirsch B, Linke B, and Aurich JC. Sustainability in ultra precision and micro machining: A review. International Journal of Precision Engineering and Manufacturing-Green Technology 2019; 6:601–10
16. Levy JM, Ohadi MM, and Kyosung C. Energy analysis of cleanrooms in an academic research building. ASHRAE Transactions 2015; 121:71–84

Chapter 2

Background

This chapter will begin with a general overview of microfabrication, then the limitations involved in each process. Physical machining will then be explored, before performing a review of current literature in the context of physical machining of optical and photonic devices.

2.1 Microfabrication Overview

Microfabrication is typically defined as fabricating structures on a micron scale or smaller, hence most cleanroom based fabrication processes are classed as microfabrication. There are several different microfabrication techniques, including lithography & etching, scanning tunnelling microscopes, laser processing and physical machining. A somewhat crude attempt to compare the critical dimension with feature depth and device size is carried out in Figure 2.1. This ignores aspect ratios, material types, form expectations and some other details. The next section will discuss how these techniques operate, then briefly compare them:

- Lithography (Electron beam lithography or photo-lithography) and etching are heavily used in the semiconductor industries and are used to pattern complicated electronic circuits on silicon wafers with high yields. These methods have largely been borrowed for the fabrication of integrated optics. Typically for photolithography, photoresist is deposited onto the substrate, then placed under a mask and lens array. The photoresist is exposed to UV light through the mask, and is then developed to remove the exposed photoresist areas for positive photoresist, or masked areas for negative resist. Etchants (wet or dry) are then used to etch away the exposed surface, then the developed photoresist is washed off with solvents. For electron beam lithography, the

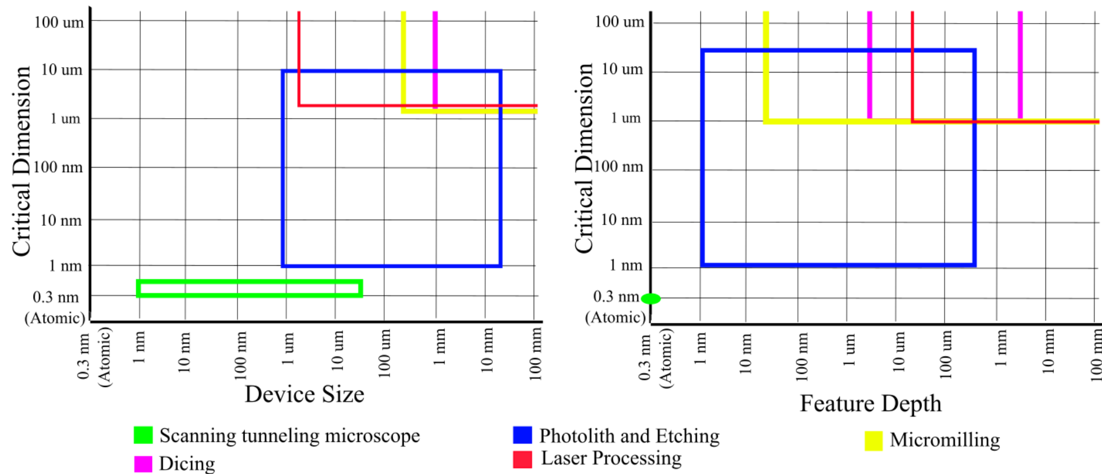

FIGURE 2.1: A limited comparison of the different dimension regimes of microfabrication techniques

shapes are drawn directly onto a electron-sensitive resist, allowing for nanometer precision, albeit at a cost of throughput

- Scanning tunnelling microscopes (STM) can move individual atoms around by using an ultrasharp conductive tip and electron tunnelling. The tip is scanned close to the conductive surface (typically ≤ 1 nm) where the electron clouds overlap. A voltage is applied, and the electron tunnelling effect takes place. There is a feedback loop in place, and this can be checked to map out the surface or controlled to pick up individual atoms/molecules. This allows atomic level precision and experimentation, however, has extremely high stability requirements, as well as very low throughput and limited device size.

- Laser ablation is the process of removing material from the surface of a substrate by surface irradiation. A laser with a suitable wavelength, intensity and pulse length for the target material is selected. The material absorbs the energy and either sublimates, evaporates, or ablates. This process is highly limited to removing material in Gaussian shapes, and if the material is not perfectly pure or uniform in density, the resulting hole may be distorted or be coated in residue.

- Physical machining is the process of using a physical tool, such as a diamond, to remove material, and is expanded upon later in this chapter.

As shown in Figure 2.1, while STM moves individual atoms with angstrom resolution, it is limited in terms of usable dimensions, especially feature depth. The STM feature depth is limited because no method currently exists for 3D stacking of individual atoms. Lithography and etching can have a feature depth of a few nm, but is also limited in critical dimension to a few 10s of nm on this scale. The critical dimensions and feature depth are linked somewhat proportionally. The reason

photolithography/etching can obtain such precise features is because the masks are fabricated with e-beam lithography processes, which provides the lateral accuracy, and the depth is controlled by the etchant deposition. However, there is an aspect ratio to consider with critical dimension and depth/device size. The smaller the required critical dimension, the smaller the feasible device size and depth becomes.

Whereas dicing, micromilling and laser ablation device sizes are only limited to the bed sizes (typically limited to the standard wafer dimension - 6 to 8 inch) and are not as restricted by depth either. This comes with the cost of limited critical dimensions of typically 1 μm due to bed/tool positioning accuracy and material brittleness. Another geometrical limitation is the tool or laser spot dimensions, which places a size limit on the removed material. Micromilling and laser processing are much deeper, only limited by the cutter length, laser rayleigh range and translation stages. But dicing depths are usually limited to 2 mm for standard diameter dicing blades. It is possible to go up to 4-5 mm, however there is typical width to depth aspect ratio recommendation of 1:10 (metal bonded blades are typically 1:15 to 1:20) to prevent blade bending and breakage. There are other considerations for the method suitability for the use case, such as material type, machine stability, limited shapes, dimensionality etc.

Utilisation of physical machining enables smooth features across a large variety of dimensions as illustrated in Figure 2.1, with high repeatability and accuracy, albeit with form restrictions due to tooling shapes and sizes. One aim of this work is to demonstrate and develop ultra-precision physical machining as a complementary technique for chip-based photonics.

2.2 Ultra-Precision Machining

Ultra-precision machining (UPM) is defined here as being able to fabricate features with a sub-micron geometry tolerance. Geometry includes depth, roughness, and accuracy. Though there are other definitions for UPM, such as Taniguichis [2], where UPM is defined as the current widespread state of the art for absolute accuracy. He produced a timeline, Figure 2.2, that shows the (mainstream) historical progress of UPM (according to his definition), normal machining (industrial metal mills, lathes etc) and high precision machining, which unfortunately does not have a definition, but lies between the ultra and normal machining.

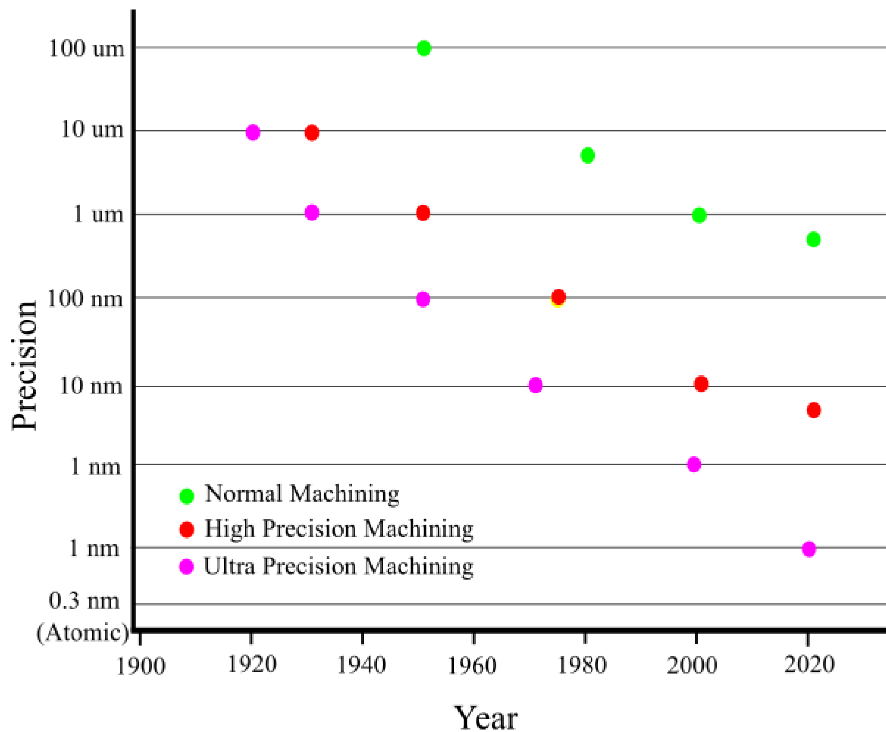

FIGURE 2.2: Taniguichi timeline of machining precision over the past century. The precision is defined as random + systematic errors. Based on [1–3] and extended.

2.3 Physical Machining

While physical machining is commonly used in the fabrication of optics, mostly by single point diamond turning (SPDT) for lens manufacturing, it is not widely used in photonic fabrication, especially not for chip-based photonics. The modern concept of physical machining (more generally known as conventional machining) is the controlled removal of material by the relative motion and contact of a tool on a workpiece. This is usually automated but some hand powered tools such as lathes and mills are still utilised. The controlled aspect is usually motion along the Cartesian axes (X,Y,Z), relative to the tool. Typically, the workpiece is moved relative to the tool, such as in mill or lathe based systems. This is for mechanical stability and practicality reasons, such as the spindle stability. Some mills have 6 degrees of freedom and as such can perform near 3D removal of material. Most physical machining tools have computerised assistance to make full use of the degrees of freedom since the required level of manual control is unpractical especially at the high speed/precision required for large-scale industrial fabrication.

Non-conventional machining is where the tool does not come into contact with the workpiece surface i.e. laser ablation, (abrasive) water machining. This often has advantages in stability and tool precision, since the tools are not rotating at high velocities therefore reducing vibrational effects and the lack of tool wear enables high

consistency but non-conventional tooling can be problematic from a roughness or form perspective.

The main benefit of physical machining is that it can obtain sub-micron features and optically smooth (sub nanometre roughness) surfaces over relatively large distances than other processes such as etching or photolithography. Physical machining can also be used on materials that are difficult for standard cleanroom processes, which is one reason why Covesion Ltd. use physical machining for defining lithium niobate waveguides. Physical machining opens possibilities for applications in various areas in photonics, in non-standard materials. Another benefit is that cleanrooms are typically not required for physical machining processes which reduces costs and fabrication complexity significantly, and has better sustainability as a result of the reduced energy consumption and by-products [4–6]. Dicing is especially of interest, due to a more tolerant geometry for tool wear and maintenance of sharpness and shape of the blade.

The two main disadvantages of physical machining are that the tool wears non-linearly, reducing form consistency significantly and that stiffness and vibrational damping are critical. Assuming the tool is dressed correctly, there will be a transient stage [7, 8] where the wear is high (shape changes rapidly and roughness falls), then a steady state where the resulting surface roughness is low, and the resulting form should not be changing significantly. Then a period of rapid degradation due to clogging or breakage. If the tool is well designed (i.e resin bonded blades), it may self-sharpen, and may keep cutting for a long time with minimal effect on roughness and wear rates. A dicing blade will generally perform in this manner, with a heavy material dependency due to the varying blade compositions used. If this is understood, it is possible to set the machining parameters and change them as the tool wears to obtain the desired form. This is known as deterministic machining. An in-depth understanding of tooling, dynamics, parameters, and the material is required to truly make use of deterministic physical machining.

This thesis heavily focused on physical machining performed with dicing saws. This is due to their widespread availability and hence near-term impact that this work can have in photonics. However, much of the insights from dicing-base physical machining can be applied to other geometries such as milling.

2.3.1 Dicing

Dicing originates from the semi-conductor industry in 1970s, where it is used with great success to for singulation of wafers of silicon electronic chips into semiconductor dies after scribing and cracking was no longer deemed efficient enough for wafer yields. Dicing was borrowed by the photonic industry for dicing gallium arsenide

wafers for the production of LEDs soon after, then various other wafer based devices. To the Authors' knowledge, it was not until 2000 where the dicing saw was first used to define ridge waveguides in literature, demonstrating other uses of a dicing saw [9]. This work was built on significantly, resulting in an active area of research that also has significant technological and commercial interest. Due to the the word "dicing" having a connotation of cutting through wafers entirely, within this work, it will refer to non-singulation cuts as physically machined trenches.

Dicing can be likened as a high precision automatic small table saw. This work had access to two dicing machines for this work, imaged in Figure 2.3, both fundamentally operate identically. There is a high speed, high stability air-bearing spindle typically mounted on a two stage stepper screw for z height positioning and a separate mechanical slider for y positioning of the dicing blade. The blade is mounted onto a spindle by a hub (or can be mounted onto a hub permanently) and is clamped in place by lock-rings and spacers. A dicing blade is composed of pieces of diamond grit with knoop hardness values of 8000 $\mathrm{kg_f\,mm^{-2}}$ [10]. This diamond grit is significantly harder than the lithium niobate (630 to 800 $\mathrm{kg_f\,mm^{-2}}$ [11]) and silicon (1000 - 1400 $\mathrm{kg_f\,mm^{-2}}$) studied in this work enabling efficient removal of material. The individual pieces of grit are held in a softer binder, typically nickel, zinc or resin, enabling worn diamond pieces to fall out of the blade exposing fresh diamond. The binder also wears down, creating voids known as pores enabling efficient material removal. [12].

The x and θ axes are provided by a vacuum chuck mounted onto a mechanical or air slider. Historically this has been mechanically driven, though some commercial dicing saws have recently become direct driven, increasing precision and repeatability. The sliders of the dicing saws used in this work are mechanically driven. The typical steps for the dicing (after setup) are that the y axis is moved to a specific point, spindle activated and brought down to the required depth of cut with the z stepper, then the slider moves the workpiece under the blade, trenching a line into the workpiece removing material. This is repeated and the bed rotated as required by the program.

There are two dicing machines available within the ORC, a Loadpoint MicroAce 3 and a Disco DISCO Automatic Dicer (DAD) 3430. The Loadpoint MicroAce 3 is an old but still serviceable machine, based on standard motors and traditional bearing based sliders. The Y axis encoder is rated to 2 µm, with manual rotation control for alignment. The DISCO DAD 3430 is a significantly newer commercial system based on a superior stiffness air slider, with steppers on all 4 axes, allowing for finer control with better positioning precision, being specified to 0.1 µm. This work shall primarily use the DAD 3430 for physical machining due to most work in literature being based on DISCO DAD systems, i.e [13–19].

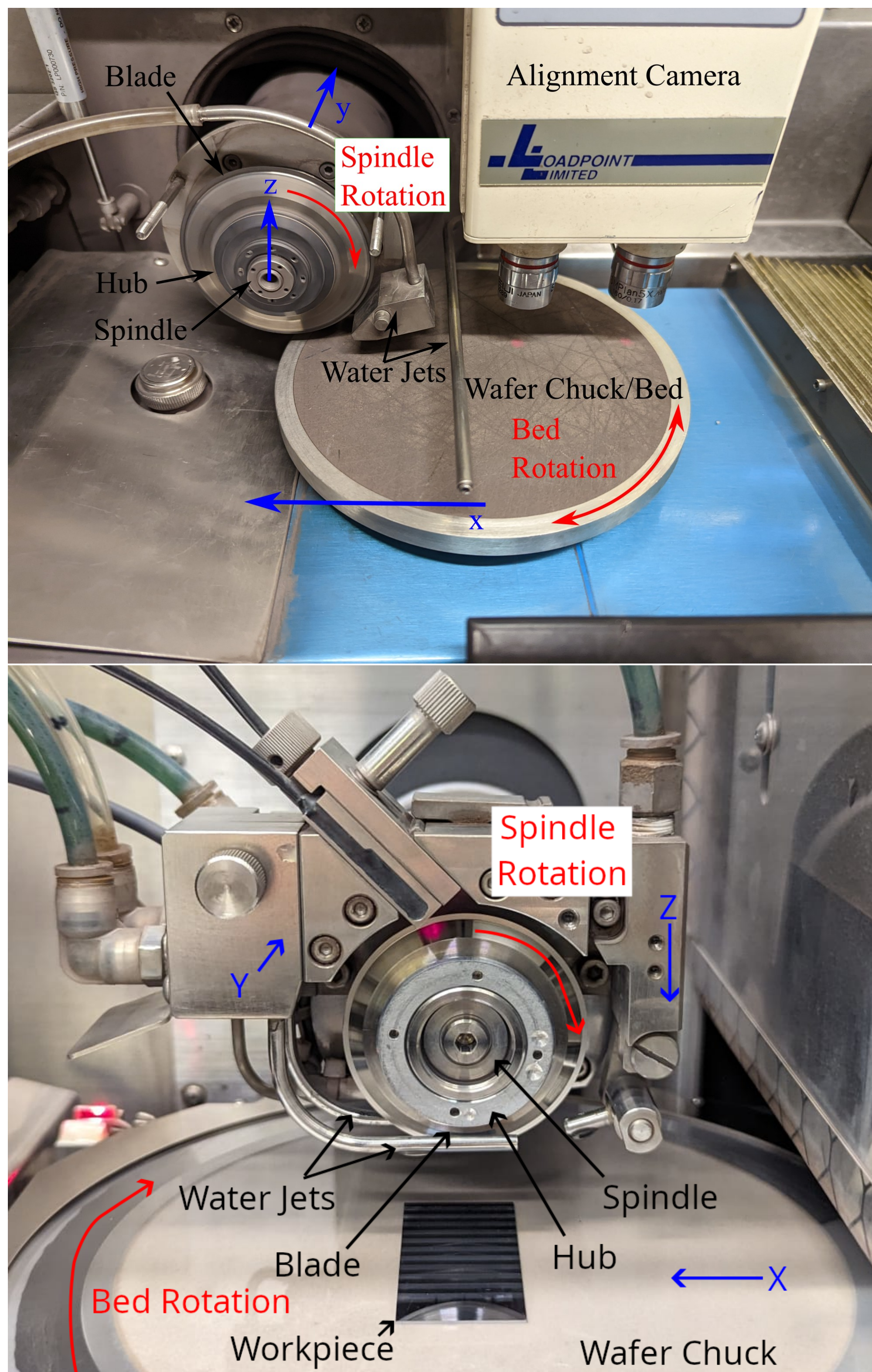

FIGURE 2.3: Annotated photos of the MicroAce 3 (top) and DAD 3430 (bottom) dicing saws.

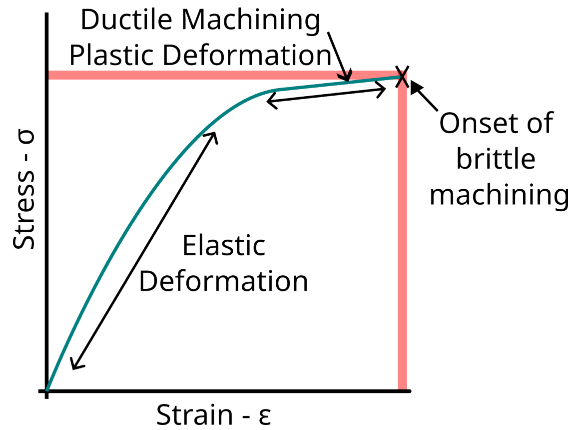

FIGURE 2.4: Chart displaying the ductile-brittle threshold on a representative stress-strain curve [12].

2.4 Ductile Machining

Ductile machining refers to the process where a brittle material is machined in such a way that brittle fractures are avoided, and instead, plastic deformation occurs up to the material's yield point. This results in a smooth finish with minimal cracks and chipping, which is crucial for improving optical performance. This process is especially important for brittle optical materials such as lithium niobate, silicon, and silica, that tend to fracture when traditionally machined.

The key to ductile machining is maintaining steady conditions that consistently remove material in a ductile state, keeping the stress-strain forces below the ductile-brittle transition threshold. This enables consistent plastic deformation, as shown in Figure 2.4 [12, 20, 21]. Achieving ductile machining requires careful optimization of machine operating conditions, including feed rate, blade depth of cut, and spindle speed, as well as dicing blade parameters such as grit size, grit concentration, and cutting edge shape [20] in order to keep the chip size under the critical chip thickness h_{crit} proposed by Marshall et al ;

$$h_{crit} = 0.15 \frac{E}{H_k} \left(\frac{K_c}{H_k} \right)^2 \tag{2.1}$$

Where E is the Youngs' Modulus, K_c is the fracture toughness and H_k is the knoop hardness [21, 22]. 0.15 was determined by Bifano et al. [20] for brittle ceramics. For lithium niobate and silicon, these values are typically on the order of 0.1 to 0.3 µm. For ductile machining, the feed reed rate and blade rpm have to be set such that per revolution of the blade in the material, the blade travels forwards at most the critical chip thickness. Other parameters like blade binder strength, and grit size consistency also affect the process but are beyond the scope of this work.

2.5 Lithium Niobate Ridge Waveguide Fabrication

This section shall discuss the typical ridge waveguide fabrication steps, focusing on non-linear secondary harmonic generation processes in lithium niobate. Further details on the non-linear process will be discussed in Chapter 5. The ridge waveguides discussed in this work are generally fabricated in a similar manner, as illustrated in Figure 2.5.

Periodic poling is performed using a photolithgraphy process to deposit photoresist in the poling pattern for the specific wavelengths involved. Electrodes pass a high voltage electric field through the wafer, forming the required periodic poling for secondary harmonic generation. Typically for a wafer based ridge waveguide, both vertical and lateral confinement is required. A wafer of crystalline material is either indiffused with a metal - typically zinc or titanium for lithium niobate - to change the refractive index properties, or is treated as a bulk substrate and layers of other crystalline materials are deposited or bonded onto the surface. The Covesion ltd. approach uses a zinc indiffused layer as specified in [23]. Then lateral definition occurs by machining grooves into the wafer. This creates air-gaps where the refractive index is 1, confining the light to the narrow waveguide. End facets on waveguides are historically polished after the fabrication steps due to poor form or surface finish, however, it is possible to single step polish and machine the facets with a dicing saw, with surface roughnesses as low as 0.29 nm Sa [24]. This provides significant time and cost savings.

2.6 Diamond Micro-Machining of Optical Materials

This section reviews the literature on micro-machining of optical crystalline materials using a dicing saw. As lithium niobate is the most commonly studied material in the literature, likely due to difficulties of obtaining isotropic etching [25], etch rate considerations and charge build up. Firstly, this section introduce work done on this material before covering other optical materials. For the sake of conciseness and relevance, the review has been narrowed to literature that provides both the machining parameter and some form of quantified metrology, such as surface roughness or width variation, as well as optical metrics like transmission or coupling losses, in order to facilitate meaningful comparison, although, direct comparisons have proven very limited. The machining parameters are provided in Table 2.1.

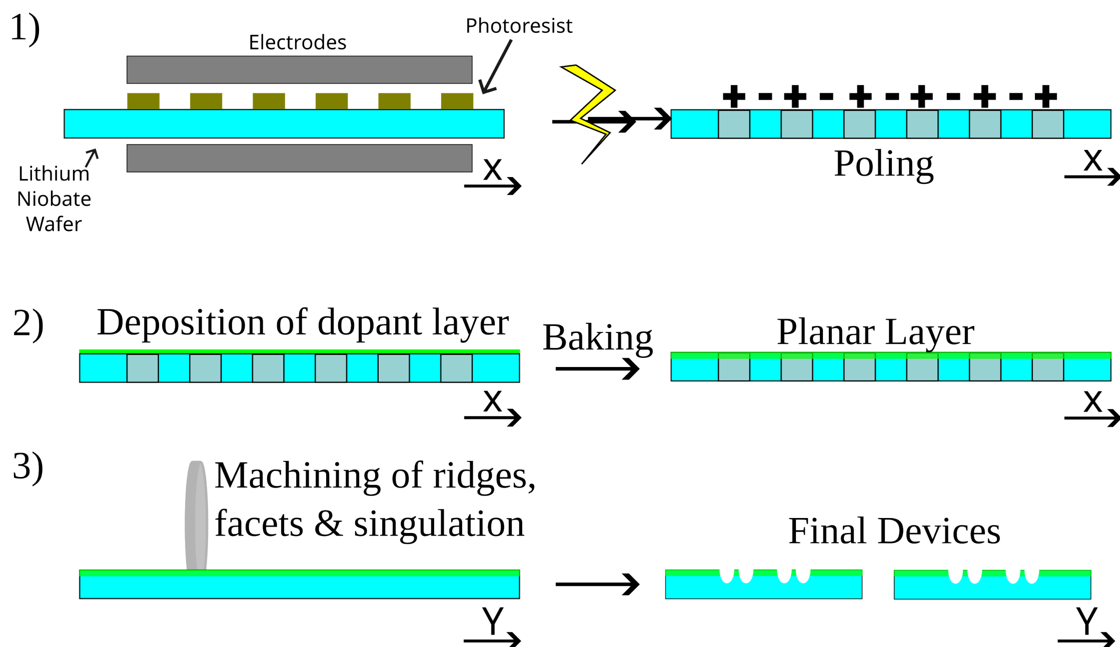

FIGURE 2.5: Schematic showing the process flow of ridge waveguide formation for the purpose of secondary harmonic generation; 1) Periodic poling is created in a lithium wafer 2) Formation of a planar guiding layer by indiffusion 3) Physical machining of ridges, facets and finally singulation into devices.

2.6.1 Lithium Niobate

Various ridge waveguides have been machined in doped lithium niobate using different parameters for various use cases. This section begins with the typical single-mode ridge waveguides, and then discusses more unconventional formats and results. In this review, indiffusion of dopants and ion exchange processes are assumed to not significantly impact the physical machining. However, to the Authors' knowledge, no studies have explicitly stated or investigated this.

Sun et al. in 2011 demonstrated green light generation using ridge waveguides fabricated by machining, reporting a facet roughness of 3.72 nm Ra and verticality of 3°, achieving an impressive optical conversion efficiency of 69.7% [16, 26]. However, there were no comments on the sidewall characteristics or fabrication parameters. In 2021, Suntsov et al. reported Watt-level 755 nm secondary-harmonic generation (SHG) in lithium niobate ridge wavguides, noting that the ridges exhibited a deviation of $\leq$ 0.1 µm in ridge width over 50 mm. [13, 14]. Suntsov et al. also reported that there was asymmetry in the ridge angles, with a difference of 4°. Despite this, the propagation losses were low, measured at 0.27 dB/cm at 1550 nm. Coupling efficiencies were also high, ranging from 83% to 94%, further underscoring the suitability of physical machining for fabricating ridge waveguides. Bruske et al. (from the same research group) fabricated ridge waveguides targeting 1085 nm, resulting in propagation losses of 1 dB/cm at 860 nm and 0.6 dB/cm at 1064 nm. While these values are impressively low, no additional details on the physical machining process were provided [27, 28].

Carpenter et al. in 2017 reported the best machined facet roughness to date, with a surface roughness of 0.29 nm Sa achieved in a single step [24], eliminating the need for expensive and time-consuming polishing. This impressively low roughness is directly comparable to results achieved through polishing, and although no optical testing was conducted on this specific waveguide, it demonstrates that physical machining can be used to finish waveguide surfaces without additional post-processing. The paper also emphasized the importance of blade selection; resin and nickel blades were compared under similar grit compositions and machining parameters, yet the resin blade produced nearly double the surface roughness, with 0.54 nm Sa.

Having discussed standard lithium niobate ridge waveguides, the review now turns to more unique formats and results to further demonstrate the capabilities of physical machining. In 2011, Courjal et al. fabricated high-aspect-ratio ridge waveguides, exploring a wide range of cut depths from 20 to 526 μm [18]. The sidewalls were impressively vertical at 88°, and the 526 μm-deep trenches proved to be the most efficient waveguides at 1550 nm, with ridge widths down to 6 μm, yielding a remarkably low propagation loss of 0.5 dB/cm for the TE mode. This showcases the versatility of ridge waveguide machining, which has also been applied in the fabrication of surface acoustic wave (SAW) devices [29–31].

Courjal et al. also compared the performance of round vs. square-shaped ridge trenches [19]. Despite both having the same width of 4.2 μm, the round ridges outperformed the square ridges, with reported propagation losses of 1.1 dB/cm and 2.5 dB/cm for the TE mode, respectively. The better performance of round ridges was theorized to result from improved mode propagation. They also confirmed that ridge waveguide losses increase as ridge width decreases, due to the smaller ridges being more sensitive to surface imperfections.

In 2015, Caspar et al. fabricated tapered ridge waveguides connected to standard waveguides and found that the taper reduced insertion losses by 3 dB. This method was successfully used to create electro-optical ridge waveguides for miniaturization purposes [32]. Achieving this required precise control of blade radius and cut length to minimize transmission losses to below 1 dB/cm, emphasizing the need for deterministic machining.

A study by Gerthoffer et al. investigated the effect of baking waveguides post-machining to further reduce propagation losses, reporting a significant improvement to 0.1 dB/cm [33], compared to the 0.5 dB/cm discussed in [18]. This improvement is attributed to high temperature annealing the crystal lattice damage caused by physical machining. The resulting propagation loss is the lowest this Author has seen in machined ridge waveguides and is comparable to that of standard proton-exchange fabricated waveguides. This highlights the importance of reducing subsurface damage caused by machining.

Another interesting format of lithium niobate involves thin films on a substrate, known as thin-film lithium niobate (TFLN), which enables more than 20x higher SHG conversion efficiencies compared to standard waveguides [34]. However, until recently, TFLN has been extremely challenging to machine physically due to delamination and chipping. These structures consist of a layer of lithium niobate only a few microns thick, deposited on an insulating or substrate layer (such as silicon) to provide the necessary refractive index contrast and/or structure, after which ridges are machined into the surface [35–39].

Due to the limited depth of the material, obtaining surface roughness data has been difficult. Only Chauvet et al. reported a sidewall roughness of 4-5 nm, along with propagation losses of 1.2 dB/cm for the TE mode [39]. Volk et al. reported similar propagation losses with ridge depths ranging from 1 to 20 μm [38]. They noted that deeper ridge waveguides exhibited form issues, tilting by up to 10°, while shallower ones tilted by $\leq 2°$, leading to complications in Fabry-Perot loss measurements and other applications.

Wei et al. estimated waveguide losses of approximately 1 dB/cm, which they found sufficient for their C-band wavelength multiplexing device, noting that a longer waveguide would further improve conversion efficiency, which is easily achievable [35]. Additionally, periodically poled lithium niobate on lithium tantalate was fabricated, targeting an 11 μm ridge width but achieving 12.6 μm. While no machining parameters were provided, the authors reported a frequency conversion efficiency from 1550 nm to 585 nm of 232.08%/W, the highest known to them.

Other use cases of physically machined lithium niobate include terahertz-wave resonators based on thin-film layers of silicon and lithium niobate [17], as well as tunable terahertz generation in bulk poled lithium niobate [15, 40]. These applications rely on machined gratings, though no specific machining parameters or optical performance data are provided. Nonetheless, they demonstrate the versatility of physical machining, despite its limitation of only fabricating straight-line features.

In 2022, Mwangi et al. fabricated an optical ridge waveguide-based polarization modulator with integrated electrodes, representing an impressive application of electro-optics. Despite insertion losses of 2.6 dB at 1550 nm, they reported high performance and noted that the energy consumption of physical machining is significantly lower than that of standard ion-slicing methods [41].

2.6.2 Other Optical Materials

This section will discuss the fabrication of ridge waveguides in other materials using the physical machining process, analysing the results, limitations, and potential directions for future work.

Ettabib et al. (2023) fabricated a ridge waveguide-enhanced Raman spectroscopy sensor using tantalum pentoxide [42], but reported a high insertion loss of 65%, indicating the need for further improvements in the physical machining of facets in non-standard crystalline materials. However, no specific machining parameters were provided. Similarly, Nd:YAG ridge waveguides have been successfully machined by Jia et al. [43], despite the material's extreme hardness. The cut depth was set to 9 µm, resulting in curved sidewalls due to aggressive wear. Nonetheless, the propagation loss was measured at 1.7 dB/cm, which is impressively low for such a difficult material. The authors also noted that further investigations into the waveguiding parameters are required.

Zinc selenide waveguides were fabricated by Cheng et al. [44], targeting a mid-infrared wavelength of 4000 nm. O^{5+} ion irradiation was used for depth confinement, followed by machining to create ridge waveguides. Despite high surface roughness values of 565 nm and 387 nm, the propagation losses were relatively acceptable at 1.3 dB/cm and 1.1 dB/cm, respectively. By introducing annealing treatments of unspecified temperature and duration, they significantly improved surface roughness to 4 nm and reported a corresponding reduction in propagation loss to 0.4 dB/cm indicating possible improvements with the physical machining process [44].

Cheng et al. later focused on machining ridge waveguides in lithium fluoride crystals, which offer an improved transmission band [44]. They reported pre-annealing propagation losses of 0.7 dB/cm and post-annealing losses of 0.2 dB/cm, although no surface roughness data were provided.

Terbium gallium garnet ridge waveguides, fabricated by You et al. [45], resulted in a propagation loss of 2.9 dB/cm at 633 nm, though no further details on the fabrication process were provided. Similarly, Er-doped germanate glass ridge waveguides, fabricated by Liu et al. [46], reported a propagation loss of 2.8 dB/cm. They also noted scattered light due to poor surface roughness, although no specific roughness metrics were given.

In 2023, Hasse et al. successfully machined ridge waveguides in praseodymium-doped lithium yttrium fluoride for the first time, achieving high lateral refractive index contrast. This innovation enabled high-performance ridge waveguides targeting 979 nm, with propagation losses as low as 0.4 dB/cm. However, they also reported losses of 2.5 dB/cm for visible light, indicating some sub-surface damage.

Potassium titanyl phosphate (KTP) ridge waveguides have also been successfully machined [47, 48]. Vernay et al. [48] achieved third-harmonic generation at 1594 nm with a conversion efficiency of 3.4%. They reported a surface roughness of 5 nm Ra and noted that only 40% of the ridge waveguides were suitable for further

characterization due to fabrication defects. No specific machining parameters were provided. Their closing remark emphasized that improving waveguide cross-section uniformity and decreasing propagation losses could potentially reach a theoretical maximum efficiency of 50%, highlighting a need for more indepth study of the physical machining parameters.

Kores et al. reported blue light (468 nm) generation in KTP with a conversion efficiency of 0.12% [47]. They found the fabrication challenging and observed poor propagation, with only 5-20% of the input light transmitted due to scattering. They attributed these issues to significant topside chipping and suggested that further optimization of the dicing process is necessary.

A notably unusual case was the micromachining of a flat optical fiber by Ambran [49], where a dicing saw was used to create two air trenches 204 μm apart in an air-fiber, resulting in a multi-mode interference device with high lateral index contrast. However, Ambran reported an excess loss of 1.89 dB, attributed to scattering and fabrication imperfections.

Another interesting scenario involved the fabrication of 90° mirrors in waveguides to create bends, as reported by Zha [50]. They achieved a surface roughness of 2.3 nm. Additionally, Fathy et al. [51] reported impressively vertical sidewalls (0.04°) for gas absorption spectroscopy using a silicon-on-insulator (SOI) platform, an improvement from the 2.8° roughness typically associated with etching processes.

2.6.3 Machining Parameters

The machining parameters found in the literature have been compiled in Table 2.1. It is clear that lithium niobate is the most popular material for physical machining, primarily for the fabrication of various optical waveguides in many formats such as ridge waveguides and thin film waveguides. and that DISCO DAD machines are almost universally used, making the research discussed in this thesis comparable, as the work in this chapter also utilizes a DAD machine. However, much of the published literature lacks enough detail for direct one-to-one comparison, largely due to variations in blades, machines, and fabrication processes and non-clarity across different publications. In some cases, only the machine model is reported.

From a parameter perspective, most dicing work uses similar settings regardless of the material: a 0.1 $mm\,s^{-1}$ feed rate, 20 krpm spindle speed, and a typical depth of cut of less than 40 μm. The highest feed rate observed in the literature is 1 $mm\,s^{-1}$ in ND:YAG, which is surprising given its hardness. However, this was achieved using an electroformed blade with a large grit size of #1000, which enabled the machining. The majority of studies employed resin blades with small grit sizes (#5000+), favoured for their self-dressing properties, however, can be limited in shape uniformity due to

higher wear rates. This has not been discussed in the literature, due to the limited fabrication distances used within literature.

It is noteworthy that there are no studies examining variations in feed rate or spindle speed on the resulting form, surface roughness and ultimately optical performance, particularly in lithium niobate, where there is significant commercial interest. This is critical, as feed rate is a primary limitation of physical machining.

2.7 Conclusion

This chapter has introduced microfabrication and physical machining within the context of photonic and optical device fabrication. A literature review has been performed. In conclusion, while physical machining has made significant progress over the past decade, particularly in the fabrication of ridge waveguides in lithium niobate, further optimisation is still required, especially for non-lithium niobate materials. Many works in the past few years have physically machined ridge waveguides in non-lithium niobate materials, however, significant imperfections have been found, especially in ridge uniformity and surface roughnesses.

There is a notable gap in detailed parameter studies across all crystalline materials of interest in optic and photonic fields, with a significant lack of comparable parameters relative to optical results, particularly in non-lithium niobate materials. There is yet to be a comprehensive study into the physical machining parameters (such as feed rate, spindle speed and depth of cut) and the resulting effects on the quality of the machined surfaces for any material of interest for the optics community. Addressing this gap is crucial for optimizing machining processes, understanding their impact on waveguide performance, and achieving deterministic machining, where the machining processes are controlled sufficiently that the reliability and performance of the end device is guaranteed without testing the machined features. In addition, issues related to surface roughness, uniformity, and material-specific physical machining parameters, particularly in harder crystalline materials, need to be identified and resolved.

References

1. Zhang Z, Yan J, and Kuriyagawa T. Manufacturing technologies toward extreme precision. International Journal of Extreme Manufacturing 2019; 1:022001
2. Taniguchi N. Current Status in, and Future Trends of, Ultraprecision Machining and Ultrafine Materials Processing. CIRP Annals. 1983 Jan 1; 32:573–82. DOI: 10.1016/S0007-8506(07)60185-1

3. Shore P and Morantz P. Ultra-precision: enabling our future. Philosophical Transactions of the Royal Society A: Mathematical, Physical and Engineering Sciences. 2012 Aug 28; 370. Publisher: Royal Society:3993–4014. DOI: 10.1098/rsta.2011.0638
4. Aurich J, Linke B, Hauschild M, Carrella M, and Kirsch B. Sustainability of abrasive processes. CIRP Annals 2013; 62:653–72
5. Schneider F, Das J, Kirsch B, Linke B, and Aurich JC. Sustainability in ultra precision and micro machining: A review. International Journal of Precision Engineering and Manufacturing-Green Technology 2019; 6:601–10
6. Levy JM, Ohadi MM, and Kyosung C. Energy analysis of cleanrooms in an academic research building. ASHRAE Transactions 2015; 121:71–84
7. Yang L. Prediction of steady-state wear coefficients in adhesive wear. Tribology Transactions 2004; 47:335–40
8. Lin JW and Cheng MH. Investigation of chipping and wear of silicon wafer dicing. Journal of Manufacturing Processes 2014; 16:373–8
9. Kawaguchi T, Mizuuchi K, Yamamoto K, Yoshino T, Imaeda M, and Fukuda T. Optical Waveguide SHG Devices Using $LiNbO_3$ Epitaxial Grown and Ultraprecision Machining Technique. The Review of Laser Engineering 2000; 28:600–3
10. Komanduri R. Cutting-tool Materials. *Encyclopedia of Materials: Science and Technology*. Ed. by Buschow KJ, Cahn RW, Flemings MC, Ilschner B, Kramer EJ, Mahajan S, and Veyssière P. Oxford: Elsevier, 2001 :1–13. DOI: https://doi.org/10.1016/B0-08-043152-6/00353-3
11. Brown H, Ballman AA, and Chin GY. Knoop microhardness measurements on lithium niobate and lithium tantalate. Journal of Materials Science 1975; 10:1157–60
12. Carpenter L. Precision dicing and micromilling of silica for photonics. PhD thesis. University of Southampton, 2013
13. Suntsov S, Rüter CE, and Kip D. Er:Ti:$LiNbO_3$ ridge waveguide optical amplifiers by optical grade dicing and three-side Er and Ti in-diffusion. Applied Physics B. 2017 Mar 29; 123:118. DOI: 10.1007/s00340-016-6635-1
14. Suntsov S, Rüter CE, Brüske D, and Kip D. Watt-level 775 nm SHG with 70% conversion efficiency and 97% pump depletion in annealed/reverse proton exchanged diced PPLN ridge waveguides. Optics Express. 2021 Apr 12; 29. Publisher: Optical Society of America:11386–93. DOI: 10.1364/OE.416723

15. Suizu K and Kawase K. Monochromatic-Tunable Terahertz-Wave Sources Based on Nonlinear Frequency Conversion Using Lithium Niobate Crystal. IEEE Journal of Selected Topics in Quantum Electronics. 2008 Mar; 14. Conference Name: IEEE Journal of Selected Topics in Quantum Electronics:295–306. DOI: 10.1109/JSTQE.2007.911306

16. Sun J, Gan Y, and Xu C. Efficient green-light generation by proton-exchanged periodically poled MgO:$LiNbO_3$ ridge waveguide. Optics Letters. 2011 Feb 15; 36. Publisher: Optical Society of America:549–51. DOI: 10.1364/OL.36.000549

17. Bassignot F, Haye G, Henrot F, Gauthier-Manuel L, Guichardaz B, Maillotte H, Ballandras S, Courjon E, and Lesage JM. New radio-frequency resonators based on periodically poled lithium niobate thin film and ridge structures. *2016 IEEE International Frequency Control Symposium (IFCS)*. 2016 IEEE International Frequency Control Symposium (IFCS). 2016 May :1–4. DOI: 10.1109/FCS.2016.7546793

18. Courjal N, Guichardaz B, Ulliac G, Rauch JY, Sadani B, Lu HH, and Bernal MP. High aspect ratio lithium niobate ridge waveguides fabricated by optical grade dicing. Journal of Physics D: Applied Physics 2011; 44:305101

19. Courjal N, Devaux F, Gerthoffer A, Guyot C, Henrot F, Ndao A, and Bernal MP. Low-loss $LiNbO_3$ tapered-ridge waveguides made by optical-grade dicing. Optics Express. 2015 Jun 1; 23. Publisher: Optical Society of America:13983–90. DOI: 10.1364/OE.23.013983

20. Bifano TG, Dow TA, and Scattergood RO. Ductile-Regime Grinding: A New Technology for Machining Brittle Materials. Journal of Engineering for Industry 1991 May; 113:184–9. DOI: 10.1115/1.2899676

21. Alao AR. Review of ductile machining and ductile-brittle transition characterization mechanisms in precision/ultraprecision turning, milling and grinding of brittle materials. Precision Engineering 2024; 88:279–99. DOI: https://doi.org/10.1016/j.precisioneng.2024.02.012

22. Marshall DB, Lawn BR, and Cook RF. Microstructural effects on grinding of alumina and glass-ceramics. Journal of the American Ceramic Society 1987; 70:C–139

23. Smith P, Ming L, O'Connor M, and Gawith C. Zinc diffused lithium niobate waveguides for high conversion efficiency second harmonic generation. 2005 Jan

24. Carpenter L, Berry S, and Gawith C. Ductile dicing of $LiNbO_3$ ridge waveguide facets to achieve 0.29 nm surface roughness in single process step. Electronics Letters 2017; 53. eprint: https://onlinelibrary.wiley.com/doi/pdf/10.1049/el.2017.2863:1672–4. DOI: 10.1049/el.2017.2863

25. Shen B, Hu D, Dai C, Yu X, Tan X, Sun J, Jiang J, and Jiang A. Advanced Etching Techniques of $LiNbO_3$ Nanodevices. Nanomaterials 2023; 13:2789

26. Sun J and Xu C. 466 mW green light generation using annealed proton-exchanged periodically poled MgO:$LiNbO_3$ ridge waveguides. Optics Letters. 2012 Jun 1; 37. Publisher: Optical Society of America:2028–30. DOI: 10.1364/OL.37.002028

27. Brüske D, Suntsov S, Rüter CE, and Kip D. Efficient ridge waveguide amplifiers and lasers in Er-doped lithium niobate by optical grade dicing and three-side Er and Ti in-diffusion. Optics Express. 2017 Nov 13; 25. Publisher: Optica Publishing Group:29374–9. DOI: 10.1364/OE.25.029374

28. Brüske D, Suntsov S, Rüter CE, and Kip D. Efficient Nd:Ti:$LiNbO_3$ ridge waveguide lasers emitting around 1085 nm. Optics Express 2019; 27:8884–9

29. Henrot F, Bassignot F, Guichardaz B, Ulliac G, Courjon E, Rauch JY, Baron T, and Ballandras S. Acoustic resonator based on periodically poled lithium niobate ridge. IEEE Transactions on Ultrasonics, Ferroelectrics, and Frequency Control 2013 Aug; 60. Conference Name: IEEE Transactions on Ultrasonics, Ferroelectrics, and Frequency Control:1556–63. DOI: 10.1109/TUFFC.2013.2735

30. Henrot F, Bassignot F, Guyot C, Rauch JY, Guichardaz B, and Ballandras S. Highly coupled resonator based on ridge-shaped periodically poled materials for radio-Frequency applications. *2013 Joint European Frequency and Time Forum International Frequency Control Symposium (EFTF/IFC)*. 2013 Jul :933–6. DOI: 10.1109/EFTF-IFC.2013.6702136

31. Henrot F, Bassignot F, Rauch JY, Ulliac G, and Ballandras S. Ridge-shaped periodically poled transducer for wide band R-F filter. *2014 European Frequency and Time Forum (EFTF)*. 2014 Jun :290–3. DOI: 10.1109/EFTF.2014.7331489

32. Caspar A, UlUac G, Suarez M, Calero V, Bernal MP, Courjal N, Roussey M, Häyrinen M, Laukkanen J, Honkanen S, and Kuittinen M. High-aspect-ratio electro-optical ridge waveguide made by precise dicing and atomic layer deposition. *2017 Conference on Lasers and Electro-Optics Europe & European Quantum Electronics Conference (CLEO/Europe-EQEC)*. 2017 Conference on Lasers and Electro-Optics Europe & European Quantum Electronics Conference (CLEO/Europe-EQEC). 2017 Jun :1–1. DOI: 10.1109/CLEOE-EQEC.2017.8086602

33. Gerthoffer A, Guyot C, Qiu W, Ndao A, Bernal MP, and Courjal N. Strong reduction of propagation losses in LiNbO3 ridge waveguides. Optical Materials 2014; 38:37–41

34. Hu C, Pan A, Li T, Wang X, Liu Y, Tao S, Zeng C, and Xia J. High-efficient coupler for thin-film lithium niobate waveguide devices. Optics Express 2021 Feb; 29:5397–406. DOI: 10.1364/OE.416492

35. Wei J, Hu Z, Zhang M, Li P, Wu Y, Zeng C, Tang M, and Xia J. All-optical wavelength conversion of a 92-Gb/s 16-QAM signal within the C-band in a single thin-film PPLN waveguide. Optics Express. 2022 Aug 15; 30. Publisher: Optica Publishing Group:30564–73. DOI: 10.1364/OE.465382

36. Ding T, Tang Y, Li H, Liu S, Zhang J, Zheng Y, and Chen X. Noncritical birefringence phase-matched second harmonic generation in a lithium-niobate-on-insulator micro-waveguide for green light emission. Optics Letters. 2024 Mar 1; 49. Publisher: Optica Publishing Group:1121–4. DOI: 10.1364/OL.519484

37. Lu C, Zhang Y, Qiu J, Tang Y, Ding T, Liu S, Zheng Y, and Chen X. Highly tunable birefringent phase-matched second-harmonic generation in an angle-cut lithium niobate-on-insulator ridge waveguide. Optics Letters. 2022 Mar 1; 47:1081. DOI: 10.1364/OL.449634

38. Volk MF, Suntsov S, Rüter CE, and Kip D. Low loss ridge waveguides in lithium niobate thin films by optical grade diamond blade dicing. Optics Express. 2016 Jan 25; 24. Publisher: Optica Publishing Group:1386–91. DOI: 10.1364/OE.24.001386

39. Chauvet M, Henrot F, Bassignot F, Devaux F, Gauthier-Manuel L, Pêcheur V, Maillotte H, and Dahmani B. High efficiency frequency doubling in fully diced $LiNbO_3$ ridge waveguides on silicon. Journal of Optics. 2016 Jul; 18. Publisher: IOP Publishing:085503. DOI: 10.1088/2040-8978/18/8/085503

40. Suizu K, Suzuki Y, Sasaki Y, Ito H, and Avetisyan Y. Surface-emitted terahertz-wave generation by ridged periodically poled lithium niobate and enhancement by mixing of two terahertz waves. Optics Letters 2006; 31:957–9

41. Mwangi M, Behague F, Coste A, Safioui J, Suarez M, Byiringiro J, Lutz P, Clévy C, and Courjal N. In-situ phase control of a low-loss membrane-based lithium-niobate polarisation-state modulator. Optics Continuum. 2022 Dec 15; 1. Publisher: Optica Publishing Group:2513–20. DOI: 10.1364/OPTCON.471413

42. Ettabib MA, Bowden BM, Liu Z, Marti A, Churchill GM, Gates JC, Zervas MN, Bartlett PN, and Wilkinson JS. Grating-incoupled waveguide-enhanced Raman sensor. PLOS ONE. 2023 Aug 10; 18. Publisher: Public Library of Science:e0284058. DOI: 10.1371/journal.pone.0284058

43. Jia Y, Rüter CE, Akhmadaliev S, Zhou S, Chen F, and Kip D. Ridge waveguide lasers in Nd:YAG crystals produced by combining swift heavy ion irradiation and precise diamond blade dicing. Opt. Mater. Express 2013 Apr; 3:433–8. DOI: 10.1364/OME.3.000433

44. Cheng Y, Zhang X, and Song H. O5+-ion irradiated ridge waveguide operating at mid-infrared wavelength in ZnS crystal. Applied Physics B. 2022 Apr 24; 128:94. DOI: 10.1007/s00340-022-07817-8

45. You JL, Wang YS, Wang T, Fu LL, Yue QY, Wang XF, Zheng RL, and Liu CX. Optical properties of He+-implanted and diamond blade-diced terbium gallium garnet crystal planar and ridge waveguides. Chinese Physics B. 2022 Nov; 31. Publisher: Chinese Physical Society and IOP Publishing Ltd:114203. DOI: 10.1088/1674-1056/ac7c02

46. Liu CX, Lu Y, Ding WJ, You JL, Zhang LL, Fu LL, Yue QY, Lin SB, and Zhou YJ. One-dimensional and two-dimensional Er3+-doped germanate glass waveguides by combination of He+ ion implantation and precise diamond blade dicing. Vacuum. 2023 Mar 1; 209:111743. DOI: 10.1016/j.vacuum.2022.111743

47. Kores CC, Mutter P, Kianirad H, Canalias C, and Laurell F. Quasi-phase matched second harmonic generation in periodically poled Rb-doped $KTiOPO_4$ ridge waveguide. Optics Express. 2018 Dec 10; 26. Publisher: Optica Publishing Group:33142–7. DOI: 10.1364/OE.26.033142

48. Vernay A, Boutou V, Boutou V, Félix C, Jegouso D, Bassignot F, Chauvet M, Boulanger B, and Boulanger B. Birefringence phase-matched direct third-harmonic generation in a ridge optical waveguide based on a $KTiOPO_4$ single crystal. Optics Express. 2021 Jul 5; 29. Publisher: Optical Society of America:22266–74. DOI: 10.1364/OE.432636

49. Ambran S, Holmes C, Gates JC, Webb AS, Carpenter LG, Mahamd Adikan FR, Smith PGR, and Sahu JK. Fabrication of a Multimode Interference Device in a Low-Loss Flat-Fiber Platform Using Physical Micromachining Technique. Journal of Lightwave Technology. 2012 Sep; 30. Conference Name: Journal of Lightwave Technology:2870–5. DOI: 10.1109/JLT.2012.2199465

50. Zha H, Yao Y, Wang M, Chen N, Zhang L, Bai C, Liu T, Ren Y, and Jia Y. Bending 90° Waveguides in Nd:YAG Crystal Fabricated by a Combination of Femtosecond Laser Inscription and Precise Diamond Blade Dicing. Crystals. 2023 Jan 20; 13:188. DOI: 10.3390/cryst13020188

51. Fathy A, Magdy M, Sabry YM, Marty F, Gnambodoe-Capochichi M, Khalil D, and Bourouina T. Silicon Multipass Cells for Localized Multi-Parameter Gas Sensing by Absorption Spectroscopy. Journal of Lightwave Technology. 2024 Mar; 42. Conference Name: Journal of Lightwave Technology:1702–9. DOI: 10.1109/JLT.2023.3325265

52. Tadanaga O, Yanagawa T, Nishida Y, Magari K, Umeki T, Asobe M, and Suzuki H. Widely tunable 2.3 µm-band difference frequency generation in quasiphase-matched LiNbO3 ridge waveguide using index dispersion control. Journal of Applied Physics. 2007 Aug 1; 102. Publisher: American Institute of Physics:033102. DOI: 10.1063/1.2767214

53. Zinaoui A, Grosjean L, Khouri M, Coste A, Suarez MA, Queste S, Gauthier-Manuel L, Robert L, Chauvet M, and Courjal N. Broadband second harmonic generation by birefringent phase matching in an X-cut $LiNbO_3$ membrane. EPJ Web of Conferences. 2023; 287. Ed. by Kibler B, Millot G, and Segonds P:06008. DOI: 10.1051/epjconf/202328706008

54. Zamboni R, Gauthier-Manuel L, Zaltron A, Lucchetti L, Chauvet M, and Sada C. Opto-microfluidic coupling between optical waveguides and tilted microchannels in lithium niobate. Optics Express. 2023 Aug 14; 31. Publisher: Optica Publishing Group:28423–36. DOI: 10.1364/OE.495406

55. Ito H, Sasaki Y, Suzuki Y, and Yokoyama H. Surface-emitted continuous THz-wave generation from PPLN. *(CLEO). Conference on Lasers and Electro-Optics, 2005.* (CLEO). Conference on Lasers and Electro-Optics, 2005. Vol. 2. 2005 May :1118–1120 Vol. 2. DOI: 10.1109/CLEO.2005.202043

56. Cheng Y, Lv J, and Chen F. Mid-infrared ZnSe ridge waveguides fabricated by swift Kr8+ ion irradiation combined with precise diamond blade dicing. Opt. Mater. Express 2015 Oct; 5:2292–9. DOI: 10.1364/OME.5.002292

57. Liu X, Wang G, Liang Z, Yao T, Miao H, and Sun R. Low-cost and facile assembly strategy for fiber ribbons and integrated optical waveguides with MT-ferrule-compatible optical connector. *2022 23rd International Conference on Electronic Packaging Technology (ICEPT)*. 2022 23rd International Conference on Electronic Packaging Technology (ICEPT). 2022 Aug :1–5. DOI: 10.1109/ICEPT56209.2022.9872627

58. Shi S, Abbas Z, Zhao X, Liang J, and Wang D. Numerical Simulation and Optimization of Stable Coaxial Jet Formation and Direct-Write Printing Array Nanoarchitectonics. Journal of Electronic Materials. 2024 Jan 1; 53:265–79. DOI: 10.1007/s11664-023-10768-1

59. Chen H, Huang H, Cheng J, Zhang X, Feng X, Cheng X, Ma L, Gu K, Liang W, and Lin W. Broadband yellow-orange light generation based on a step-chirped PPMgLN ridge waveguide. Optics Express. 2022 Aug 29; 30. Publisher: Optica Publishing Group:32110–8. DOI: 10.1364/OE.468218

60. Cheng Y, Song H, and Li S. Infrared LiF ridge waveguide fabricated by carbon ion irradiation. Laser Physics. 2022 Oct; 32. Publisher: IOP Publishing:126201. DOI: 10.1088/1555-6611/ac967c

61. Hasse K, Suntsov S, Püschel S, Tanaka H, Kränkel C, Bányász I, and Kip D. Ion-Implanted Diced Ridge Waveguides in Pr:YLF. *2023 Conference on Lasers and Electro-Optics Europe & European Quantum Electronics Conference (CLEO/Europe-EQEC)*. 2023 Conference on Lasers and Electro-Optics Europe & European Quantum Electronics Conference (CLEO/Europe-EQEC). ISSN: 2833-1052. 2023 Jun :1–1. DOI: 10.1109/CLEO/Europe-EQEC57999.2023.10231430

Citation	Material	Kerf (μm)	Blade Dia (mm)	Blade Type	Blade Grit	Machine	RPM (krpm)	X Speed ($mm\,s^{-1}$)	DoC (μm)
[15]	LN					DAD 522			300
[52]	LN								20
[24]	LN			Resin	#6000	DAD 3430	20	0.1	60
[26]	LN			Nickel	#5000	DAD3430	20	0.1	60
[14]	LN	100		Resin	#6000	DAD322	20	0.1	25
[53]	LN					DAD3350			
[41]	LN					DAD3350	10	0.2	
[54]	LN	50 & 200		”Polishing”		DAD3350	10	0.2	100
[55]	LN								400
[40]	LN					DAD522			
[18]	LN	200	56			DAD321	10	0.2	20
		200	56			DAD321	10	0.2	35
		200	56			DAD321	10	0.2	526
[33]	Ti:LN	200	56			DAD 3350	10	0.2	30
[32]	Ti:LN								40
[16]	MgO:LN								30
[27]	Er:LN					DAD322			10/15
[28]	Nd:Ti:LN								16 & 19
[17]	Si/LN/Si	400	52			Disco			100-500
[38]	LN Films	100		Resin		DAD322	20	0.1	1 - 20
[43]	Nd:YAG	200	52	Resin	#5000	DAD?	20	0.1	4.5 -9
[50]	Nd:YAG		50	Electroformed	#1000		30	1	200
[44]	ZnSe			Resin	#6000		15	0.05	
[56]	ZnSe						10	0.02	
[37]	LNOI								9
[49]	Ge:Silica Flat Fibre	18		Nickel	#5000	MicroAce3			140
[48]	Si/Gold/KTP/Silica	400	56						
[47]	KTP			Resin	#6000	DFD640	30	0.25	30-40?
[57]	Er:Germanate Glass	200		Resin		DAD3350	20	0.1	
[58]	SiO_2	40							30
[59]	Mg:LN on LT								15
[60]	LiF						20	0.1	
[37]	LNOI								9
[45]	TGG	200		Resin			20	0.1	
[61]	Pr:YLF			Soft-Bond		DAD322			~15

TABLE 2.1: Table of physical machining parameters in optical materials

Chapter 3

Metrology

3.1 Introduction

One key aspect of general fabrication of optics and photonics is obtaining metrological data of the fabricated features for both verification and comparison of various dicing parameters in subsequent experiments. Metrology in this context can be divided into two practical areas resulting from fabrication and alignment issues:

- **Surface roughness:** Localised surface texture, which is a critical factor in transmission and coupling losses and should therefore be minimised whenever possible.
- **Form error:** Error in large scale surface features as compared to the idealised design. Analysis of form errors provide information on machine alignment, tool stability, sample warp, wear rates, and other factors.

Three types of metrology are of particular interest: dimensional, defect, and material. Dimensional metrology is closely related to form, focusing on measuring the sizes and dimensions of the fabricated features on the samples. Defect metrology involves the measurement of localized defects, such as surface chipping and surface roughness. Material metrology pertains to material characteristics such as hardness and elasticity, which is out of the scope of this work.

In this work, due to the fragility of the machined features, metrology methods are primarily limited to non-contact optical techniques, as the contact techniques such as stylus profilers commonly cause scratches and ridge breakages during measurements. This is especially important for surface roughness measurements of the ridge waveguides (as in Chapter 5) where surface damage would affect optical measurements, though it is also a concern for other aspects of the fabrication process.

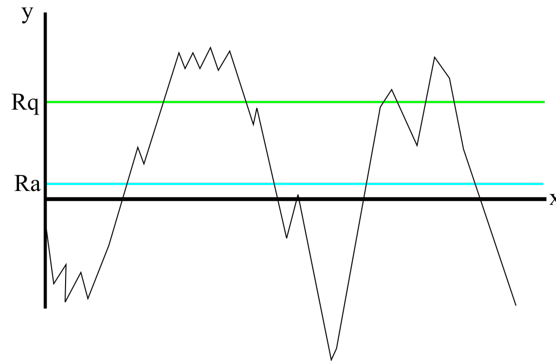

FIGURE 3.1: Diagram indicating the 2D surface roughness parameters, Ra and Rq on an example surface with form removed.

This chapter will discuss the relevant statistical definitions, provide an overview and limitations of the varied metrology equipment used, and describe the development of a bespoke metrology tool.

3.2 Definitions

There are numerous metrological statistical measurements detailed in the literature and defined by various standards agencies worldwide, e.g ISO 21920-2:2021 [1], ISO 16610-21:2011 [2], ASME B46.1-1995 [3], JIS B0601-1994 [4]. These measurements are commonly divided into 2D and 3D parameters, each suited for different tools and purposes. To obtain repeatable and accurate measurements, input data must be filtered and levelled to prevent data from being obscured by tilt or other large-scale deformations. This section shall discuss 2D, then 3D parameters, and then discuss the filtering recommendations.

3.2.1 2D Surface Parameters

The 2D parameters are obtained from a single line of n surface points, as indicated in Figure 3.1 [1–4].

Roughness Average (Ra) is defined as the average arithmetic perpendicular distance between the mean line and the values measured;

$$\mathrm{Ra} = \frac{1}{n} \int |y(x)|\, dx \tag{3.1}$$

And root mean square average (Rq - also known as the quadratic average, or RMS) is defined as;

$$\mathrm{Rq} = \sqrt{\frac{1}{n} \int y^2(x)\, dx} \tag{3.2}$$

The Rq allows for better indication of the average magnitude of the roughness compared to the Ra.

Peak to valley (PV) is defined as the distance between the maximum and minimum of the values;

$$\text{PV} = \max(y) - \min(y) \tag{3.3}$$

This is primarily used to obtain trench depths and feature heights. For this work, this is averaged out over multiple lines to minimise a single sample distorting the mean.

3.2.2 3D Surface Parameters

These are the 3D versions of the Ra and Rq parameters described above;

$$\text{Sa} = \frac{1}{n}\int\int Z(x,y)dxdy \tag{3.4}$$

$$\text{Sq} = \frac{1}{n}\sqrt{\int\int Z(x,y)^2 dxdy} \tag{3.5}$$

The 3D parameters provide a more complete representation of surface roughness due to being over a surface area, enabling a better comparison for optical surfaces. However, literature values often reference Ra for historical and equipment-related reasons. Ra and Rq can also be relevant when representing directional roughness or deviation over a larger scale, especially when using Rq to characterise form.

3.2.3 Filtering

To obtain accurate and repeatable roughness values, any form variations or waviness must be addressed and removed. Waviness refers to medium to long-scale variation in the surface, while form represents the overall shape of the device or sample.

The form can generally be removed by performing a large scale feature fit of either the nominal size and shape or a generic polynomial fit for removing curvature, then removing the fit from the data points as displayed in Figure 3.2. Alternatively it is possible to mask areas of curvature to remove unnecessary or distorted data. The first method does distort the resulting roughness, so masking is heavily preferred. When using a shape fitting, the results are no longer independently comparable, but can be comparable within the specific dataset. The specific shape filter will be specified when used, to allow for consideration.

To counteract waviness, the National Physical Laboratory (NPL) has produced a best practice guide for characterizing surfaces with roughness below 20 nm,

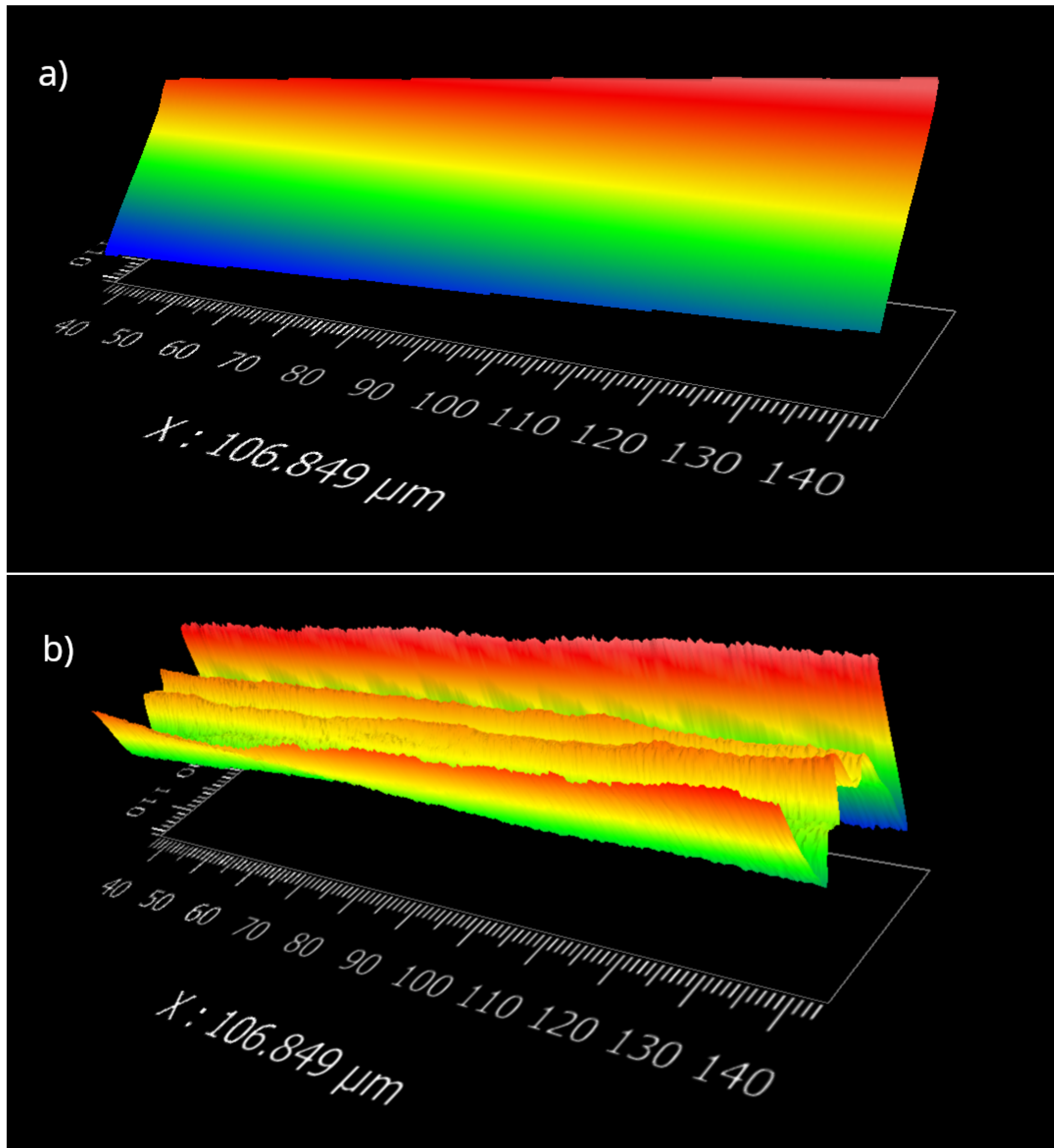

FIGURE 3.2: a) Raw sample surface data taken from a Zygo Zegage scan of a ridge waveguide sidewall b) Corrected of data removed by performing a plane fit removal, then a cylindrical fit removal

recommending the use of a low-pass filter with a set measurement length depending on the roughness magnitude for Ra and Rq measurements [5]. For surface roughnesses below 20 nm, the recommendation is to use a set measurement length of 80 µm, with a low pass filter of 17 µm. Although no guide has been produced for Sa and Sq nor for surface roughnesses greater than 20 nm, this work has based an approach on the recommendations of the Ra and Rq measurements. However, due to similar size and contamination issues, the measuring areas are limited. As mentioned with form, the parameters for the filters will be specified explicitly. Since the roughness values are used for internal comparisons, they remain valid as long as the filtering remains the same.

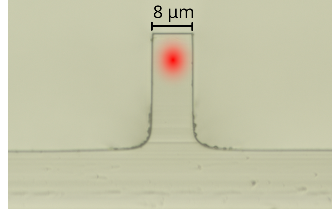

FIGURE 3.3: Microscope image of ridge waveguide facet with an optical mode drawn on as representation.

3.2.4 Top Side Chipping

Top side chipping is a well known defect from dicing, referring to small chips of material that break off from the top edge of the ridges during the wafer cutting process. This can be due to the blade entering the material with high force, causing material to chip away from the edges, or when the back side of the blade catches the edge of the cut. It is speculated that the latter is the primary cause of large amounts of top side chipping, especially when the chipping is asymmetrical.

Small amounts of top side chipping compared to other defects is not a critical concern for the optical performance. The power in the chipped regions is very small due to the location and shape of the optical mode within the ridge waveguide, as shown in Figure 3.3. However, it remains important to minimize this defect to achieve maximum conversion efficiency. If the chips penetrate too deeply into the optical mode, the conversion efficiency can be significantly impacted due to poor phase matching. This occurs because the effective refractive index within the waveguide changes, distorting the modal overlap.

Top side chipping is not numerically quantified by any standard, and various versions exist in literature [6–10], each with its own uses and definitions. Below are the most common conventions:

- **Chip size:** The lateral length of the chip along the cut edge. This measurement is useful for defect detection on the ridge waveguide
- **Maximum Chipping Depth:** The perpendicular distance that a chip penetrates into the material from the edge along the wafer surface. This measurement is useful for evaluating ridge waveguide defects.
- **Chipping Area:** The total projected area of the chipping missing from the edge surface, taking into account both the width and depth of the chips, as well as the number of chips.
- **Chipping Density:** The number of chips per unit length of the cut, often represented as chips per millimeter.

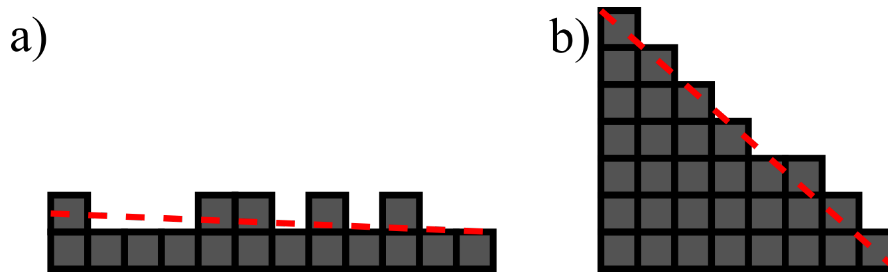

FIGURE 3.4: Diagram illustrating the advantage of a 45° scan over a pixelized horizontal cut scan. The red dashed lines represent the line of best fit for the data. a) Horizontal Edge Scan: In this case, the physical edge falls between pixels, resulting in a poor line of best fit. b) Rotated Edge Scan: Here, the pixels align more accurately with the edge, providing a better line of best fit and a more precise estimate of the chipping area.

Of all the measures discussed here, the chipping area is the most useful for evaluating diamond sawing performance because it can be easily calculated and compared, while still being highly representative. In this work, the measurement of top-side chipping is expressed as the chipping area density, defined as the chipping area per unit length of the edge.

This measurement is obtained by performing a 3D coherent scanning interferometry (CSI - see subsection 3.3.2) scan of the ridge edge positioned 45° diagonally across the resulting image. Scanning at this angle reduces edge pixel noise when the sample edge is horizontal or vertical, causing issues when determining the edge location. By rotating the sample 45°, the edge pixels are more accurately represented within the dataset, as illustrated in Figure 3.4. The 3D scan enables edge detection by setting a Z-axis threshold to simply exclude irrelevant pixels.

This binary pixel map of the surface is then processed using an edge detection algorithm to identify the edge pixels. A best fit line is fitted to these edge pixels to obtain the gradient of the edge. Due to the small scan size (0.174 x 0.174 mm) relative to the ridge size and blade cutting edge length, the edges are assumed to be locally straight over the edge length within individual scan sites. To correct the line fitting after considering the gradient, the Y-intercept of the fitted edge line is varied within a range of -20 to 20 pixels to minimize the number of points below the line while retaining at least a third of the edge pixels beneath the line. This adjusted line is taken as the true edge of the scanned sample. The number of pixels between this line and the scanned edge is counted, converted to an area and then divided by the scanned edge length to compute a chipping area density. The procedure is displayed in Figure 3.5.

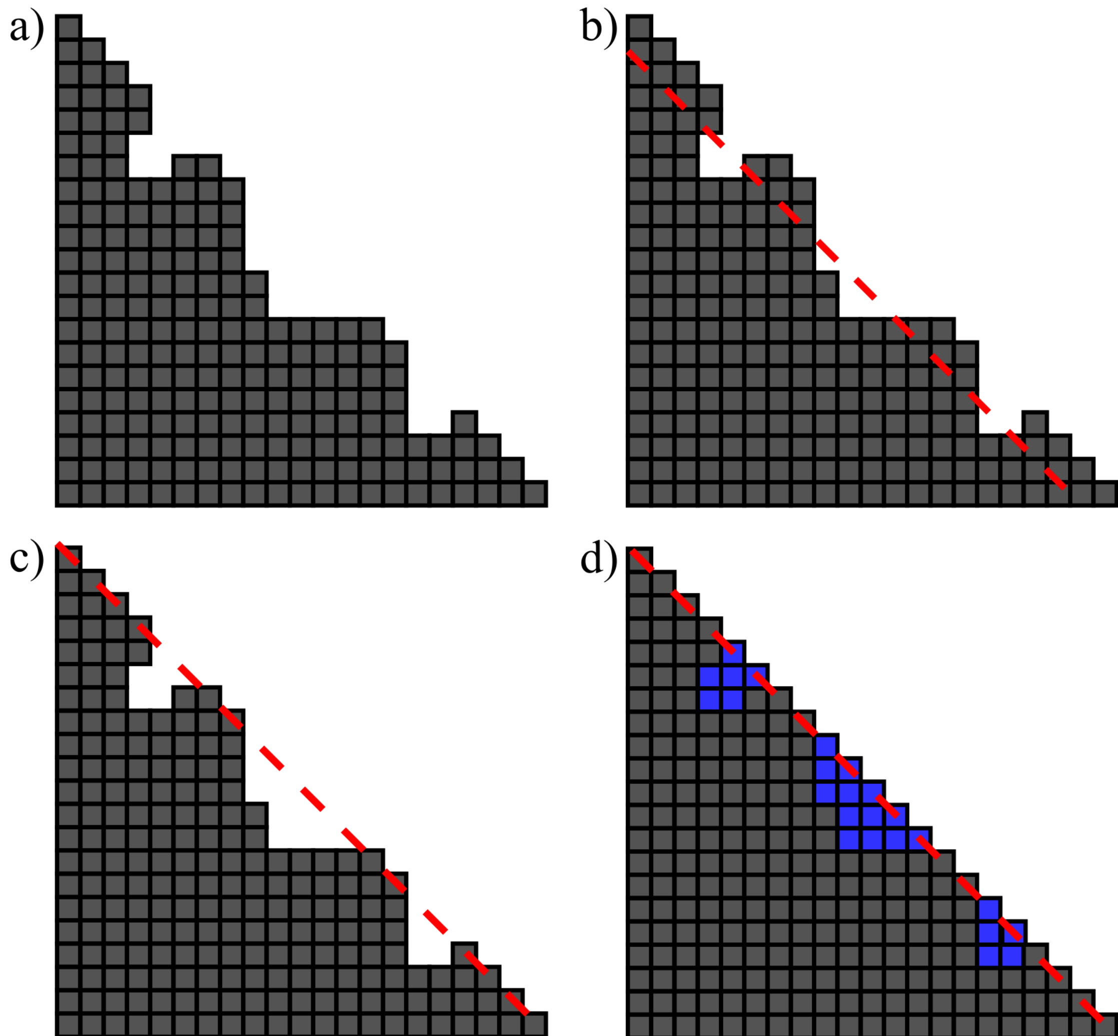

FIGURE 3.5: Diagram displaying the top side chipping processing method. a) A pixel bitmap of a chipped edge. b) A line is fitted to the average edge gradient of multiple scans. c) The edge line is fitted to the specific edge of the current scan. d) The number of missing pixels below the line and to the left of the edge are marked (blue) and counted. This is is then converted to an area missing per unit length statistic for the current scan.

3.3 Equipment

A range of equipment is available at the ORC for metrology, each with its own limitations and use cases. The equipment utilized in this work will be discussed in detail. Physical methods for metrology have seen minimal use due to the fragility of the samples, particularly narrow ridge widths that are prone to breaking when stylus tips are dragged over the edge. Additionally, tool head convolution can complicate post-processing, especially when profiling edges in depth. Therefore, only optical-based metrology tools have been employed, despite their own limitations with edges and narrow ridges [5, 11].

3.3.1 Scanning Electron Microscopy

Scanning Electron Microscopy (SEM) is commonly used to image samples across a range of resolutions, from millimeters to nanometers. The extreme resolution of SEM is achieved using an electron beam and various detectors that capture X-rays and scattered electrons, which can be triangulated to determine their source location. Our SEM tool also has limited material characterization capabilities through energy-dispersive X-ray spectroscopy (EDX/EDS). For more detail, the reader is referred to [12–15].

SEM has been used for determining sample contamination and for imaging blade sidewalls and facets due to its excellent depth of field. However, it does not provide true depth data and is therefore limited to 2D lateral dimensional measurements, albeit distorted to the depth of field.

3.3.2 Coherent Scanning Interferometry

Coherent Scanning Interferometry (CSI), also known as White Light Interferometry (WLI) or Vertical Scanning Interferometry (VSI), is employed to measure surface topography and roughness of samples. The core principle of CSI involves creating an interference pattern between a reference mirror and the sample surface using a light source with a very short coherence length.

An Mirau (or Michelson) interferometer is used to split a light source into two paths; one reflects off a reference mirror and the other off the sample surface. Due to the short coherence length, the focal region is very narrow. When the surface is within this region, the two beams will interfere, producing a fringe pattern at that height. The interferometer is then translated vertically, and the resulting fringes are captured by a camera. Each pixel will record a vertical interference pattern recorded, which is fitted to determine the height of the surface for that pixel, building a 3D topographical map. There are a range of algorithms used for fringe processing, but phase convolution is used within this work. These steps are indicated in Figure 3.6. For more information on fringe processing see [5, 11].

Two CSI tools were used within this work; the Zemetrics ZeScope and the Zygo Zegage. Both tools were validated using known step heights for the z-axis, gratings for the lateral x and y directions, and surface roughness measurements on targets with specified roughness ratings.

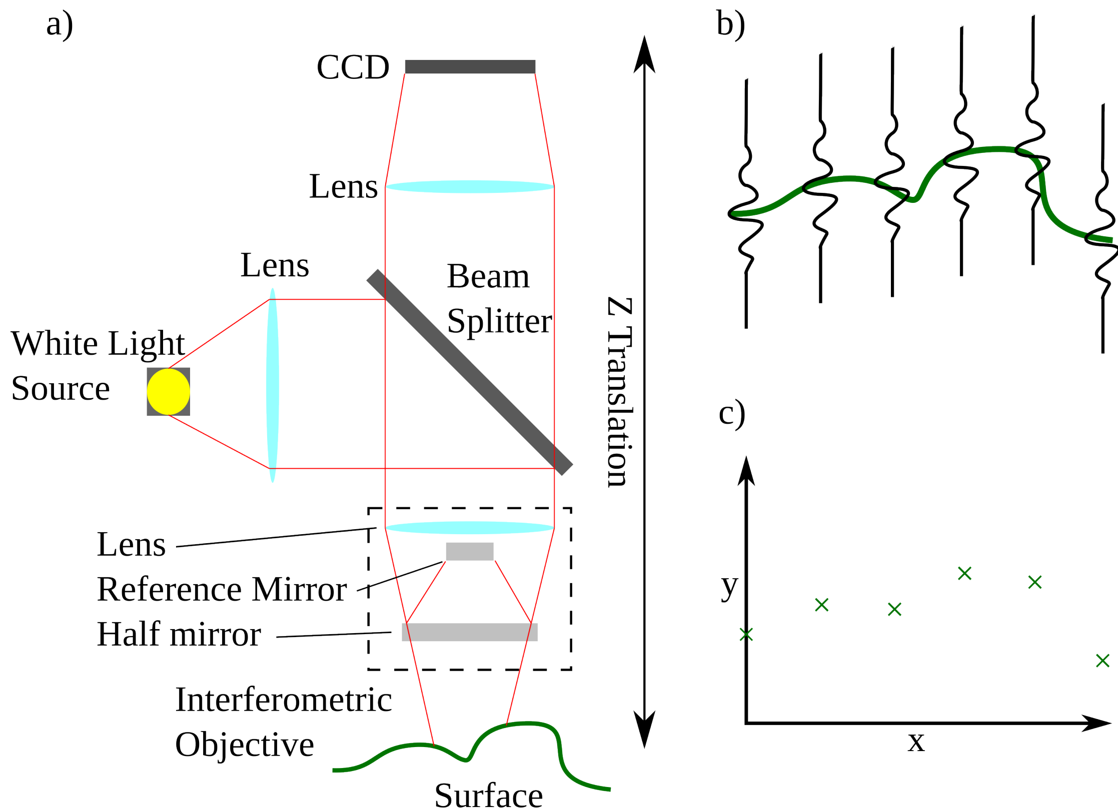

FIGURE 3.6: a) Labelled schematic of a Mirau interferometer based CSI tool. In Michelson based CSI, the reference mirror is positioned next to the beam splitter, rather than within the objective. b) An interferogram representation of a line through the surface. Various algorithms can be used to fit the interferogram; peak value, envelope convolution or phase convolution c) The obtained surface profile of the scan.

3.3.2.1 Limitations of CSI

Unfortunately, due to the optical nature of the method of measurement, there are a variety of possible artifacts. The artifacts encountered within the work and the resulting limitations will be discussed below.

Edge Diffraction Edge diffraction can occur at sharp edges such as ridge waveguides, leading to further interference with light from the true surface and causing distortion in the recorded fringes. This results in a slight ridge effect along the sharp edge, characterised by a jump upwards. This has to be taken into account when doing peak to valley measurements, however, it does not affect the lateral measurements. An example is displayed in Figure 3.7.

Batwing Artifacts Batwing artifacts are a wing-like distortion seen where there are two planar surfaces with a sudden height change between the two planes Figure 3.8. These are particularly known to happen when the Z height of the step between the two surfaces is smaller than the coherence length of the source light. These artifacts

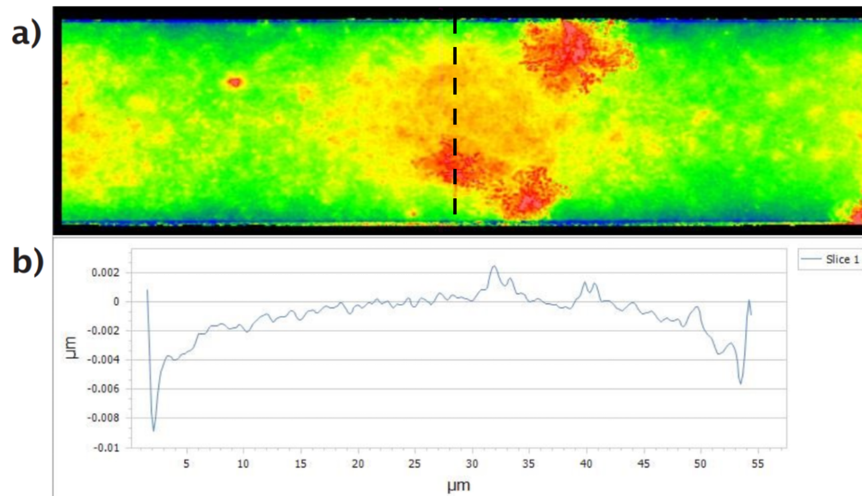

FIGURE 3.7: a) b) A height map of the diffraction artifact, characterised by the blue band along the edges c) A line trace of the diffraction artifact.

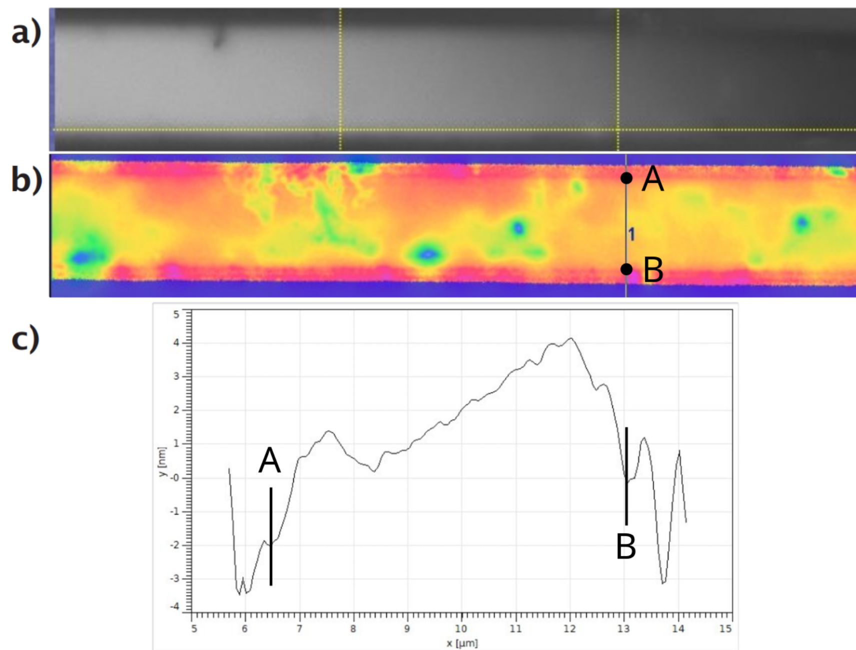

FIGURE 3.8: a) Grey scale image of the resulting batwing artifact bands. b) Heightmap of the batwing artifacts, the red bands indicating the batwing artifact location. c) A line trace of the batwing artifact, characterised by the sudden peak drops on either side (points A and B), indicating a phase-shift.

are caused by interference of light between the top and bottom surfaces, which causes a perceived phase distortion and causing the algorithm to see step heights that do not exist. Batwing artifacts only impact height measurements, and does not affect lateral measurements [5], i.e the perceived step is still in the same location as the physical surface. These can be minimised with algorithms or by adjusting the wavelengths used to scan the surface [16].

Multiple Reflections/Ghosting Multiple reflections are especially significant for thin layers of transparent materials, (such as ridge waveguides) where multiple reflections can occur due to the presence of multiple interfaces. If these interfaces are close together, as when measuring the sidewall roughness of a ridge waveguide, the reflections can interfere with each other. This causes severe distortion of the fringes, causing a failure to measure the profile of the sidewalls due to a bad fitting of the resulting interferogram.

3.4 Confocal Probe Scanner

This bespoke system was developed to provide large-scale topographical data, specifically aimed at profiling large scale form, such as straightness and width uniformity along the length of a ridge waveguide. It includes two key components; a confocal chromatic probe (CHRocodile 2HS unit) (imaged in Figure 3.9) with a measurement range of 1003 µm, a vertical resolution of 330 nm, and a lateral resolution of 3 µm, and a laser interferometrically referenced, aerostatic bearing and magnetically positioned translation stage - Aerotech ABL9000. The laser interferometer provides an accurate plane of reference, using a retro-reflector mirror system. An initial attempt used a blue laser, forming a confocal laser probe. This approach will be discussed first, including its limitations, followed by an explanation and validation of the confocal chromatic probe based scanner.

3.4.1 Laser Confocal Probe

The initial setup aimed to measure feature straightness using a blue laser point probe to profile wafer reflectivity as illustrated in Figure 3.10. While it provided a contrast map, it was limited to lateral positioning data on reflectivity changes and lacked height feedback. This absence of height feedback made it difficult to maintain a consistent focal height, affecting result reliability due to the spot-size varying over the scan. An optical microscope mounted on an Aerotech stage system served as a traveling microscope, relying on visual contrast between the trench and surface. Perfect perpendicular alignment was crucial to minimize lens distortion, but this was not always achievable, leading to inconsistent results.

Additionally, the response included convolution of the true surface with the probe head and unwanted back reflections. Despite efforts to mitigate these issues using absorbing beam blockers and pinholes of various sizes, these attempts were unsuccessful. Given these limitations and practicality issues, the decision was made to purchase a confocal chromatic probe from Precitec, which allows for accurate height profiling, resolving most of the issues discussed.

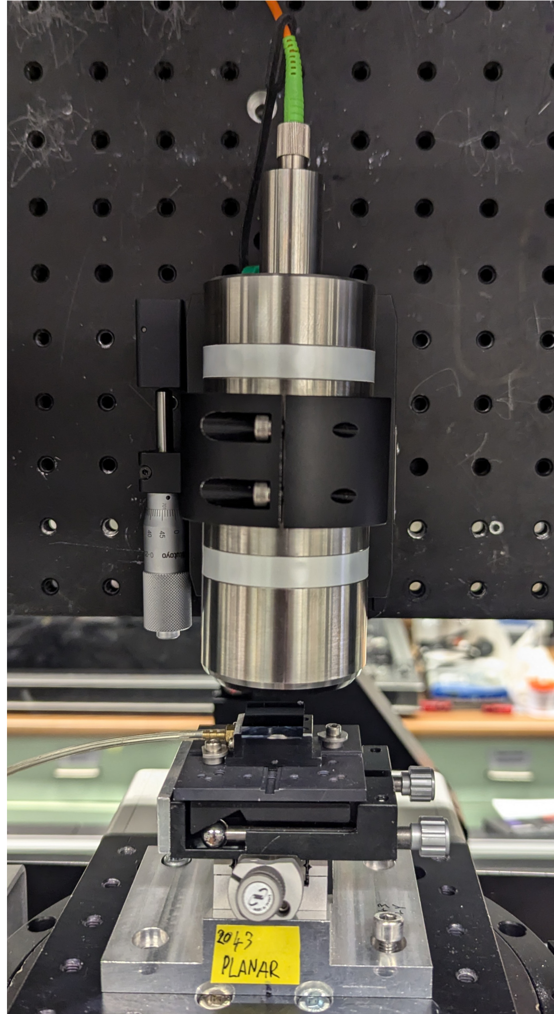

FIGURE 3.9: Photograph of the confocal scanner setup. The schematic is displayed in Figure 3.12

3.4.2 Principles of Confocal Chromatography

The confocal probe operates with chromatic dispersion of a polychromatic white light source. The white light, which has a low coherence length, is coupled into a fiber and directed to the probe head. There, a set of lenses disperses the light into a range of monochromatic focus points, as illustrated in Figure 3.11.

The reflected light from the sample is collected by the confocal probe and sent to a spectrometer, sometimes via a filtering pinhole. The spectrometer generate intensity over wavelength spectrum. A peak-finding algorithm identifies the central wavelengths of these peaks, which are then matched to distances from the probe using a calibrated look-up table. For transparent, layered surfaces with multiple parallel refractive index changes, each layer will produce a distinct peak, enabling accurate thickness measurements assuming that the peaks can be resolved from each other. These measurements correspond to optical path lengths and require corrections based

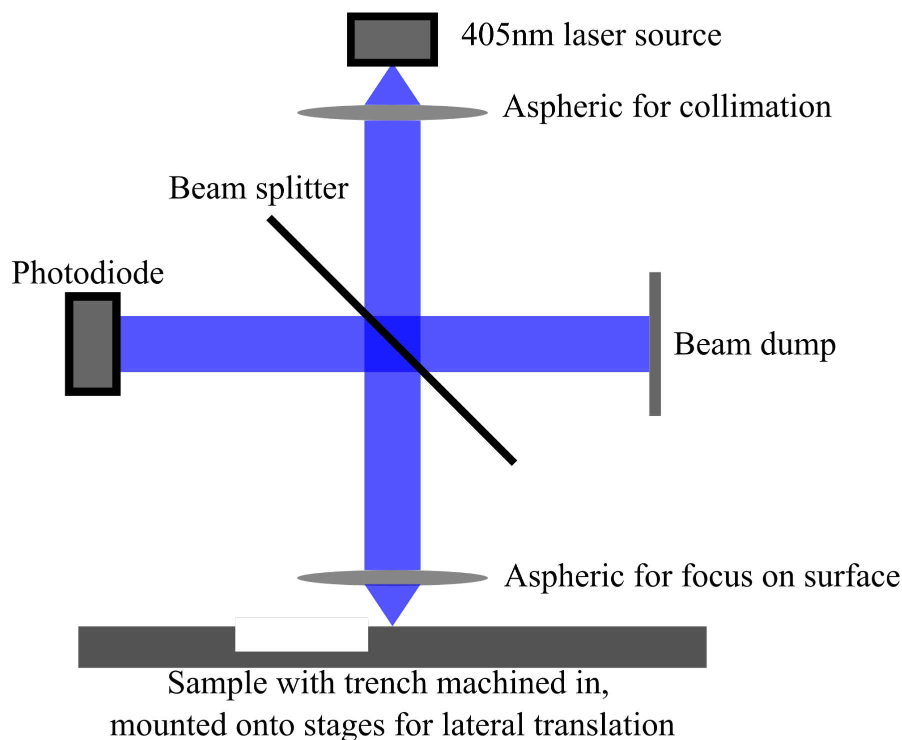

FIGURE 3.10: Labelled schematic displaying the laser point probe setup

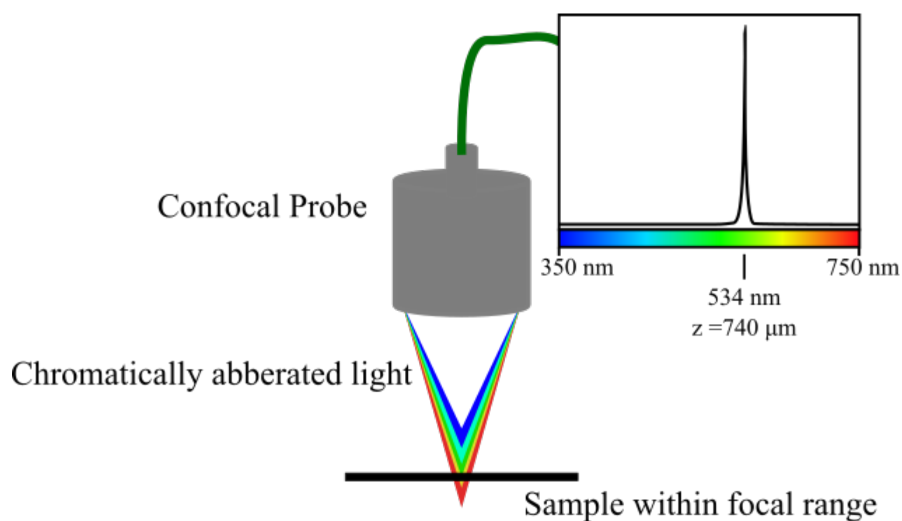

FIGURE 3.11: Labelled schematic displaying the principles of confocal chromatography

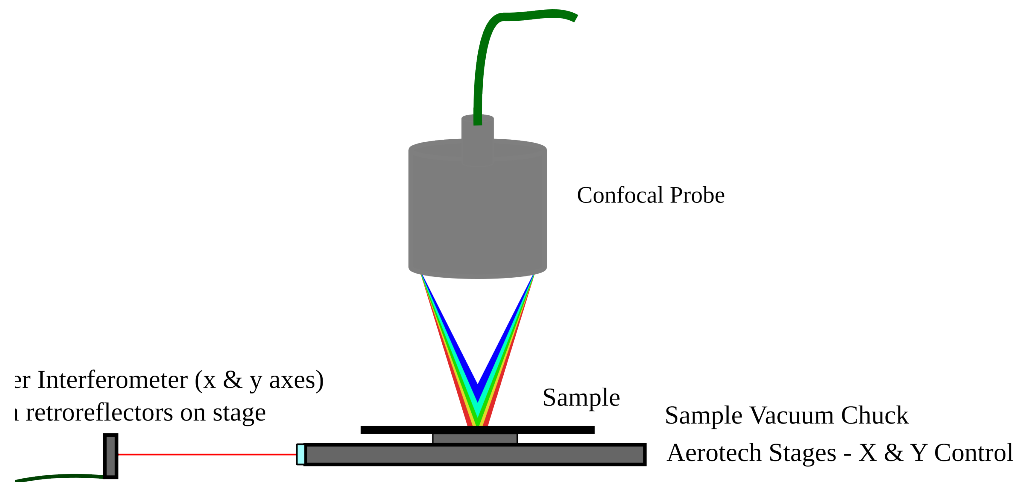

FIGURE 3.12: Schematic of the travelling confocal probe.

on refractive indices and Abbe numbers. Typically, a dedicated processor in the controller handles these corrections, allowing for high-speed, low-latency sampling, making it suitable for various tasks, including measuring fabricated devices. The setup of the equipment will be discussed next.

3.4.3 Confocal Scanner Development

The confocal scanner is a confocal probe travelling microscope utilising the Aerotech stages. The set up is shown in Figure 3.12. The Aerotech stages provide high lateral precision and thermal stability, being mounted onto a granite slab to minimise thermal expansion and ensuring rigidity. The stages operate on electromagnetically positioned air-bearing sliders, with glass encoders providing positioning feedback to the Aerotech controller with a resolution of 5 nm. However, due to issues with drift and technical constraints, the glass encoders are not employed for scanning positioning feedback. Instead a retro-reflecting laser interferometer encoder (Renishaw RLE20) is used, delivering a quadrature signal with a 9.88780 nm and 9.88779 nm distance resolution for the lateral X and Y axes respectively. The mirrors mounted on the stage are flat to $\lambda/20$. The quadrature output from the laser interferometer is connected to the confocal probe controller, which counts the number of quadrature signals detected, simplifying software development, as discussed next.

As part of this project, multiple pieces of software was developed for this system, including a standalone application that uses the Aerotech A3200 and CHRocodile software libraries. This application translates x and y distances, scan speed, serpentine step size, and confocal probe settings into the required g-code. The resulting data is shown in Figure 3.13, with the software logging the x and y start and end encoder counts and the averaged z values in CSV format for each sample.

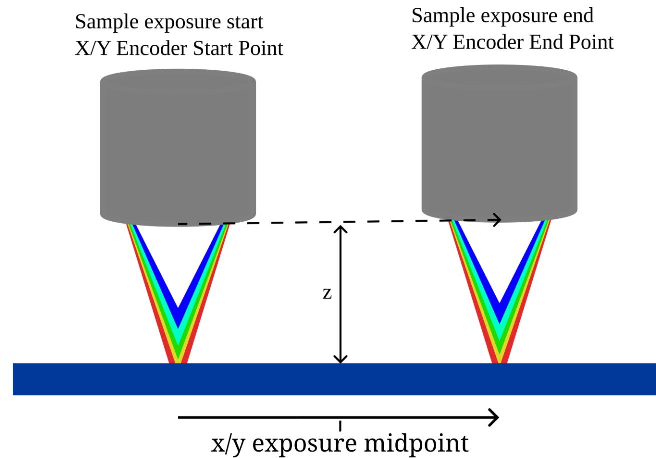

FIGURE 3.13: Diagram indicating the reported data of the confocal probe per exposure sample.

Processing is performed by a script that converts the data from a range of x, y, z points into a map of straight-line edges. For ridge scanning, the script assumes that the edges will be perpendicular to the scan direction, making edge pairing easier. It also assumes that the features are below the surface and that the top edge is large and flat, which facilitates straightforward linear levelling. Although these assumptions are not strictly necessary, they significantly simplify the processing.

The data is first loaded from the file, then split line by line. Due to the serpentine pattern used during the scanning, every intermediate line has no feature data and is removed. The sample exposure start and end positions for every sample (see Figure 3.13) are averaged to obtain the sample midpoint, and then multiplied by the interferometer sampling resolution to calculate the sample's lateral position. An example trace is shown in Figure 3.14, the tilt is highly exaggerated to illustrate the sample processing steps. The artifacts in the trace are optical effects and are discussed further in subsubsection 3.4.4.1.

Since these lines are not necessarily flat, the data for each line is binned by z, then levelled by subtracting the best fit line through the top bin. This is repeated twice to get accurate levelling as shown in Figure 3.14, which also establishes the surface reference point.

For edge detection, two parameters are defined, a threshold z value and a depth tolerance, with typical values of -0.5 µm and 10 µm respectively. The data is processed from left to right in a rolling pair of values. If the pair of values crosses the z threshold, and has a height change greater than the depth tolerance, the pair of points are marked as an Up or Down pair depending on the direction of travel (as in Figure 3.15). The Up and Down pairing allow for further edge pairing.

However, due to the confocal probe jitter, spectral shapes distortions and the low translation speed of the scans, each edge can have multiple Up and Down points. This

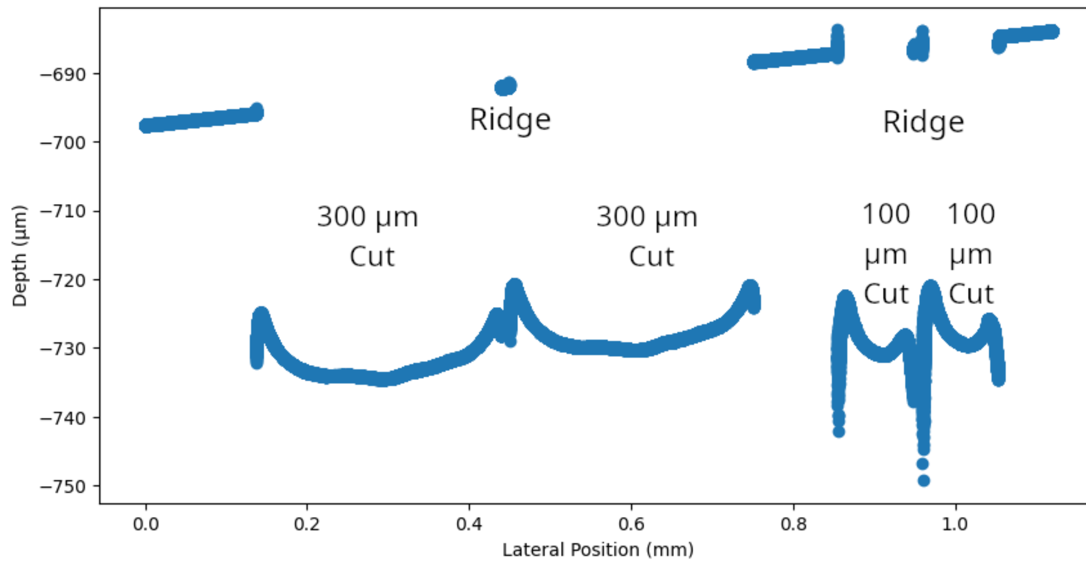

FIGURE 3.14: Example data from a confocal scan line across four cuts, two made with a 100 µm blade and two with a 300 µm blade, resulting in two waveguide ridges.

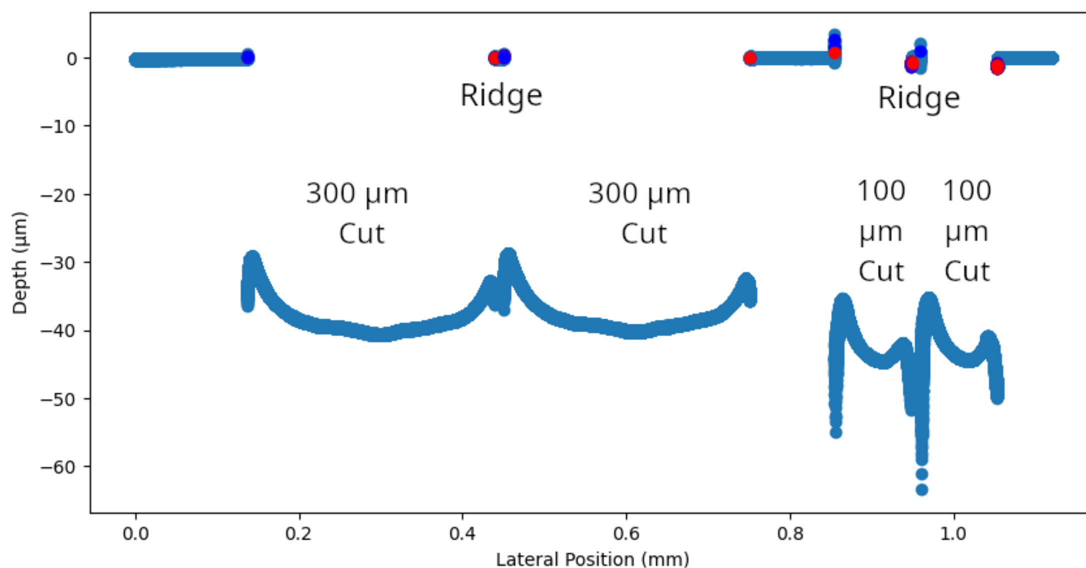

FIGURE 3.15: Confocal line trace with up (red) and down (blue) edge points marked. Each edges will have multiple up and down points.

"fuzziness" of the points is limited to where the confocal spot is, so averaging and calculating the standard error yields the location of the edge as seen by the confocal probe. Starting from the left, the first Down point (assuming the features are downwards) is selected. All Down points within 3 µm are gathered and averaged to determine the edge X and Y points. This process is repeated for the subsequent Up points, and then the Up and Down points are paired, resulting in multiple columns of points perpendicular to the feature lines. This is repeated along the length of the line for each row in the dataset, enabling the creation of a full topographical map of edges, as depicted in Figure 3.17.

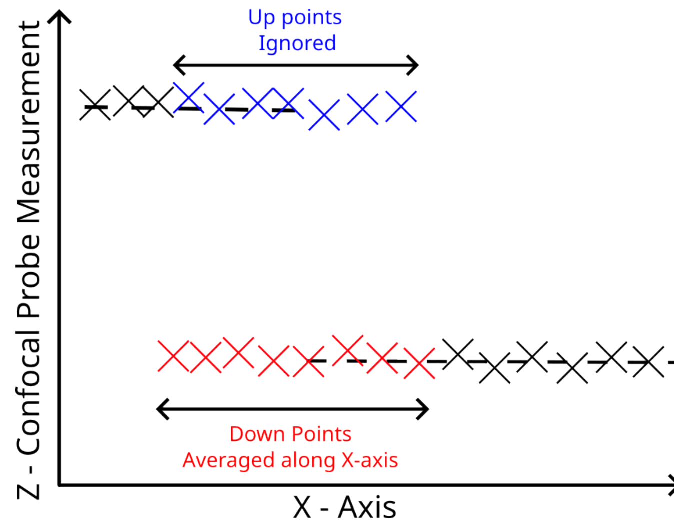

FIGURE 3.16: Diagram displaying how up and down points are processed for a typical step down edge. Starting from the left-most Down point, all of the Downs within a set distance are averaged over in both X and Y axes to get the a single edge location location with standard errors. This is repeated for the following Up points, allowing for pairing to be carried out.

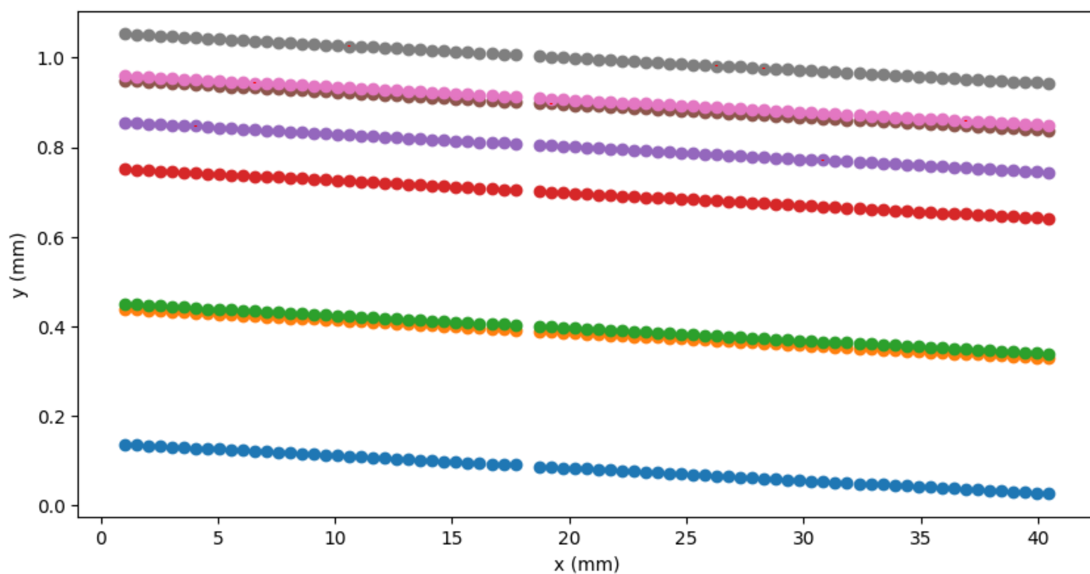

FIGURE 3.17: An example topographical map with data provided by the confocal probe. This consists of a line of edge points. The gap in the middle represents a section where the software could not match the column of points to a set of lines due to dirt on the sample, resulting in missing data.

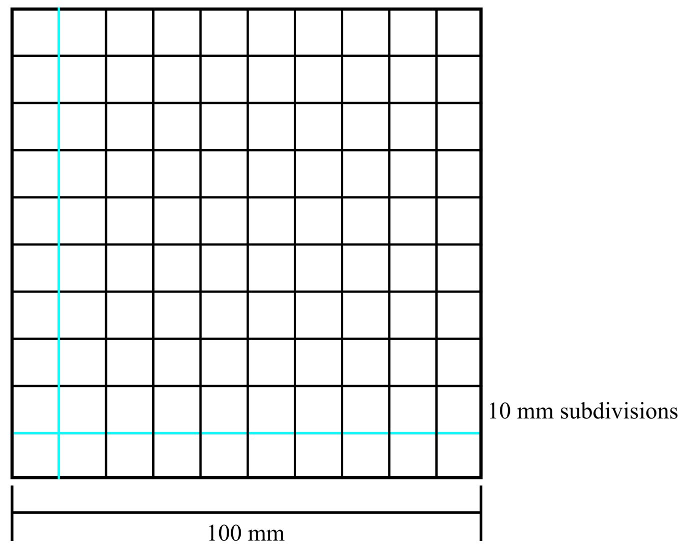

FIGURE 3.18: Figure displaying the precision graticule grid shape. The lines in blue were the profiled lines to obtain the stage squareness.

Since the primary use case of this is mapping ridges or machined features, a straight line can be fitted to each edge. This allows for the calculation of statistics such as period variation, straightness, and squareness.

3.4.4 Verification

To verify the confocal scanner's accuracy, a precision graticule was purchased from Precision Optics. This graticule is a thick glass slab with a grid of lines rated to be within 2 µm of straightness and with an angular tolerance of 5 arc-seconds, as displayed in Figure 3.18. The Z heights were verified against WLI scans of various steps. The stages have been previously verified to maintain 0.5 µm straightness over the full 300 mm length by Aerotech, and the interferometer encoder ignores any inaccuracy in the glass encoder.

The main verification step focuses on the squareness of the mirrors used for angular measurements. The graticule was scanned in an L pattern to determine the squareness error of the stages and mirrors. However, because the lines are vacuum-deposited chrome on glass with a height difference of only 40 nm, which is too small for the confocal probe to reliably resolve, the reflectivity of the chrome was used to locate the lines. The confocal probe's intensity threshold was set to ignore the peak from the glass, using only the brighter reflections from the chrome. This resulted in a series of short lines crossing the chrome lines, which were averaged to a midpoint with calculated standard errors. The scan results are displayed in Figure 3.19.

A linear regression performed on these two lines yields slopes of -55.991 ± 0.003 and 0.0187 ± 0.0009, indicating an angular error between the two mirrors of

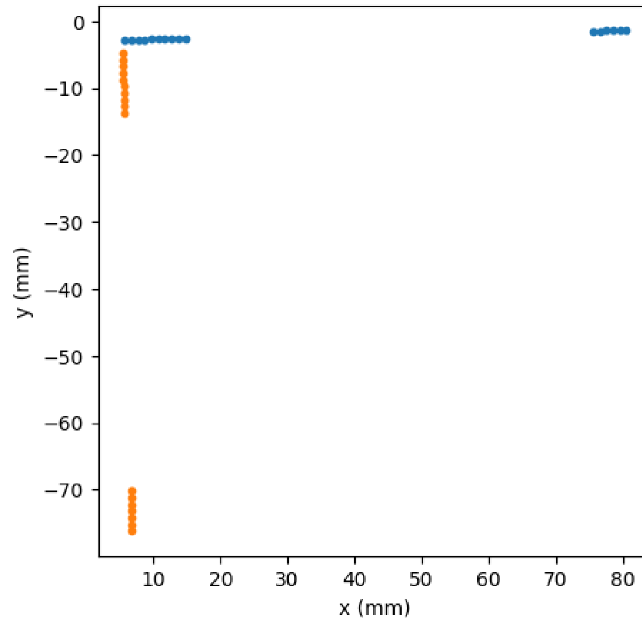

FIGURE 3.19: Charts displaying the scanned points of the graticule. Orange and blue represent the Y and X lines (relative to the stage axes) respectively, with each point consisting of multiple x and y edge positions.

$0.05046^\circ \pm 0.0014^\circ$, a highly precise measurement that is used for the correction of angular measurements.

3.4.4.1 Confocal probe artifacts

Similarly to the CSI, the optical-based measurement method used here also introduces artifacts around large vertical steps, as illustrated in Figure 3.20. These artifacts are primarily due to diffraction effects and the optical characteristics of the confocal probe.

Top Edge Diffraction At the top edge of a sharp step, diffraction causes a distortion in the spectral data. The diffraction tends to increase towards the blue end of the spectrum, making the top edge appear artificially higher. This effect occurs because shorter wavelengths (blue light) are more prone to diffraction, leading to an upward distortion in the measured height [17].

Bottom ”Drooping Artifact” The bottom edge of the feature exhibits a ”drooping” artifact. This is due to multiple reflections within the cut and the high numerical aperture (NA) of the lens, which skews the spectral data towards the red end of the spectrum. This effect causes the bottom edge to appear lower than its true position, creating a droop in the profile.

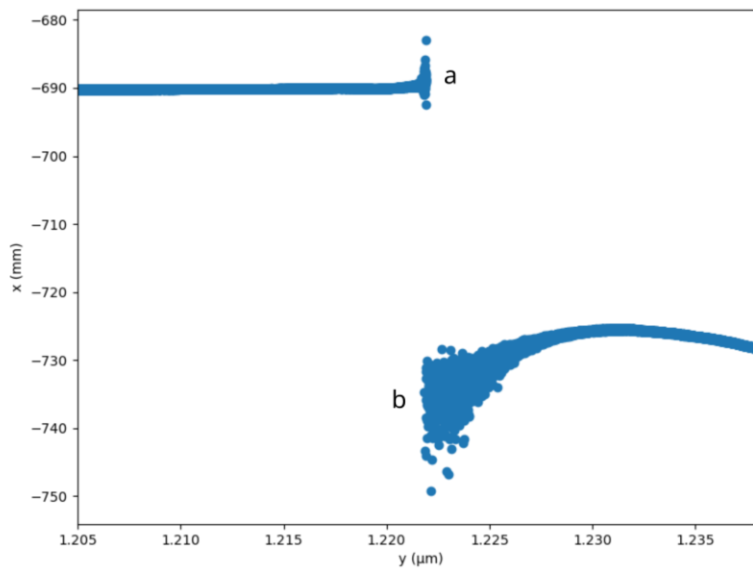

FIGURE 3.20: Line trace of a confocal probe step scan indicating the confocal artifacts resulting from optical effects. a) Diffraction over top edge with a preference for blue light. b) Scattering from bottom edge and sidewall with a red light preference

Neither of these artifacts will affect the lateral positioning of the result, only the vertical position is affected. Given the tool is primarily used for straightness measurements, this is not expected to cause any skew of results and no steps have been taken to correct for it.

Impact of Spot Size The confocal probe used has a spot size of approximately 3 µm, which is relatively large compared to the features being measured, although this is the smallest spot size on the market. This large spot size tends to overestimate the ridge location by approximately 1.5 µm. This overestimation occurs because the spectral data received from both the top and bottom of the feature is averaged, but the probe typically reports the top location until the peak from the bottom ridge becomes more pronounced. This behavior is inconsistent across scans due to slight variations in spot size with height and the reflectivity spectrum of the surface, which can affect the detection threshold.

Despite the relatively large spot size, the symmetry of the scanned features and the levelling steps implemented before scanning mitigate their impact. The overestimation primarily affects ridge width measurements, but it should not significantly influence the straightness values reported in this work.

3.5 Conclusion

This chapter has discussed the role of metrology in the verification and comparision of features in our work, primarily focusing on two areas, surface roughness and form errors, both of which are to be minimised for the functionality of our devices discussed in later chapters. This chapter has highlighted the requirement for non-contact based tooling, and have discussed a variety of artifacts that limit certain applications and use cases. A bespoke tool has been designed, developed and validated for the purpose of measuring straightness of machined features, a key parameter that has not been discussed in literature previously within the context of optics. Overall, the metrology techniques discussed here form the backbone of the experimental work, providing the necessary data to validate and optimize the fabrication processes explored in subsequent chapters.

References

1. ISO 201920-2:2021. Geometrical product specifications (GPS) — Surface texture: Profile. International Standard. Geneva, CH: International Organization for Standardization, 2021 Dec
2. ISO 16610-21:2011. Geometrical product specifications (GPS) — Filtration. International Standard. Geneva, CH: International Organization for Standardization, 2011 Jun
3. ASME B46.1-2019. Surface Texture (Surface Roughness, Waviness, and Lay). National Standard. Washington, DC: American National Standards Institute, 2019
4. JIS B0601-1994. Surface Roughness. National Standard. Tokyo, Japan: Japanese Industrial Standards Committee, 1994
5. Petzing J, Coupland J, and Leach RK. The measurement of rough surface topography using coherence scanning interferometry. Tech. rep. Teddington UK: National Physics Laboratory UK, 2010
6. Zhao H and Shi D. Process challenges in low-k wafer dicing. *IEEE/CPMT/SEMI 28th International Electronics Manufacturing Technology Symposium, 2003. IEMT 2003.* IEEE. 2003 :401–7
7. Su TJ, Chen YF, Cheng JC, and Chiu CL. Optimizing the dicing saw parameters of 60 µm wafer dicing street. Microsystem Technologies 2018; 24:3965–71
8. Shen J, Zhu X, Chen J, Tao P, and Wu X. Investigation on the edge chipping in ultrasonic assisted sawing of monocrystalline silicon. Micromachines 2019; 10:616

9. Hooper A, Ehorn J, Brand M, and Bassett C. Review of wafer dicing techniques for via-middle process 3DI/TSV ultrathin silicon device wafers. *2015 IEEE 65th Electronic Components and Technology Conference (ECTC)*. IEEE. 2015 :1436–46

10. Kumagai M, Uchiyama N, Ohmura E, Sugiura R, Atsumi K, and Fukumitsu K. Advanced Dicing Technology for Semiconductor Wafer—Stealth Dicing. IEEE Transactions on Semiconductor Manufacturing 2007; 20:259–65. DOI: 10.1109/TSM.2007.901849

11. Gianto G, Salzenstein F, and Montgomery P. Comparison of envelope detection techniques in coherence scanning interferometry. Applied Optics 2016 Aug; 55:6763–74. DOI: 10.1364/AO.55.006763

12. Yablon D and Libera M. Microscopy 101: Scanning Probes or Scanning Electrons: A Practical Guide to Select a Method for Nanoscale Characterization. Microscopy Today 2019; 27:32–8. DOI: 10.1017/S1551929519001044

13. Zhou W, Apkarian R, Wang ZL, and Joy D. Fundamentals of Scanning Electron Microscopy (SEM). *Scanning Microscopy for Nanotechnology: Techniques and Applications*. Ed. by Zhou W and Wang ZL. New York, NY: Springer New York, 2007 :1–40. DOI: 10.1007/978-0-387-39620-0_1

14. Shindo D and Oikawa T. Energy Dispersive X-ray Spectroscopy. *Analytical Electron Microscopy for Materials Science*. Tokyo: Springer Japan, 2002 :81–102. DOI: 10.1007/978-4-431-66988-3_4

15. Ngo PD. Energy Dispersive Spectroscopy. *Failure Analysis of Integrated Circuits: Tools and Techniques*. Ed. by Wagner LC. Boston, MA: Springer US, 1999 :205–15. DOI: 10.1007/978-1-4615-4919-2_12

16. Allendorf B, Käkel E, Ha UM, Hagemeier S, Hillmer H, and Lehmann P. Adaptive high-resolution Linnik interferometry for 3D measurement of microparticles. Opt. Lett. 2019 Jul; 44:3550–3. DOI: 10.1364/OL.44.003550

17. Niehues J and Lehmann P. Improvement of lateral resolution and reduction of batwings in vertical scanning white-light interferometry. Proceedings of SPIE - The International Society for Optical Engineering 2011 May; 8082. DOI: 10.1117/12.889180

Chapter 4

Machining Dynamics in Brittle Materials for Device Based Photonics

4.1 Introduction

As discussed in Chapter 2.6, there is a lack of detailed investigations into physical machining using a dicing saw configuration of a large variety of photonic/optical materials. Lithium niobate has seen the most investigations, primarily due to its incompatibility with conventional cleanroom processing and its commercial applications. Carpenter et al. compared both resin and nickel blades under similar grit compositions and machining parameters, yet the resin blade produced nearly double the surface roughness, with 0.54 nm Sa compared to 0.23 nm Sa for the nickel blade [1]. Another study by Courjal et al. compared two ridge shapes, both having the same width of 4.2 µm. The round ridges outperformed the square ridges, with reported propagation losses of 1.1 dB/cm and 2.5 dB/cm for the TE mode, respectively [2]. The superior performance of round ridges was theorised to result from improved mode propagation. However, apart from lithium niobate, other photonic materials are yet receive extended attention, with many materials only obtaining one or two proof of concept publications.

To summarise the literature review performed in Section 2.6, most research into physical machining within an optics context focuses on the applications or development of various tools and, as such, provides little statistical data or information on wear rates and form evolution of the machine tool or dicing blade. Additionally, there is limited information on the effects of machining parameters on brittle optical materials such as lithium niobate, silica, and silicon. These factors are crucial for achieving deterministic machining (defined as capabilities, which are

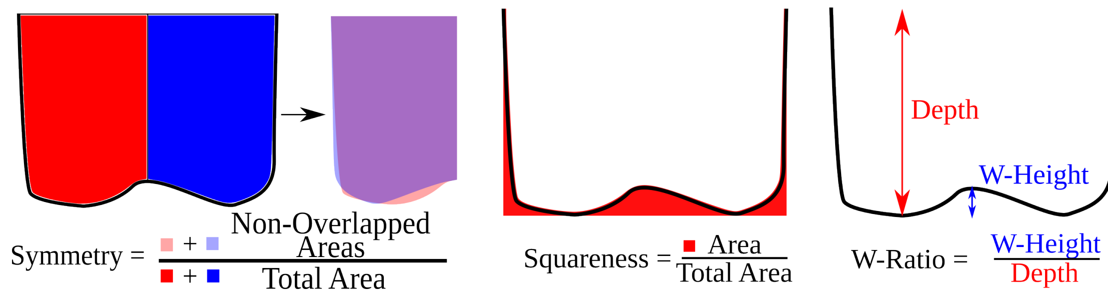

FIGURE 4.1: Illustration of the trench shape evolution quantification.

necessary for producing ultra-efficient photonic devices [1, 3–6]. The controllable parameters can be divided into two categories: process parameters (feed rate, spindle speed, and depth of cut etc.) and blade parameters (grit size, shape, diameter, blade composition, exposure, blade width, and shape etc.).

To further progress towards achieving deterministic machining of crystalline materials within the optical context, this chapter discusses two experiments. The first experiment investigates the machining dynamics of lithium niobate with the aim of improving ridge waveguide fabrication and advancing understanding of deterministic machining of ridge waveguides. The second experiment is a multi-material study where feed rates are varied as an attempt to link resulting surface roughness for different materials with feed rates, providing a test bed for determining optimal parameters for specific materials.

4.2 Parameter Definitions

This section will define the new parameters used to analyse physically machined trench shapes. These parameters are numerical measures that allow for a quantitative investigation into the evolution of the trench shape over multiple cuts. The measurements are obtained by performing a Coherence Scanning Interferometry (CSI) topographical scan of the trench ends, with samples held vertically using a 3D-printed mount. Post-processing is then conducted to extract shape information. The analysis begins by leveling the trench image through fitting the wafer surface, followed by applying a vertical cut-off to accurately locate the corners of the trenches, similar to work in Chapter 3. The following definitions are also illustrated in Figure 4.1.

Symmetry The symmetry ratio measures how symmetrical the machined trenches are. It is calculated by determining the midpoint between the two sidewalls and counting the number of non-symmetrical pixels on either side, up to the sidewalls.

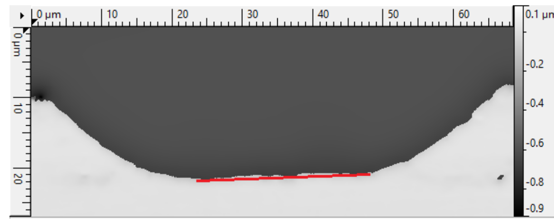

FIGURE 4.2: Grayscale image of a ”w” worn blade cut. The red line is drawn on to illustrate the ”w”.

This value is then expressed as a ratio by dividing it by the total number of pixels covering the trench.

Squareness The squareness is determined by fitting a bounding square to the trench, calculating the number of surface pixels inside the square, and then dividing this by the total number of pixels to obtain the squareness ratio.

W - Ratio An observed rise in the middle of physically machined trenches, as shown in Figure 4.2, has not been previously discussed in the literature, likely because most studies focus on wafer singulation rather than shallow trenches, as in this work. This phenomenon is likely due to uneven wear and blade loading, though the exact cause remains unclear. This will be referred to as the ”w” ratio, based on the trench shape. To quantify this numerically, the lowest point of the trench is taken as the depth value, and the highest point within the middle half of the trench is selected as the rise height. The ”w” ratio is then calculated by dividing the rise height by the depth value.

4.3 Evolution of Shape and Depth of Cut

This investigation examines the long-term evolution of trench shape and depth over a 10-meter cutting distance in lithium niobate, with the goal of achieving more deterministic fabrication of ridge waveguides.

4.3.1 Experimental Methodology

Two blade shapes and two depths of cut were targeted, selected for their simplicity. Two new resin dicing blades (RBT-6084 SD6000 N100 BR16) was dressed on two different dresser boards depending on the target shape. For a flat, rectangular dress, the dressing was performed on a PB08-F50 75 mm by 75 mm dressing board, using 2 lines at 5 $\mathrm{mm\,s^{-1}}$. For the round dressed blade, the dressing routine involved 10 lines

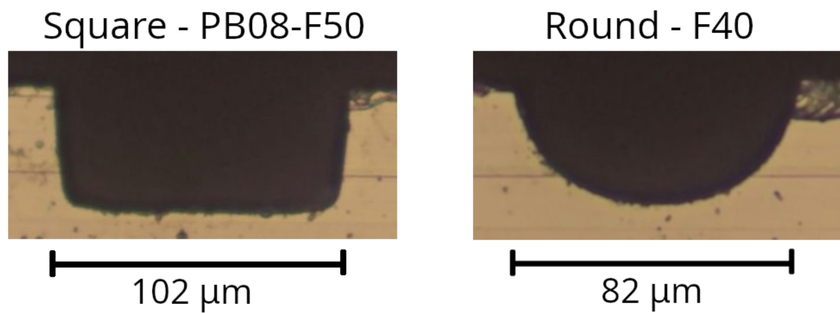

FIGURE 4.3: Microscope images of a square (left) and round (right) machined trenches

at 5 mm s^{-1} on a softer F40 25 mm by 25 mm dressing board. The resulting machined trenches for these blade shapes are shown in Figure 4.3.

The experiment begins by dicing out 4 25 mm by 50 mm rectangles of 5% MgO-doped lithium niobate (LN). Once the 52 mm diameter blade was suitably dressed, 400 trenches were machined into these rectangles at a feed rate of 2 mm s^{-1} and a spindle speed of 20,000 rpm, with either 50 or 100 µm depth of cut. This totalled 10 metres of cutting distance for each starting condition.

Top-down CSI measurements were carried out to assess the evolution of depth, width, and chipping. Then, CSI measurements of the trench ends (enabled by 3D-printed jigs) were performed to evaluate squareness, symmetry, and the w-ratio. Finally, the rectangle was singulated with a narrower blade (80 µm) along the middle of every 10th cut to enable CSI measurements of the sidewall surface roughness. The results are discussed in the next section.

4.3.2 Results & Discussion

Firstly, the results for the depth evolution are displayed in Figure 4.4. Surprisingly, both of the 100 µm deep starting conditions exhibited extreme wear in the first few cuts, indicating significant blade loading, followed by a prolonged period of stable wear. The initial blade geometry did not appear to have any major effect on this trend. All but one of the starting conditions tended towards the same final depth of cut of approximately 20 µm still sufficient for optical waveguide fabrication, provided the sidewalls remain sufficiently vertical, given that the optical mode diameter typically ranges from 7 µm to 11 µm. The exception is the 50 µm square starting condition, which showed a linear wear trend throughout. Although the cause of this behaviour remains unclear, the results suggest that blades tend toward a stable cutting depth where loading remains consistent. To minimise blade wear with this specific blade in lithium niobate, operated at a feed rate of 2 mm s^{-1} and a spindle speed of 20,000 rpm, a target cut depth of approximately 40 µm appears to offer an optimal balance between machining performance and blade longevity.

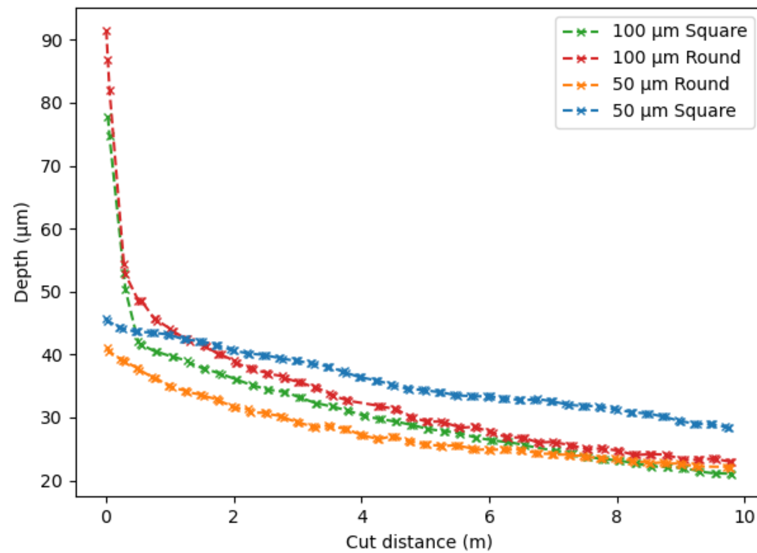

FIGURE 4.4: Chart displaying the evolution of cut depth over 10 m of machining distance for the initially 100 µm deep square and round, and the 50 µm deep square and round blades.

Most of the cut widths did not change notably over the cut distance, as displayed in Figure 4.5. The square starting conditions were the most stable, maintaining the same kerf width throughout the full duration, likely due to their vertical sidewalls experiencing no significant loading or wear. A handling error caused breakage in the 50 µm deep square starting condition, as seen by the sharp peak at the 9 m mark. The 100 µm deep round starting condition remained fairly stable, indicating that the sidewalls were vertical at the surface. Although the blade was slightly narrower than previous ones, the kerf remained within spec. The 50 µm deep round starting condition was the anomaly, showing errors in depth of cut and localized sample and/or bed curvature. This is confirmed by the curvature in Figure 4.5, where the width increases again, indicating that the wafer was bent. This again shows that round blades are more sensitive to issues with wafer curvature and depth of cut. For this reason, round blades should not be used for ridge waveguide formation, as ridge waveguides have poor optical tolerance for width variation [7–9].

Characterizing the squareness of the cuts proved challenging due to facet chipping and sample contamination, leaving several data gaps in Figure 4.6. Despite this, general trends can be observed; both square blades remained square throughout the cut, while the round blades gradually trended towards becoming square, likely due to increased tip loading, albeit very slowly. This further supports the idea that square blades are more shape-stable than round blades, increasing optical performance if used for physically machining ridge waveguides.

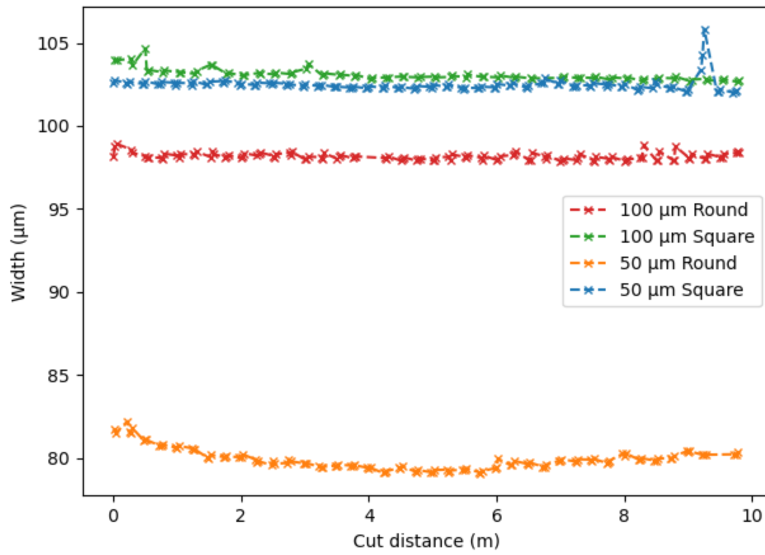

FIGURE 4.5: Chart displaying the evolution of cut width over 10 m of machining distance for the initially 100 µm deep square and round, and the 50 µm deep square and round blades.

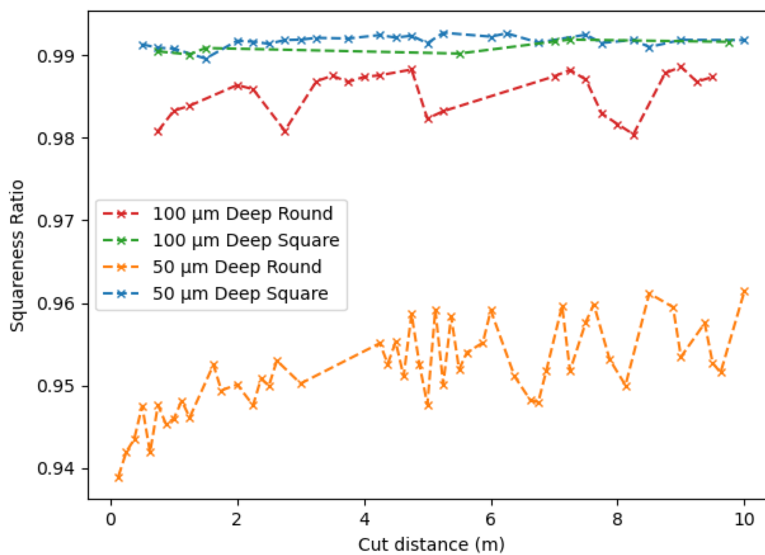

FIGURE 4.6: Chart displaying the evolution of squareness width over 10 m of machining distance for the initially 100 µm deep square and round, and the 50 µm deep square and round blades.

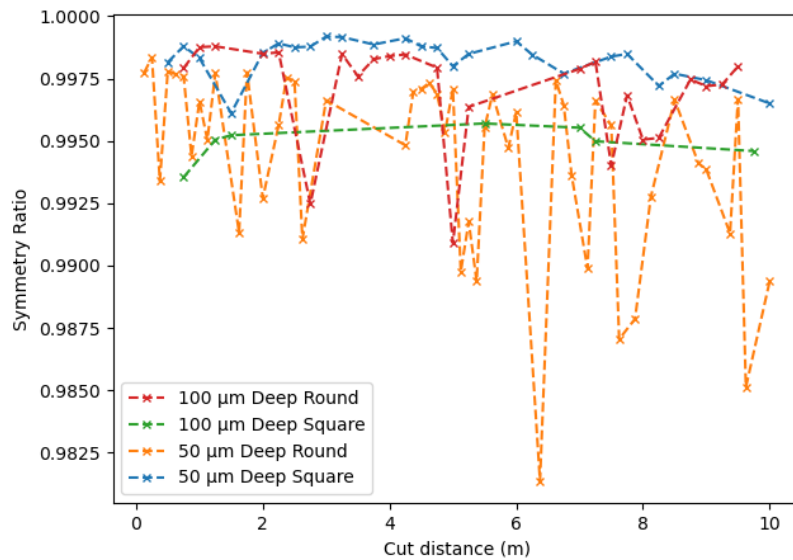

FIGURE 4.7: Chart displaying the evolution of cut symmetry over 10 m of machining distance for the initially 100 µm deep square and round, and the 50 µm deep square and round blades.

The symmetry of the cuts is displayed in Figure 4.7, shows minimal variation, however there is a slight decrease in symmetry for all of the blades. This implies that the blade loading is not even, likely due to an angle offset between the blade cutting axis and the machine feed axis. The round 50 µm deep blade remains the most unstable, with large swings in the symmetry, indicating uneven blade loading due to chip pockets filling up, causing poor debris clearance and blocking grits from cutting.

The W-Ratio is displayed in Figure 4.8, which indicates that the 100 µm and 50 µm deep square starting conditions avoided the W defect, while the 50 µm round deep blade worsened significantly. The W-ratio reached almost 10% of the cut depth, indicating that the blade has consistent uneven loading. This also explains the large asymmetry observed in Figure 4.8, as it is unlikely the trench was centered properly. This is unlikely to have any effect on the optical performance of ridge-waveguides, due to the physical distance from the sidewalls.

No significant trends were observed in the surface roughness and top-side chipping, so for the sake of conciseness, this data was formatted into Table 4.1 and Table 4.2, respectively. Surface roughness could not be measured for the 50 µm deep round starting condition due to contamination issues. The 100 µm deep square starting condition consistently showed the lowest surface roughness. Top-side chipping was heavily influenced by the initial blade condition, with the round starting condition performing 2-3 times worse than the square starting condition, and the 100 µm starting condition performing 8 times worse than the 50 µm starting condition, despite the overall trend toward the same shape. This highlights that the initial blade

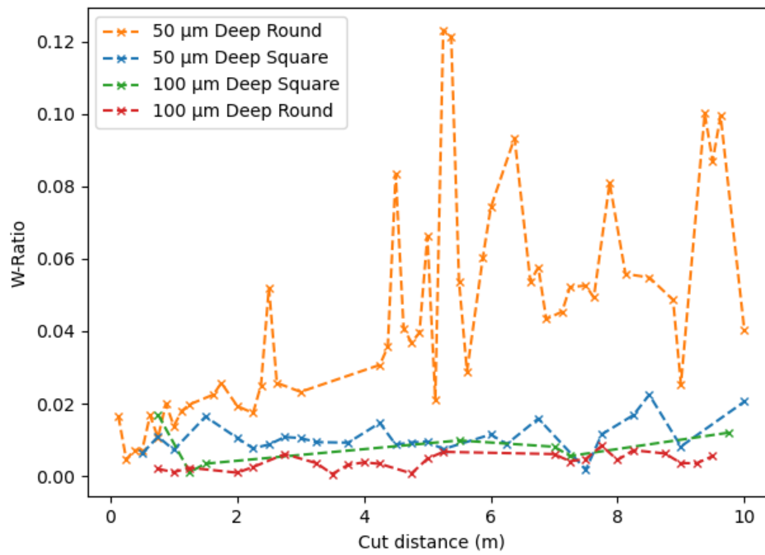

FIGURE 4.8: Chart displaying the evolution of cut "W-ratio" over 10 m of machining distance for the initially 100 µm deep square and round, and the 50 µm deep square and round blades.

	Vertical		Horizontal	
	Ra (nm)	Rq (nm)	Ra (nm)	Rq (nm)
100 µm Round mean	0.17	0.21	0.46	0.50
Std Err (n = 15)	0.016	0.018	0.067	0.085
100 µm Square mean	0.16	0.20	0.37	0.20
Std Err (n = 19)	0.003	0.005	0.051	0.004
50 µm Square Mean	0.41	0.54	1.49	1.74
Std Err (n = 15)	0.050	0.0058	0.414	0.537

TABLE 4.1: Table displaying the average surface roughness of initially both 100 µm and the 50 µm square machined trenches. See Figure 4.9 for measurement schematic.

	100 µm Round	100 µm Square	50 µm Round	50 µm Square
Mean chip # /mm	102.3	53.7	12.5	3.2
Stdev (n = 40)	55.0	38.2	15.3	4.0

TABLE 4.2: Table displaying the mean chip density for initially 100 µm and 50 µm round and square

conditions do have a long term effect on the physical machining, persisting despite the blades trending towards being identical.

All of the results highlight the significant impact of initial parameters on the extended dicing of lithium niobate, even as blade wear tends to guide the cut towards a relatively repeatable shape. This phenomenon is particularly pronounced in chipping

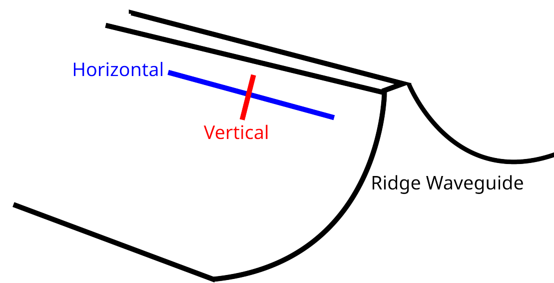

FIGURE 4.9: Schematic of vertical and horizontal Ra and Rq measured on a ridge waveguide.

but is also evident in surface roughness, blade wear rates, and the symmetry/W-Ratio. Properly configured initial parameters enable the achievement of a consistent form during cutting, albeit with some compromise in surface roughness. However, the roughness remains sufficiently low for ridge waveguide sidewalls and can be considered as largely ductile machining given the largely sub nm surface roughnesses. This is to be expected, given the blade distance per revolution is 0.24 µm compared to the critical chip size of 0.1 µm to 0.3 µm. These results have highlighted that square blades are notably more stable than round blades, exhibiting minimal form evolution and showing improved ridge waveguide uniformity. The 50 µm square blade, in particular, shows lower wear, though there is an indication of higher surface roughness as a trade-off. These findings suggest that further investigation into blade parameters is necessary, and further investigations into sample mounting, bed flatness, wafer warpage during machining is required to achieve truly deterministic results.

4.4 Blade Wear Rate as an Indicator of Ductile Physical Machining

This section proposes a link between material ductility and blade wear rate, along with a simple testing methodology to determine ductile machining parameters for different materials. This experiment proposes that increasing feed rates result in higher forces on the blade due to the increased material removal rate and blade pocket saturation [10, 11], leading to more rapid blade wear, therefore also proposing that minimum blade wear rate corresponds to the most ductile machining, and therefore results in the lowest surface roughness during machining.

4.4.1 Experimental Methodology

To test this theory across a range of brittle optical materials, lithium niobate, silicon, and silica were selected. A 25 mm by 50 mm rectangle of each material was singulated

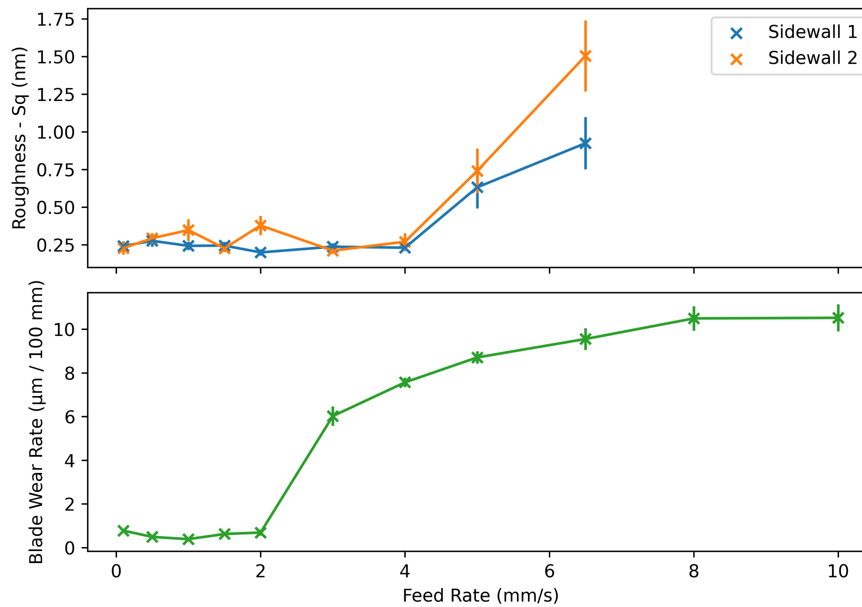

FIGURE 4.10: Chart displaying the roughness and blade wear rate for a range of machining feed rates for lithium niobate.

from a wafer. Groups of ten trenches were machined at each of the feed rates ranging from 0.1 mm s^{-1} to 10 mm s^{-1} in each material, with a spindle speed of 20,000 rpm and a 40 µm depth of cut using a fresh, undressed RBT-6084 SD6000 N100 BR16 blade. The depth of cut was specifically chosen based on the trends observed in Figure 4.4.

Top-down CSI scans were performed on every trench to measure wear rates as discussed in Chapter 3, and the samples were singulated down the middle of the 10th trench to measure surface roughness. The results and discussion follows.

4.4.2 Results & Discussion

Lithium niobate shows the most noticeable regime change, as indicated by Figure 4.10. There is a clear shift in regime at approximately 2 mm s^{-1} in both surface roughness and blade wear rate. At lower feed rates, the wear rates remain relatively constant, but beyond 2 mm s^{-1}, the blade wear increases. Interestingly, the change in surface roughness is delayed, only occurring after 4 mm s^{-1}. The exact reason for this discrepancy remains unclear, and the proposed correlation does not hold. This is theorised to be due to blade wear being consistent enough that despite the rate being higher, the exposed grit remains sufficiently dressed to machine smooth features.

Figure 4.10 displays a decrease in rate of wear rate increase with the feed rates. This is likely due to the initial high wear rate causing a significant reduction in the maximum depth of cut before the first measurement site. Additionally, the blade was found to leave a carbon residue on the sidewall, as confirmed by EDX analysis, revealing 13%

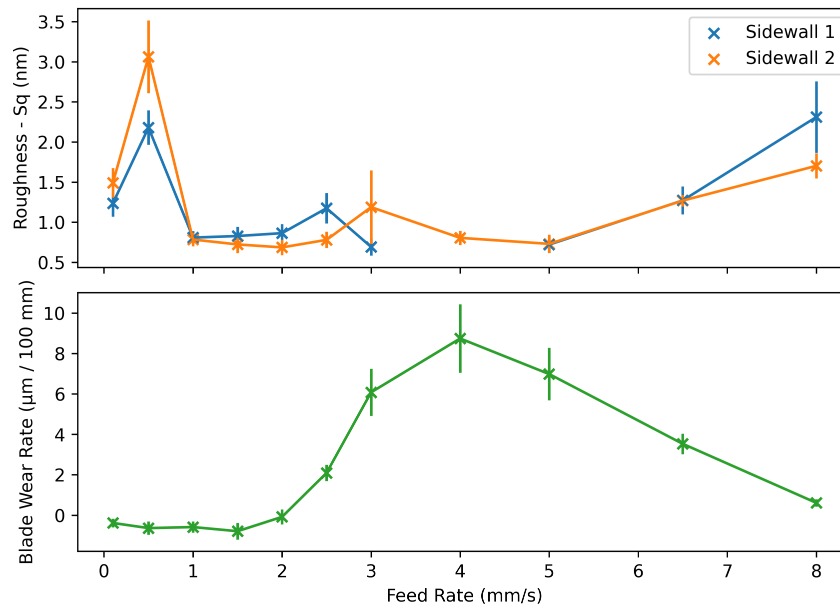

FIGURE 4.11: Chart displaying the roughness and blade wear rate for a range of machining feed rates for silicon.

of the surface area was found to be carbon. This also prevented accurate roughness measurements.

Silicon displayed no true correlation between surface roughness and blade wear rate. Similar to the lithium niobate tests, the perceived wear rate experiences a sharp increase after 4 mm s^{-1} due to high wear before the first measurement sites, however, as shown in Figure 4.11, a noteworthy result is observed. At feed rates below 1 mm s^{-1}, the blade wear rate is negative. This means that the trench depth is increasing due to higher blade engagement and less flexing. This is confirmed by the higher surface roughness at these lower speeds, which is indicative of rubbing. The blade begins to engage properly at 1.5 mm s^{-1}, leading to an increase in wear rates and a subsequent decrease in surface roughness. This result is significant as it displays a minimum feedrate for obtaining ductile machining in the physical machining of optics context. Further investigations are needed to explore these specifics and determine whether this behaviour varies with different blade binders, and/or grit sizes.

For silica, the blade wore extremely rapidly, leaving only an approximately 3 µm, depth of cut, which prevented sidewall roughness measurements. Only the measured feed rate is displayed in Figure 4.12. The observed trend is inconclusive due to the extreme wear rate in the initial few millimeters. Further studies are necessary to gain a better understanding of the dynamics involved, with harder wearing blades and much lower feed rates, however, DAD 3430 is not capable of dicing with feed rates below 0.05 mm s^{-1}.

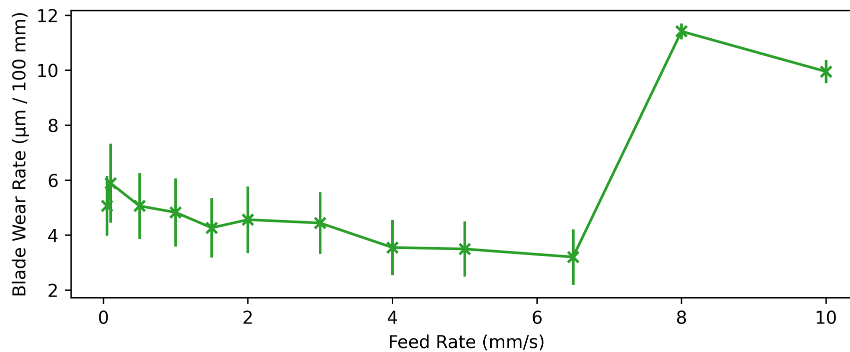

FIGURE 4.12: Chart displaying the blade wear rate for a range of machining feed rates for silica.

4.5 Conclusion

The first experiment investigated the long-term evolution of physical machining in lithium niobate using two depths of cut (50 and 100 µm) and two blade shapes (round and square) as starting conditions. All conditions, except for the 50 µm deep square starting condition, trended towards a similar depth within the first meter of cutting. This suggests that there is a ”stable” depth of cut that blades naturally reach during extended cutting for a given feed rate and blade choice. The 50 µm deep square starting condition exhibited linear wear but remained the most consistent across all parameters discussed. Despite the 100 µm and 50 µm deep square starting condition achieving similar symmetry and depth after the initial meter. This variation underscores the importance of initial parameters in long-term machining performance, likely due to issues such as blade pore clogging affecting consistency.

The cut width remained relatively stable throughout the test, with square blades maintaining their width better than round blades. The experiment found that round blades were more sensitive to issues like wafer curvature and bed variation, making them less suitable for ridge waveguide formation, which requires precise width control. Square blades showed better stability and shape consistency, enabling consistent trench geometry and improved optical performance.

Square blades remained square throughout the cutting process, while the round blades gradually trended towards becoming squarer over time. The ”W-ratio” was introduced as a measure of uneven blade wear, and it was higher for the 50 µm round blade with the other blades staying statically non-”w”, suggesting poor blade loading. The 50 µm round blade also exhibited increasing instability, highlighting how once instability occurs, it can escalate further.

Surface roughness and top-side chipping varied between the starting conditions but did not change significantly over the duration of the cutting. The 100 µm square blade consistently produced the smoothest surface, and the square blades experienced the

least chipping. Notably, the initial blade conditions had long-term effects on the resulting form, surface roughness, and chipping, despite the blades eventually tending towards the same shape. Overall, square blades were more stable and produced more consistent cuts, making them more suitable for applications like ridge waveguides.

The second experiment tested the hypothesis that minimum blade wear rate corresponds to minimum surface roughness, based on the premise that ductile machining results in lower wear. This hypothesis was found to be false. However, clear regime changes in surface roughness and wear rates were observed in silicon and lithium niobate, with low surface roughness corresponding to lower wear rate, but not necessarily the best wear rates as displayed in Figure 4.11. The reasons for these discrepancies remain unclear, and further work is needed to understand the underlying causes and advance towards deterministic machining. Potential factors include the choice of blade material, as standard resin blades used in this study may clog when machining certain materials. A softer blade is likely required for silicon and lithium niobate, while a nickel blade, which is harder wearing, is likely required for silica and might exhibit different wear and surface roughness correlations [12–14].

These findings suggest further optimisation of blade parameters (potentially as being machined) and verification of wafer and bed flatness is required to achieve more deterministic machining results.

References

1. Carpenter L, Berry S, and Gawith C. Ductile dicing of $LiNbO_3$ ridge waveguide facets to achieve 0.29 nm surface roughness in single process step. Electronics Letters 2017; 53. eprint: https://onlinelibrary.wiley.com/doi/pdf/10.1049/el.2017.2863:1672–4. DOI: 10.1049/el.2017.2863
2. Courjal N, Devaux F, Gerthoffer A, Guyot C, Henrot F, Ndao A, and Bernal MP. Low-loss $LiNbO_3$ tapered-ridge waveguides made by optical-grade dicing. Optics Express. 2015 Jun 1; 23. Publisher: Optical Society of America:13983–90. DOI: 10.1364/OE.23.013983
3. Caspar A, UlUac G, Suarez M, Calero V, Bernal MP, Courjal N, Roussey M, Häyrinen M, Laukkanen J, Honkanen S, and Kuittinen M. High-aspect-ratio electro-optical ridge waveguide made by precise dicing and atomic layer deposition. *2017 Conference on Lasers and Electro-Optics Europe & European Quantum Electronics Conference (CLEO/Europe-EQEC)*. 2017 Conference on Lasers and Electro-Optics Europe & European Quantum Electronics Conference (CLEO/Europe-EQEC). 2017 Jun :1–1. DOI: 10.1109/CLEOE-EQEC.2017.8086602

4. Gerthoffer A, Guyot C, Qiu W, Ndao A, Bernal MP, and Courjal N. Strong reduction of propagation losses in LiNbO3 ridge waveguides. Optical Materials 2014; 38:37–41
5. Volk MF, Suntsov S, Rüter CE, and Kip D. Low loss ridge waveguides in lithium niobate thin films by optical grade diamond blade dicing. Optics Express. 2016 Jan 25; 24. Publisher: Optica Publishing Group:1386–91. DOI: 10.1364/OE.24.001386
6. Courjal N, Guichardaz B, Ulliac G, Rauch JY, Sadani B, Lu HH, and Bernal MP. High aspect ratio lithium niobate ridge waveguides fabricated by optical grade dicing. Journal of Physics D: Applied Physics 2011; 44:305101
7. Gray AC. Nonlinear optical components and systems for quantum technologies and communications. en. PhD thesis. Zepler Institute for Photonics and Nanoelectronics, 2021 :184
8. Gray AC, Berry SA, Carpenter LG, Gates JC, Smith PGR, and Gawith CBE. Investigation of PPLN Waveguide Uniformity via Second Harmonic Generation Spectra. IEEE Photonics Technology Letters 2020; 32:63–6. DOI: 10.1109/LPT.2019.2957199
9. Chauvet M, Henrot F, Bassignot F, Devaux F, Gauthier-Manuel L, Pêcheur V, Maillotte H, and Dahmani B. High efficiency frequency doubling in fully diced $LiNbO_3$ ridge waveguides on silicon. Journal of Optics 2016 Jul; 18:085503. DOI: 10.1088/2040-8978/18/8/085503
10. Wang X, Yuan Z, Zhuang P, Wu T, and Feng S. Study on precision dicing process of SiC wafer with diamond dicing blades. Nanotechnology and Precision Engineering (NPE) 2021; 4
11. Chen ST and Guo JP. Reconditioning of diamond dicing blades via electrolytic dressing. Journal of Materials Processing Technology 2023; 311:117801
12. Loadpoint Ltd. MicroAce Manual Series 3. 2002
13. Yuan Z, Feng S, and Wu T. Preparation and characterization of ultra-thin dicing blades with different bonding properties. The International Journal of Advanced Manufacturing Technology 2022 :1–16
14. Yuan Z, Cheng K, Zhang Y, Hu J, and Zheng P. Investigation on the fabrication of dicing blades with different sintering methods for machining hard-brittle material wafers. Proceedings of the Institution of Mechanical Engineers, Part B: Journal of Engineering Manufacture 2019; 233:1781–93

Chapter 5

Machining for Photonic Waveguides

5.1 Introduction

Waveguides and facets are two of the main building blocks of photonic devices, and integrated optics. Waveguides are a critical component of integrated optics, they allow in-device and in-plane guiding and interfacing with the optical mode. The interface of a propagating mode has an extremely low tolerance to uniformity, with significant propagation losses and any processes using non-linear effects will suffer diminished efficiency. The finish of the final surfaces are important as well due to various propagation losses that occur when the mode sides encounter rough areas, though this effect does diminish quickly. Top side chipping will also diminish the optical performance of the waveguides, especially deeper chips that enroach on the optical mode, causing scattering effects and effective refractive index (n_{eff}) changes within the waveguide. This is a key issue with non-linear processes since n_{eff} and phase matching between multiple wavelengths is critical.

Facets are the main method of coupling light in and out of waveguides, photonic integrated circuits and many more interfaces. Any defect in the facet finish can have a catastrophic effect on coupling efficiencies, leading to further facet damage if the powers involved are high enough. Facets must be smooth, typically with a sub 5 nm surface roughness, preferably sub nm range. This is why facets are physically machined using the ductile regime, allowing for the best coupling performance. Form must also be controlled, especially facet angles if coupling between two interfaces in a medium with a lower refractive index. Any angle mismatch is likely to increase Fresnel reflection losses. Diamond sawing is a way to single-step process facets, without any further polishing steps, reducing costs and prices significantly.

This chapter will study the form control of waveguides by changing the thickness, therefore the stiffness, of the diamond blade, to improve the optical performance of

PPLN ridge waveguides. Firstly, the chapter discusses the principles of frequency conversion in optical materials as a background introduction. Once the topics have been introduced, the experiment and results shall be discussed.

5.2 Performance of Wide vs Narrow Blade Machined Ridge Waveguides

This is an investigation of waveguide uniformity to improve the optical conversion performance of various LN ridge waveguide devices. The primary target is to extend the practical wavelengths supported by LN further. One requirement of this is to have highly uniform ridge waveguides, since the shorter the target wavelength, the tighter the tolerances are on the fabrication steps.

This section introduces non-linear conversion, then phase matching requirements to explain the need for tight constraints on the ridge waveguide uniformities, before moving onto the experimental section.

5.2.1 Nonlinear Frequency Conversion

Typically for frequency conversion, a material's non-linear response is used to convert the input power to the output wavelength with some level of efficiency. When light interacts with a material, the electromagnetic field will cause momentary oscillations at a subatomic level. For most materials these oscillations will have no effect on the emitted light, however in certain materials, the oscillations can trigger sub-oscillations with a non-linear response. These can be second, third, fourth etc order responses depending on the material, and are characterised by the non-linear $X^{(n)}$ coefficients, where n represents the order. Here, the focus is on lithium niobate due to the transmission band being large from 400 nm through to 5 µm and high $X^{(2)}$ value, as well as a wealth of experience and interest in this field.

Many alternative non-linear optical materials exist, two keys materials are Potassium titanyl phosphate (KTP) and Lithium Tantalate (LT). KTP is largely used for quantum optics due to a high overlap with telecommunication C-Band, and the electro-optical properties are of interest in many research and commercial fields. LT is similar to LN, however has a lower transmission band, being as low as 277 nm. However, LT has a lower 2nd order optical conversion parameter than LN, therefore LN will outperform LT for many applications, except for UV/blue conversions. Little work has been carried out on LT for this reason and the lack of suitable dopants, though some commercial applications exist.

To get high efficiency wavelength conversion, high intensities are generally required to trigger the non-linear responses, and phase matching to make use of it. To obtain high intensities, laser resonant cavities, pulsed lasers or narrow waveguides are typically used. This work will use narrow ridge waveguides (7 µm) as a method of obtaining the high intensities required, with relatively low input power of 300 mW.

5.2.1.1 Phase Matching

To efficiently change wavelengths, phase matching is required to keep the complex amplitude components of the conversion the same direction, resulting in unidirectional power flow, as displayed in Figure 5.1. This is the process of which the phase relationship between the signal and pump waves is maintained as it is propagating through the device. The phase matching condition is $k_{\text{signal}} = 2 * k_{\text{pump}}$, where k is the wavenumber of the pump and signal waves. This also typically requires control of dispersion and polarisation to be successful. Normally bifrefrigent phase-matching is used to correct the phase mismatch, with the one polarisation being the pump and the other polarisation being the signal waves. To get the refractive indexes to fulfil the phase matching condition exactly for the most optimum efficiency, temperature sweeps are required to find the optimum temperature according to the thermo-optical effect. The refractive index dependency on the wavelength and temperature is well known to follow the empirical Sellmeier equation [1, 2], therefore by changing the temperature, the wavenumbers are changed and thus temperature can be used to correct the phase mismatch [3].

An alternative for phase matching is quasi-phase matching, which removes the polarisation constraints, at the cost of reducing the non-linear coefficient by a factor of $2/\pi$. Despite this, due to the polarisation direction being the same direction for both of the waves, allowing for more power transfer, it can still be more efficient in practice than true phase matching.

Quasi-phase matching (QPM) was first introduced in 1962 by Armstrong et al. [4], and effectively consists of changing the sign of the complex amplitude components of the conversion when the energy transfer vector starts trending backwards, resetting the energy transfer direction. This is also displayed in Figure 5.1. QPM is carried out by periodically poling the crystals, such that the crystal domain axis flips periodically, meaning the sign of the d_{33} tensor changes. In LN, this is carried out by using electric fields to induce a change in the domain direction, using the ferroelectric properties of LN as displayed in Figure 5.1. Like in true phase matching, QPM requires temperature sweeping to find the exact phase matching condition, however, due to the poling, this can be controlled to be significantly lower temperature than in true phase matching processes.

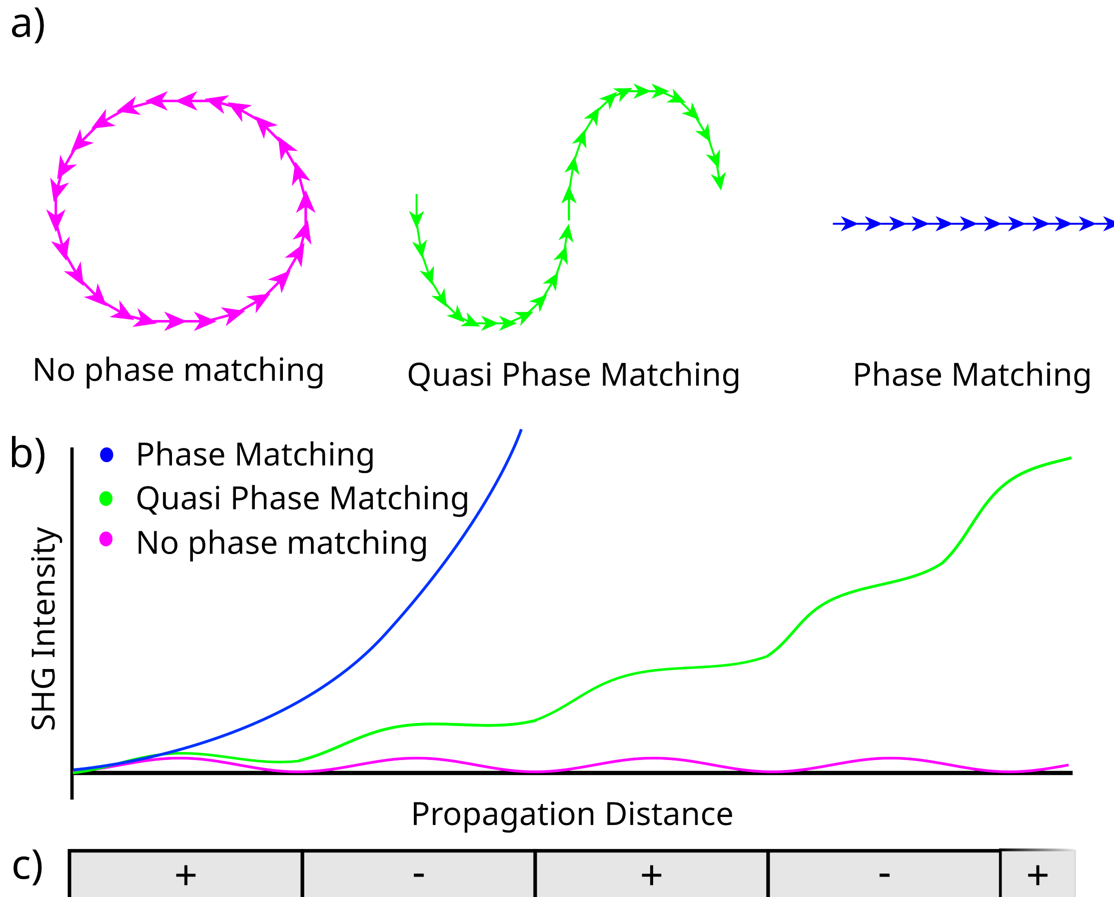

FIGURE 5.1: a) Phasor diagrams indicating the energy transfer direction and magnitude as a result of phase matching, quasi phase matching and no-phase matching. b) Chart displaying the resulting SHG intensity as a result of the three phasors displayed in a). c) Corresponding poling diagram for the phase matching in b).

5.2.1.2 Waveguide Uniformity

To have highly efficient ridge-waveguides, the mode overlap between the pump and signal waves is required to be kept the same throughout the length. Any width variation along the length of the waveguide will cause distortion of the modes, and due to the different wavelengths, the modes distort differently, reducing their effective overlap, and limiting the resulting power transfer between the modes. Few studies have investigated the waveguide uniformity on the resulting phase matching spectra. These will be discussed below.

Chavuet et al, numerically modelled a LN ridge waveguide with a linear variation and calculated that a 200 nm ridge width deviation would cause a two-thirds loss in the maximum efficiency [5]. Chauvet also highlighted that a larger linear ridge taper can cause two phase matching peaks in a LN device, causing a catastrophic efficiency loss. This highlights the importance of controlling the ridge width, even down to significantly sub micron. This is the main reason that this work characterises the width variation of typically fabricated ridge waveguides. The confocal microscope system

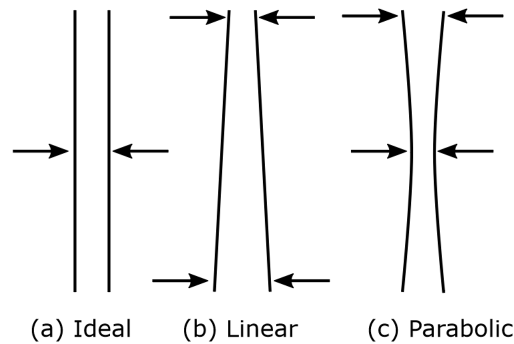

FIGURE 5.2: Diagrams displaying the modelled waveguide shapes by Gray. a) is the ideal 6.8 µm wide ridge waveguide, b) is a linear width variation and c) is a parabolic curve. Taken from [8]

allows further investigations into the causes, identifying the cut locations directly on the device, allowing for longer form errors to be identified. Furthermore, while targeting a different non-linear process, spontaneous parametric down conversion, Satandrea et al, highlighted that while random waveguide variational noise has little effect on the phase matching spectrum, low frequency noise on the waveguide width does have significant effect on the resulting phase matching spectrum [6, 7].

To further characterise the effect of uniformity of a waveguide on phase matching spectra, Gray [8] modelled three ridge-waveguides, all targeting 1560 nm to 780 nm SHG, as displayed in Figure 5.2. The first was a perfectly straight, ideal 6.8 µm wide waveguide, second was a waveguide with a linear width variation, and third was a parabolic curve. Two witdh variation magnitudes are considered, 60 nm and 540 nm. The resulting phase matching spectra are in Figure 5.3. Comparing Figure 5.3a to Figure 5.3c and Figure 5.3d to Figure 5.3f, indicates a significant drop in efficiencies as a result of the change in magnitude of the SHG intensities, with both decreasing an order of magnitude. This is a significant drop, and both variation magnitudes are not unplausible with modern dicing machines, given that current machines are rated to 1 µm cut straightness variation over 200 mm, before considering blade flutter and flex. This further highlights the requirement for exceedingly consistent and precise physical machining of ridges.

To summarise, to extend the practical usage of wavelength conversion into shorter wavelengths and to increase efficiency of the waveguides, the machining stability needs to be improved since the tolerance of width and straightness decreases non-linearly with the wavelength. Width and straightness are critical to keep consistent, and as close to nominal widths as possible. Therefore, this experiment proposes the usage of a thicker blade, providing more machining stability and less blade flutter and wander to provide better width uniformity, therefore significantly improving the SHG conversion.

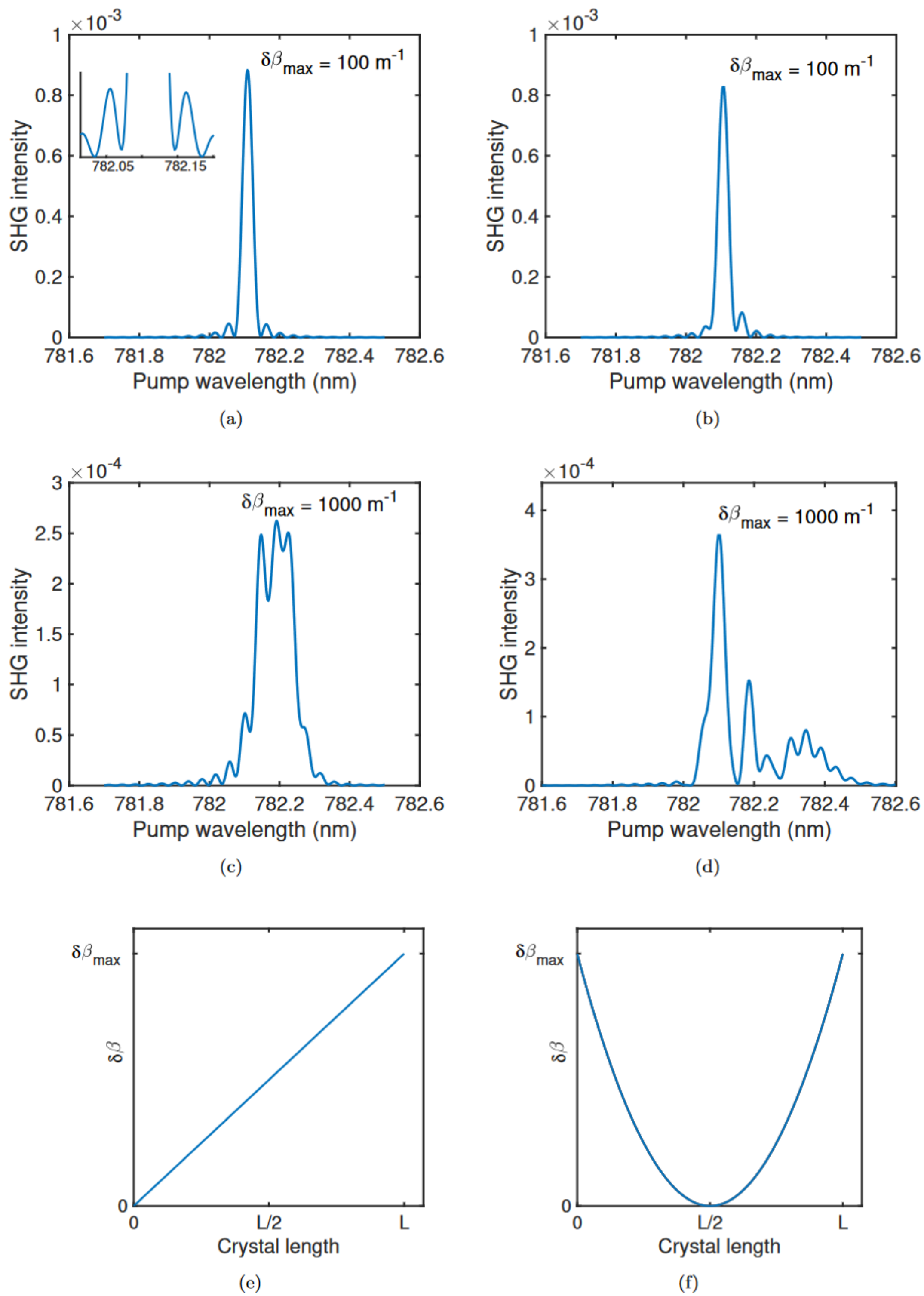

FIGURE 5.3: Charts displaying Grays modelled resulting phase matching spectra [8]. The left and right columns represent the linear width variation and the parabolic curve respectively, as displayed in e) and f). $\delta\beta$ represents the width change along the length. Two maximum width variations are modelled per shape variation, the top spectra consider a 60 nm variation, and the middle spectra represent 540 nm variation.

5.2.2 Experimental

In this experiment, four devices were fabricated using the process discussed in Figure 2.5. A thin layer of metallic zinc (typically 100-200 nm) is deposited on a 5% MgO doped lithium niobate wafer, then the layer is diffused into the surface by using a high temperature oven [9], to provide vertical confinement of the mode by creating a planar guiding layer. Periodic poling is performed first for SHG, and is performed by applying a high voltage across the wafer, with a periodic photoresist pattern providing the pattern of the poling. Next is diamond machining of the ridges, defining the optical lateral confinement, carried out on a Disco DAD 3340.

With this particular wafer for the purpose of experimentation, two ridges were machined per device, targeting a nominal ridge width of 7 µm. One ridge was fabricated with the 300 µm kerf blade and the other was fabricated with the 100 µm kerf blade for comparison. A labelled image illustrates this in Figure 5.4. As displayed, the ridge pairs were fabricated next to each other, to remove uncertainty about the effects of planar waveguide and poling uniformity, hence the results will be presented in pairs. The cutting parameters were chosen from the results of Chapter 4 for optimum cutting stability; 2 $mm\,s^{-1}$ translation speed, 20,000 rpm spindle speed and a depth of cut of 30 µm. The facets were single-step machined, with 0.1 $mm\,s^{-1}$, 20,000 rpm spindle speed and depth of cut of 40 µm, providing an optical quality surface finish for coupling. Both of the waveguide facets were machined in the same pass, keeping the surfaces directly comparable. One device was found to be faulty, so this device is labelled S4 in this work, with the functioning devices labelled S1-3.

The three remaining devices were optically profiled by Noelia Palomar Davidson, who performed the temperature sweeps to obtain the phase matching spectra, and conversion efficiencies for each of the devices. The experiment schematic is shown in Figure 5.5. After the spectra had been obtained, the samples were profiled with the confocal scanner, described in Chapter 3, for straightness and width variation, and finally the offcuts were singulated for sidewall surface roughness measurements on the Zygo Zegage.

5.2.3 Results & Discussion

The resulting phase matching spectra are displayed in Figure 5.6 with the normalised efficiencies displayed on the right for the purpose of spectra comparison. It is immediately obvious that the 300 µm machined ridges perform significantly better than the 100 µm machined ridges with the average improvement being 226%. Also of note is that the spectra for the 300 µm consistently fits the expected sinc^2 profile better, with symmetrical lobes that reach near zero. This is all indicating a more uniform mode overlap and phase matching condition, therefore a more consistent ridge width.

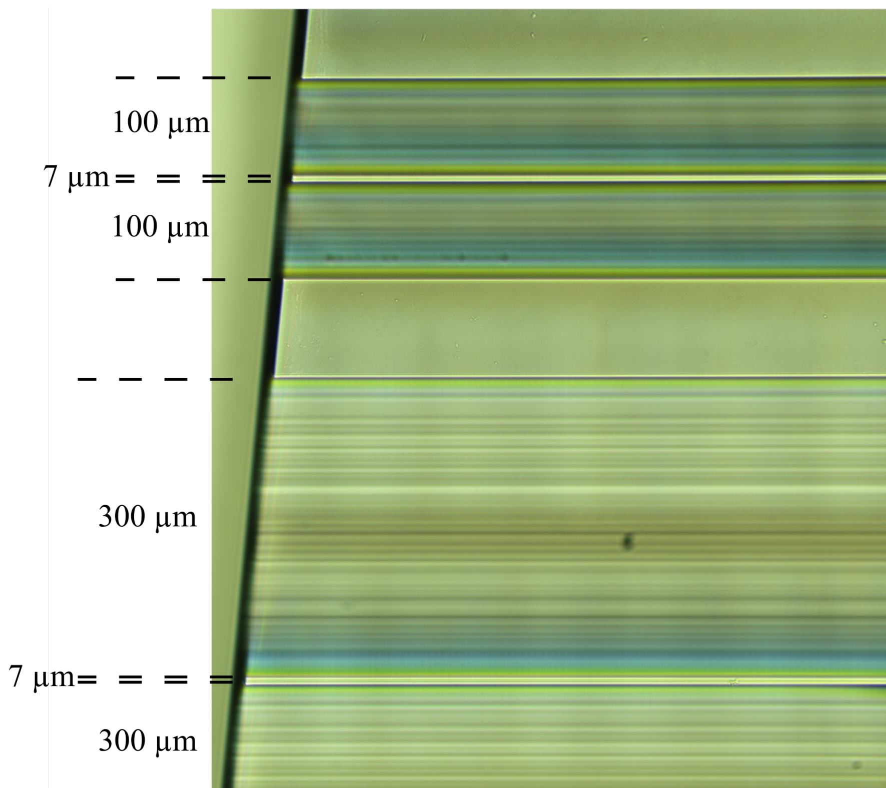

FIGURE 5.4: Labelled microscope image of 100 µm and 300 µm kerf blade machined ridge waveguides. The facets are machined at 7° to minimise coupling losses by enabling a wider angle of acceptance relative to the input beam [10].

Multiple investigations were carried out to identify the cause of the efficiency improvement and to rule out other fabrication differences comparing the two blade widths. Starting with the width variation, and straightness. Then top-side chipping and surface roughness are evaluated.

The widths along the length of ridge waveguide are displayed in Figure 5.7, with the accumulative width deviation across the length displayed in Figure 5.8 and straightness displayed in Figure 5.9. All of the ridges are slightly wider than the nominal ridge width of 7 µm, with them being about 3-5 µm wider, indicating that both of the blades are marginally narrower than their specified widths. Given the overlap of the S2 and S3 ridge widths, this does not matter significantly from a comparison point of view, and given that the S1 100 µm machined ridge is closer to the nominal width and yet still performed significantly worse optically than the 300 µm, further indicates that the average ridge widths are not the significant factor behind the lower efficiencies. It shows that despite a better average ridge width, the mode overlap of the more width consistent ridge waveguide is still better, implying that straightness of the two trenches that make up a ridge waveguide is more important than the ridge width to a point. The S3 100 µm machined ridge has clearly had some sort of machining defect in the fabrication, with the sinusoidal variation between 15 and 30 mm and the rapid shift after indicating that the dicing blade had

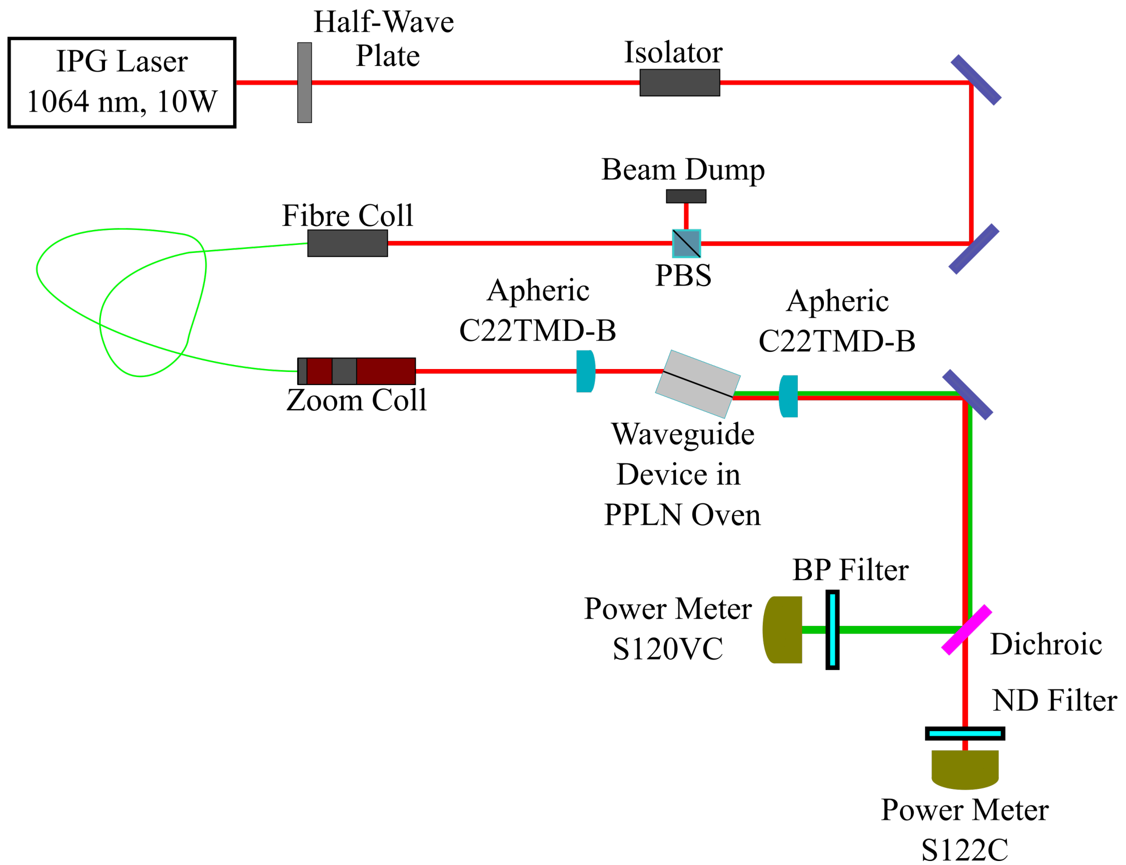

FIGURE 5.5: Schematic of the experimental setup for the wide vs narrow temperature sweeps.

either bent and course corrected, or that the dicing saw slider had drifted and the controller brought it back to the required location causing a rapid change in position.

To further examine the width variation along the length, the accumulative width variation along the ridge length was plotted in Figure 5.8. This provides a quality factor as ridge width is proportional to n_{eff} and thus phase error. It is immediately clear that the 300 µm machined ridges are more uniform in width than the 100 µm machined ridges, which confirms the theory that the improved efficiency is due to the wider blades providing more machining stability and more uniform ridges. However, the fact that S1 and S2 have similar features in similar places does imply that there is an issue with the uniformity of either the wafer (i.e warpage) or the air slider. Very careful further investigations are required to identify the cause.

Straightness of the ridges is evaluated by usage of the confocal microscope to locate the ridge edges, then taking the midpoint as the mode mean path. This is presented in Figure 5.9. The general curvature is very similar across all of the sections, implying that either the air-slider or the wafer is curved, or that the blade torque caused wafer chuck rotation. The most likely cause from internal observations is that the wafer was curved when machining was performed, then when released, the ridge waveguides became curved as a result of the strain. Otherwise the general trend is approximately

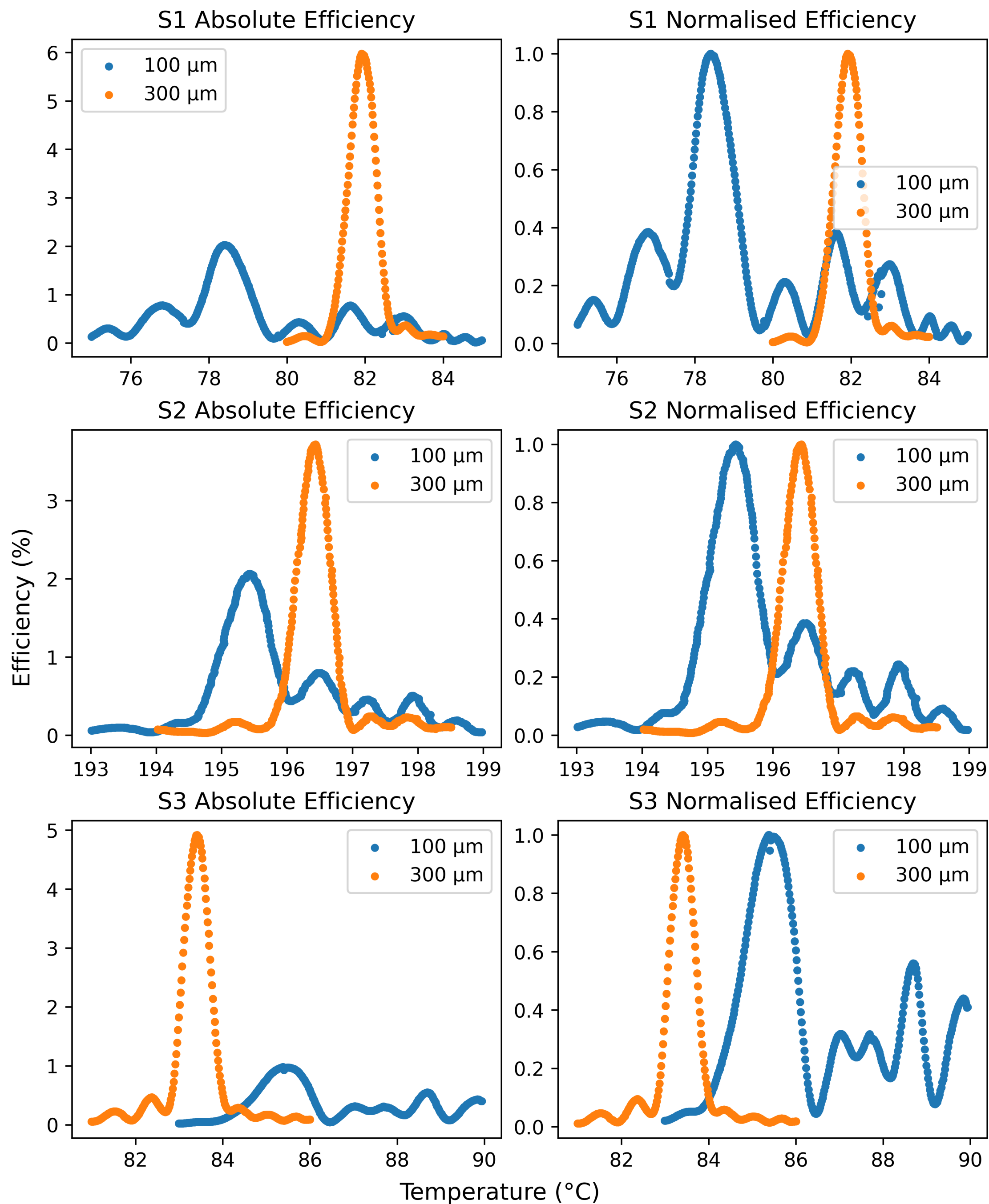

FIGURE 5.6: Chart displaying the resulting fundamental to fundamental phase matching efficiency vs temperature waveguide sweeps. Left column is the absolute efficiency. The right is normalised efficiency for the purpose of spectra comparison. Data collection performed by Noelia Palomar Davidson.

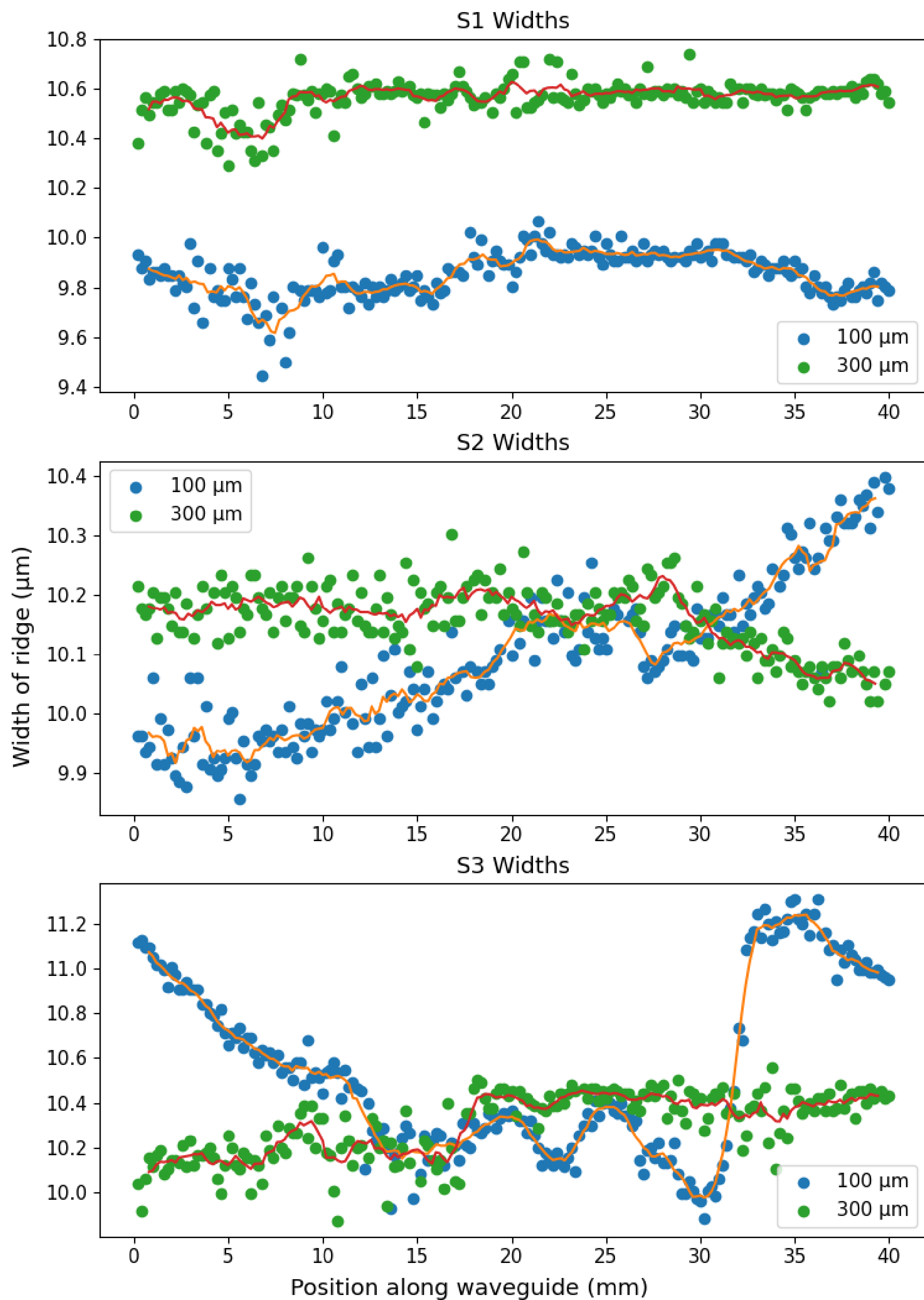

FIGURE 5.7: Width uniformity along the length of the working ridge waveguides (1-3). A rolling average over 30 points is used to smooth the points for analysis. Data obtained with the confocal scanner.

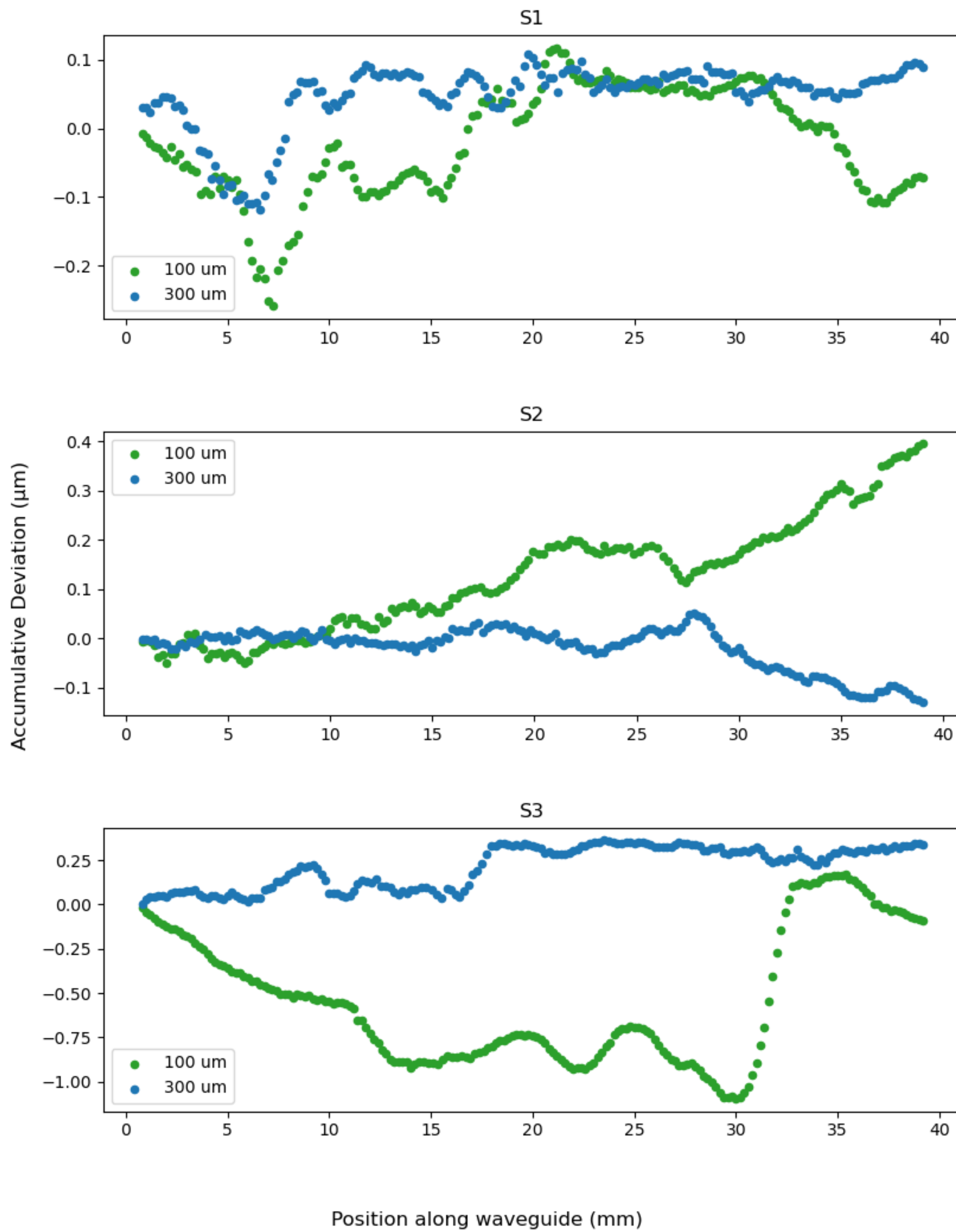

FIGURE 5.8: Chart of accumulative width variation along the waveguide lengths.

sub 1.5 µm variation over a 40 mm length of cut, which is within the machine specifications, and for S1 and S2, is generally of a slow rate of change and are similar enough that straightness can be ruled out as a significant contributing factor to the improvement in the SHG performance. The exception is in S3, where there is a rapid rate of change around the 30 to 35 mm mark in the straightness and the width of the 100 µm blade machined cut, which explains the 5x worse optical performance in the 100 µm machined ridge over the 300 µm machined ridge. The straightness having approximately half of the width deviation means that only one cut was the cause of the anomalous result. It is unknown whether the controller on the DAD 3340 corrects the y-axis position midcut, or whether the blade bent.

The topside chipping data was obtained using the processed documented in Chapter 3 and is shown in Figure 5.10. It indicates several things, the first is that the blade is clearly slightly anti-symmetrical when cutting, which can be due to many factors, though this is likely to be either the spindle not being completely perpendicular to the cutting direction or the blade weighting or lapping finish is anti-symmetrical. There is a general upwards trend as well, indicating that the chipping is increasing as the cuts increase, indicating blade wear or clogging. But on average the top side chipping is marginally worse on the 300 µm cut ridge waveguides over the 100 µm. This low chipping in combination with the mode depth as discussed in Chapter 3, rules out chipping as a factor that explains the increase in efficiencies with the 300 µm cut waveguides.

Table 5.1 is the sidewall surface roughness, characterised by singulation of the off-cuts and then profiling with the Zemetrics Zegage, with sites displayed in Figure 5.11. A Gaussian 1 µm spline fit is used to remove the curvature of the blade. Taking the average of these results, the 100 µm blade gives 0.2495 ± 0.0011 nm Sq and the 300 µm blade results surface roughness of 0.2704 ± 0.0006 nm Sq. The 100 µm cut ridges are marginally smoother than the 300 µm cut ridges, however, all of the ridges are well within sub-nm roughness, ruling out the roughness as being a factor for the significantly increased optical-conversion performance.

5.3 Conclusion

An extended investigation into ridge waveguide uniformity was carried out, targeting the improvement of SHG performance in 1064 nm to 532 nm non-linear conversion. This has very high machining tolerance requirements. Two blade widths have been used, 100 µm and 300 µm, to fabricate ridge waveguides, with a resulting average optical performance improvement of 226% of the 300 µm wide over the 100 µm wide machined ridges. The investigation highlighted the significantly improved width uniformity as the cause of the improvement in optical performance, due to the

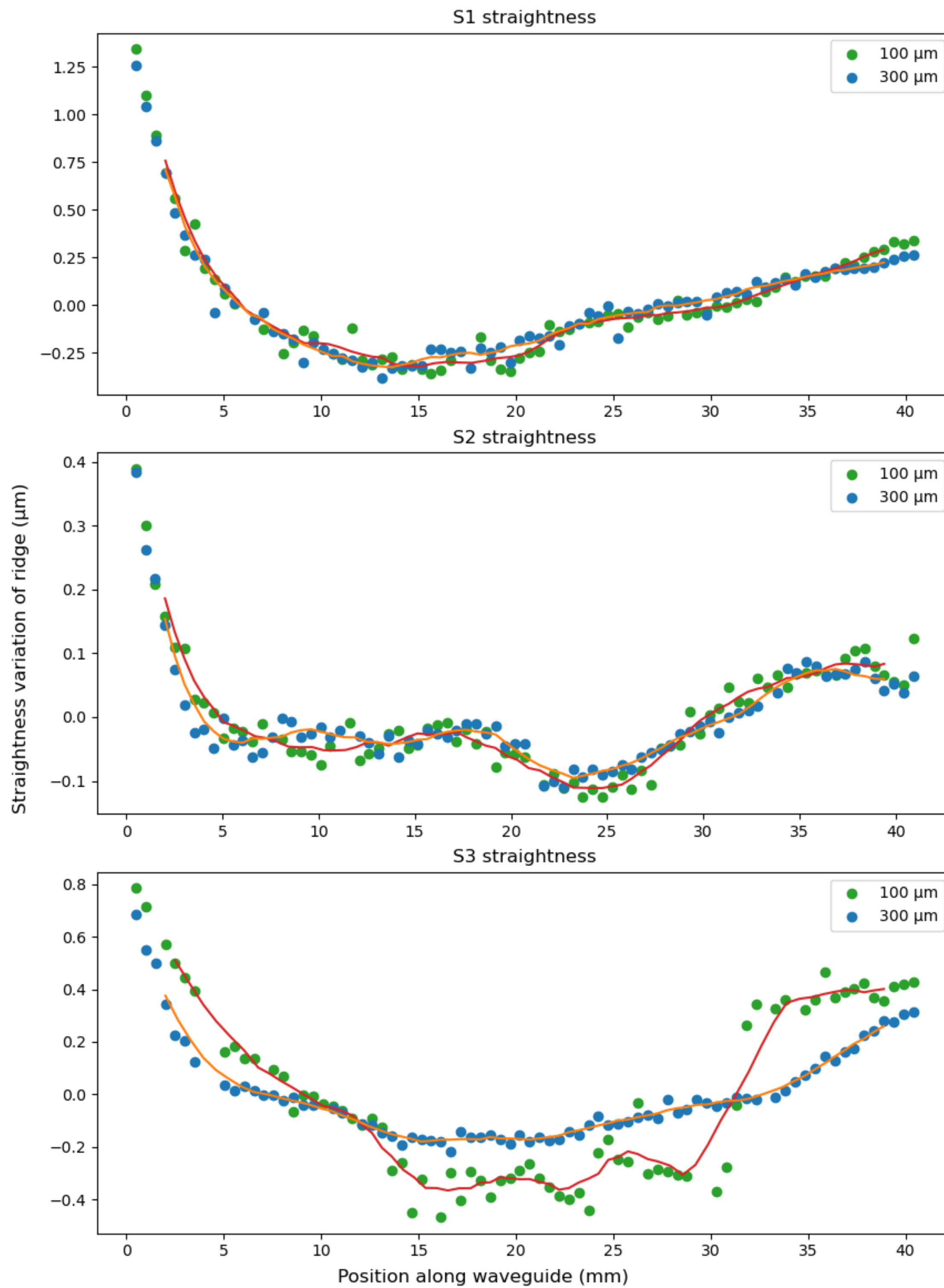

FIGURE 5.9: Chart of straightness along the length of the working ridge waveguides (1-3). A rolling average over 30 points is used to smooth the points for analysis. 0 represents the mean y position of the ridge. Data obtained with the usage of the confocal scanner.

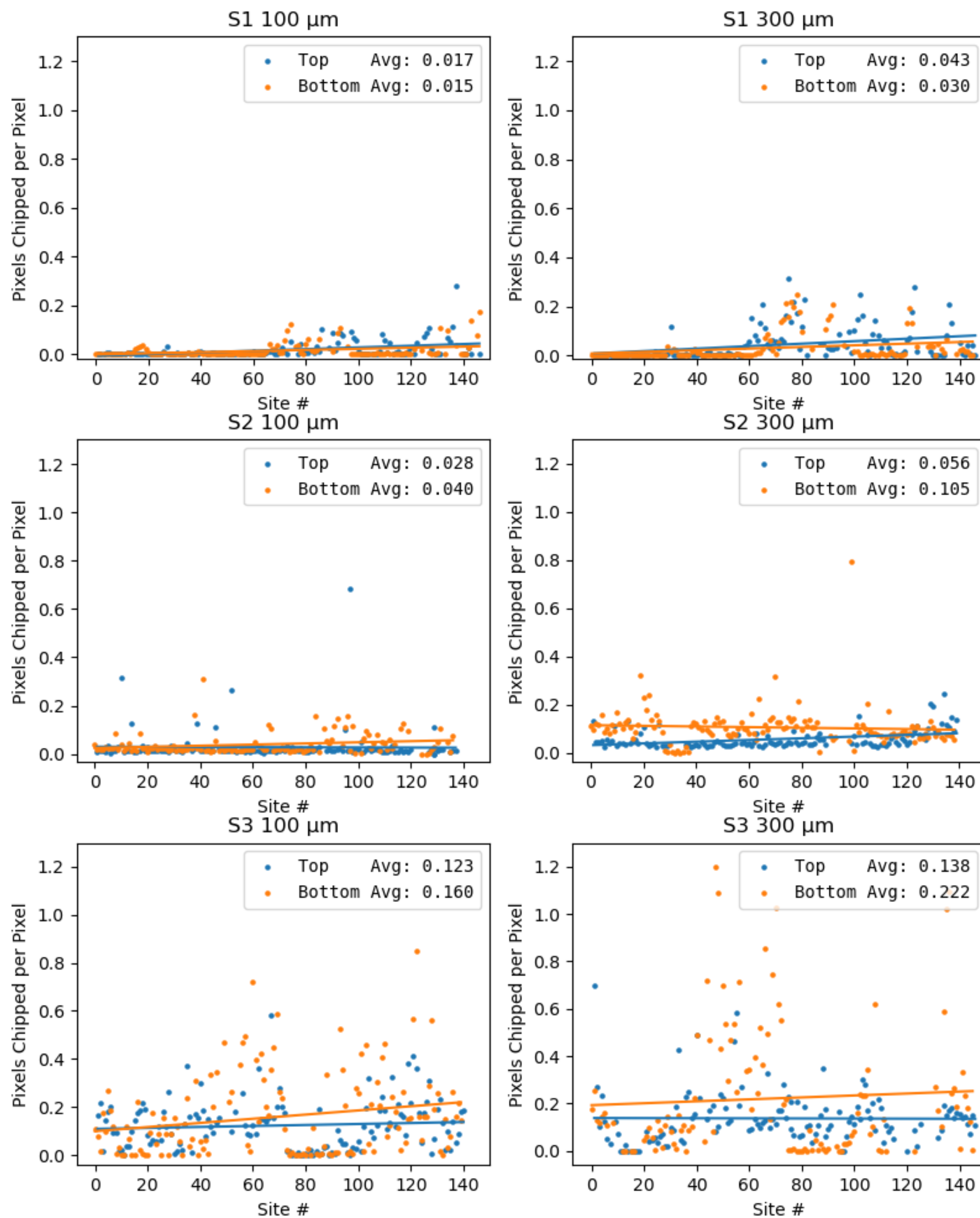

FIGURE 5.10: Chart displaying the chipping results for the three wide vs narrow blade cut data. Starting at approximately 2 mm from the start of the waveguide, with sites evenly spread out along the length of the waveguide. Top and bottom represent the relative sides of the waveguide to indicate differences between the blade cuts.

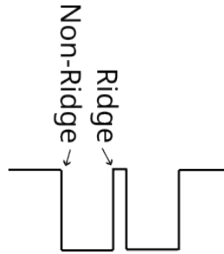

FIGURE 5.11: Diagram displaying the CSI scan sites for Table 5.1.

	Ridge 100 µm		Ridge 300 µm	
	Average Sq (nm)	StdErr (nm)	Average Sq (nm)	StdErr (nm)
S1	0.1506	0.0042	0.3783	0.0058
S2	0.2072	0.0038	0.1977	0.0027
S3	0.1738	0.0031	0.2535	0.0036
S4 (broken)	0.1799	0.0073	0.2501	0.0061

	Non-Ridge 100 µm		Non-Ridge 300 µm	
	Average Sq (nm)	StdErr (nm)	Average Sq (nm)	StdErr (nm)
S1	0.1514	0.0120	0.1746	0.0028
S2	0.4381	0.0109	0.3027	0.0047
S3	0.3973	0.0111	0.2880	0.0096
S4 (broken)	0.2976	0.0180	0.3184	0.0041

TABLE 5.1: Table of the average sidewall roughness (Sq) of the 300 and 100 µm machined ridges. The ridge values are the ridge sidewall values, the non-ridge are the opposing sides of the same cut for comparison as displayed in Figure 5.11.

superior stability of the wider blades. It also highlighted no significant surface roughness and top-side chipping changes between the blades.

The cut straightness measurements identify heavy curvature of up to 1.2 µm though is it technically within machine specification. The exact reasoning is unclear, but is theorised to be due to wafer curvature, bed mounting or torque caused by the dicing blade. It is unlikely to be due to blade wear, because observations have seen sub 0.1 µm wear while performing similar work. The width accuracy is poor, with all of the ridges being 3-5 µm wider than nominal, however, this is a trivial fix of performing better blade kerf measurements. 1.2 µm over 40 mm is impressively good compared to etching processes, however, does still leave room for improvement. Further investigations should examine the wafer curvature, bed flatness, blade curvature and stage to spindle squareness in more detail, for better machining of grooves.

References

1. Liu BW, Han ZQZ, Li JP, Wang XH, Li YH, Zhou ZY, and Shi BS. Sellmeier equation for the refractive index of ordinary light in 5 mol.% MgO-doped

congruent lithium niobate. Opt. Express 2025 Jan; 33:1163–72. DOI: 10.1364/OE.547726

2. Schlarb U and Betzler K. Refractive indices of lithium niobate as a function of temperature, wavelength, and composition: A generalized fit. Phys. Rev. B 1993 Dec; 48(21):15613–20. DOI: 10.1103/PhysRevB.48.15613
3. Fejer M, Magel G, Jundt D, and Byer R. Quasi-phase-matched second harmonic generation: tuning and tolerances. IEEE Journal of Quantum Electronics 1992; 28:2631–54. DOI: 10.1109/3.161322
4. Armstrong JA, Bloembergen N, Ducuing J, and Pershan PS. Interactions between Light Waves in a Nonlinear Dielectric. Physical Review 1962 Sep; 127(6):1918–39. DOI: 10.1103/PhysRev.127.1918
5. Chauvet M, Henrot F, Bassignot F, Devaux F, Gauthier-Manuel L, Pêcheur V, Maillotte H, and Dahmani B. High efficiency frequency doubling in fully diced $LiNbO_3$ ridge waveguides on silicon. Journal of Optics 2016 Jul; 18:085503. DOI: 10.1088/2040-8978/18/8/085503
6. Santandrea M, Stefszky M, Ansari V, and Silberhorn C. Fabrication limits of waveguides in nonlinear crystals and their impact on quantum optics applications. New Journal of Physics 2019 Mar; 21033038:033038. DOI: 10.1088/1367-2630/aaff13
7. Santandrea M, Stefszky M, and Silberhorn C. General framework for the analysis of imperfections in nonlinear systems. Optics Letters 2019 Nov; 44:5398–401. DOI: 10.1364/OL.44.005398
8. Gray AC. Nonlinear optical components and systems for quantum technologies and communications. en. PhD thesis. Zepler Institute for Photonics and Nanoelectronics, 2021 :184
9. Smith P, Ming L, O'Connor M, and Gawith C. Zinc diffused lithium niobate waveguides for high conversion efficiency second harmonic generation. 2005 Jan
10. Tang Y, Ding T, Lu C, Qiu J, Zhang Y, Huang Y, Liu S, Zheng Y, and Chen X. Broadband second-harmonic generation in an angle-cut lithium niobate-on-insulator waveguide by a temperature gradient. Optics Letters. 2023 Mar 1; 48. Publisher: Optica Publishing Group:1108–11. DOI: 10.1364/OL.481649

Chapter 6

Machining for Precision Alignment

6.1 Introduction

In the past 20 years, there has been huge interest in the field of quantum technology and integrated optics, leading to significant advancements in these fields. Work on the integration and miniaturisation of optics and photonics especially in the field of atom/ion traps is of specific interest. Atom and ion traps are critical components of quantum technology. Atom and ion trapping is a technique used to confine and control individual atoms or ions with electromagnetic fields and/or lasers. Usually neutral atoms are trapped using laser and magnetic field combinations, with charged ions trapped by using electric fields with interactions carried out using optics. These devices allow for studying of quantum phenomena [1, 2], gravitational sensing [3–5], accurate atomic clocks [6–8] and development of quantum computers [9–13].

Atom and ion traps have extremely stringent long term alignment requirements on components. The alignment tolerances vary significantly depending on the specific components used, the type of trap, the number of particles, wavelength of the light, and sensing capabilities. Typically for optical trapping of neutral atoms, the misalignment tolerance is on the order of the beam waist, normally low single digit microns [14–18]. For ion traps, the beam misalignment tolerance is normally sub-micron due to the increased precision requirements for cooling and interaction with the states.

Another alignment consideration is the 3D alignment of multiple layers allowing for more symmetrical electrode formats, greater trap depth and easier shuttling of ions through 2D junctions [19–21]. While electrodes are not considered within this work, the proposed platform addresses the 3D alignment of multiple layers. Prior multiple layer ion traps have been fabricated using manual alignment of femtosecond etched silica wafers utilising optical feedback, limiting the alignment precision to tens of

microns, resulting in undesirable micromotion [22, 23]. Day et al. also reported a similar issue due to a beam path misalignment resulting in a 2 μm misalignment in the trapping region [24]. Ragg et al demonstrated a multiwafer alignment method with an impressive 3D alignment tolerance of $\leq$ 2 μm utilising femtosecond laser-enhanced etching of a three point support mechanism [19], however, the geometry is not feasibly physically machined.

Typically, current trap beam alignment systems use a two step active alignment process, a general rough alignment that can automatically or manually place the component with some sort of fixing compound. Then another finer manual alignment is carried out based on feedback loops, before the component fixation, or during the fixation i.e when solder is cooling [25]. The combination of fixation compound, multiple small components and positional feedback sensors add significant complexity to the fabrication of the device, making it an expensive and time consuming method, limiting mass production.

Given the limited miniaturisation of certain atom and ion trap designs, due to multiple free-space components requiring multiple chip based photonic devices, atom and ion traps are an ideal example for the platform development, although the proposed passive alignment platform can be used elsewhere in general miniaturised optical systems, i.e free-space micro-optical benches [26, 27], where hybrid components are aligned to theoretically sub μm tolerances. Both the optical distance and alignment must be strictly controlled to sub-micron precision.

This section has highlighted the need for a highly precise and scalable multi-component alignment system that is capable of aligning complex 3D assemblies consisting of multiple miniaturised optical and photonic components with exceedingly high precision. This chapter introduces the various concepts of alignment, analyse current passive alignment methods. The chapter then proposes the development of a novel passive alignment methodology capable of sub-micron accuracies, targeted towards atom and ion traps, however, this work should be applicable to many areas of optics and photonics. This platform utilises ultra-precision physical machining, finding the limitations of the fabrication method. The design, fabrication and testing shall be discussed, and ultimately the limitations of physical machining encountered in this work.

6.2 Passive Alignment in Optics & Photonics

Passive alignment in optoelectronic and photonics packaging is defined as the technique where component alignment is performed without using active feedback from the component or temporary sensors to position the component and fixed in place. Using active feedback loops to align components is called active alignment.

Passive alignment is primarily used in the assembly of optical fibre interconnectors [28–31], laser diode packaging [32–35] and photonic integrated circuits [36–38]. The main driving interest behind passive alignment, is that it allows for costs to be reduced significantly since the component activation is not required during the alignment steps, simplifying the process of assembly. It also allows for significantly better repeatability of accurate alignment; however the method also places highly stringent accuracy and precision requirements on the fabrication, especially at the sub micron scale.

Passive alignment can be split into two general subsets: elastic and kinematic alignment. Elastic averaging involves incorporating flexibility into the design components (e.g., springs, microcantilevers), allowing the counter-component to elastically self-align within the assembly. This approach is primarily seen in larger devices, where there is more space for complex assemblies and movement.

Kinematic alignment, on the other hand, focuses on absolute constraint of the degrees of freedom, where the aligned components only have one possible resulting position. This method is more challenging to machine since it requires ultra-precise tooling. However, it offers the advantage of being extremely repeatable when executed correctly. Kinematic (or exact constraint) methods rely on constraining the system by matching the number of contact points to the number of degrees of freedom, ensuring the system is statically determinant. Kinematic methods do not appear to be typically used in small-scale photonic platforms because of the highly precise alignment tolerances, design limitations required at such small scale, making it extremely challenging to fabricate on the small scale with 3D physical machining.

Elastic averaging [39–43] is normally used and is based on over-constraining the system, but each constraint point is flexible. This process aligns components with multiple "flexible" attachment points such as hooks, bumps or clamps that are shaped or are flexible to allow sub-optimal alignment interlocking individually, however, these average out to provide an improved overall alignment for the device. The extent of the averaging depends on the specific design used. This has a significant advantage of not requiring expensive nanometer precision tooling, though numerical simulations and/or redesigns are required to improve the current designs.

The elastically averaged devices are capable of aligning to a sub micron accuracy, however, the elastic aligners tend to require significant real estate on the chips and have robustness issues, preventing usage in extreme scenarios such as high temperatures, impact or vibrations. The main reason why this work does not use flexible structures or clamps in this way is that the physical machining technique is not suitable for fabricating 3D complex structure, being limited to straight lines, with limited control over the start and end points. It is hoped that the UPROAR project, a

next generation ultra precision dicing machine, will enable significantly more complex structures and further investigations into alternatives.

Slocum et al [40] used elastic averaging to obtain ±0.2 μm accuracy aligning two 120 mm square aluminium plates with flexures. This is well within the accuracy requirements of fibre alignment, however, the 10 mm sized flexures are difficult to scale down sufficiently for the assembly proposed here, partly due to machining capability, but also due to the brittle nature of optical materials. Flexible locking hooks or similar structures on the sub mm scale are unfeasible which leaves us with the obvious choice of hard components that interlock. An immediate choice is ball bearings or dowels in a set of rounded holes on a multiple layer system. While metal ball bearings are surprisingly consistent in their diameters as the best grade (3) allows for ±80 nm variation in diameter [44], due to containing iron, they are not considered suitable here due to their magnetisation .

Solder-bumping techniques are promising with their alignment accuracy. A notable method is transferred multi-chip bonding (TMB) [43, 45], proposed in 1998 by Akira et al [45], which has been used to obtain ±6 μm accuracy with a stack of four AlN chips of unknown size, with simulations suggesting similar accuracy can be obtained with a stack of up to 18 chips. This process is uncommonly used due to the complexity. A patterned quartz plate is pasted to the substrate as a mask, then a gold-tin alloy solder is flowed in to create the alignment marks. The underside of another chip has the reverse alignment marks created in the same way, and the chips are stacked and bonded by heating the solder which shrinks therefore providing the elastic averaging. Due to the complexity of this setup, usage of metal and the poor height control, this method is deemed not suitable for the platform.

For quantum technology to become truly mainstream, these alignment requirements need resolving, enabling multi-millimeter sized device to device alignment with sub-micron precision. To solve this, this chapter proposes a passive alignment platform where the components including waveguides, lenses and miniaturised integrated photonic chips can be fixed onto a substrate. The passive self-alignment properties are provided by a combination of the high tolerance optical fibre diameters and ultra-precision deterministically machined trenches.

6.3 Assembly Principles

This section proposes a novel U-Groove based deterministically machined passive 3D alignment assembly, based on the principle displayed in Figure 6.1. To the Authors' knowledge, no one has performed 3D passive alignment of optical components with perpendicular U-Grooves to control spacing laterally in all axes. Only one 2.5D U-Groove fibre dowel based alignment platform has been discussed in literature,

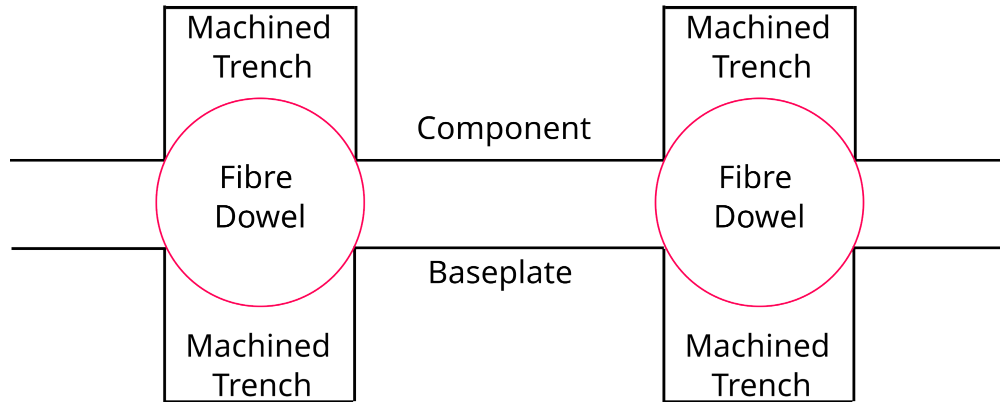

FIGURE 6.1: Diagram displaying the key principle of the passive alignment using fibre dowels in U-Grooves to align components to a base-plate

where Park et al, created a fibre dowel U-Groove alignment method to align a fibre array to a Photonic Lightwave Circuit platform (PLC), with an impressive lateral fibre to PLC alignment accuracy of ≤ 1.2 µm [46], which is a promising indicator of the platform capabilities. To extend this into 3D, a novel method is proposed with machined perpendicular U-Grooves to test whether the alignment and straightness of dicing saws is sufficient for the purpose of component alignment.

This assembly was developed to both validate the tooling and to minimise the fabrication steps, enabling a high throughput of test assemblies. The first consideration was the dowels. For optimum precision, the requirement is for something with a near perfectly round cross-section and nanometre accurate diameter. SMF28 (Single Mode Fibre) produced by Corning is quoted to have a diameter of 125 $\pm$ 0.1 µm over 5 km. Whispering gallery modes have been used to measure the diameter variation of short segments of fibre. Poon et al measured a diameter variation of 9 nm over a 7 mm segment [47], therefore it is not unreasonable to assume there is minimum variation over a length of 30 mm. With an accurate component to act as the dowel in the alignment platform, the next step is to fabricate grooves for the dowels to locate into, and verify the capability of producing such features with the necessary precision.

6.3.1 Fibre V & U-Grooves

V-Grooves are commonly used when fabricating fibre arrays (V-groove arrays), allowing a standard pitch accuracy of ≤ 3 µm, with individual arrays achieving 0.5 µm [48, 49]. U-Grooves have also been used in fibre arrays, obtaining a similar pitch accuracy [50]. The main benefit of using groove based alignment, is that the fibre only has to be initially placed to half of the fibre width accuracy (62.5 µm for standard single mode fibre) before the fibre will self-center in the groove, allowing for less

precise jigs and holders to be made for rapid pick and place robot or manual hand placement.

There are two types of U-grooves, the first is where the fibre sits on top of the corners, and the other where the fibre sits inside the trench completely. The latter is often used for butt-coupling fibres, however has no usage in this work due to the alignment platform requiring both sides of the fibre to be exposed. The top corner method will be used within this work, because it allows stacking of multiple layers and henceforth will be referred to as ”U-groove”. However, despite the improvements of the tolerances, the U-grooves are not often seen in literature. Most fibre-arrays use V-Groove based designs, likely V-grooves relative ease of etching angles in silicon. This ease is because of silicons' crystal axis planes causing non-uniform etch rates with certain etchants. The standard prevalence of MEMS tooling for silicon also allows significant scale cost reductions over a custom one off etching process for a specific material.

The main principle of the V- and U-Groove platforms are displayed in Figure 6.2, with idealised grooves displayed in the top half. The benefit of using these groove types is that U-Grooves platforms are immune to displacement errors caused by surface chipping since the tension of the fibre will enable the fibre to remain straight while passing over chipped regions. The primary benefit of using a U-groove over a V-Groove (at least when physically machined) is that as long as the groove depth is sufficient, the fibre misalignment is decoupled from the blade wear. In general, the blade sidewall doesn't have significant loading, so width wear is minimal, providing a constant width throughout the machining provided that the trench depth is sufficient that the shape does not approach the surface, making parallelism of trenches and straightness the main concern. However, when a V-blade is used, the wear will be spread across all of the V surface, causing misalignment in both directions since the wear is unlikely to be even. This is illustrated in the lower half of Figure 6.2.

6.4 Assembly Design & Discussion

The assembly was designed to test the fabrication tolerances of the dicing machines available, and to see whether physical machining can be used for the purpose of creating a novel passive alignment platform for quantum technology. The testing methodology is to air-couple two fibres over a target gap of 20 µm, with machined U-grooves and fibre dowels. This is to ensure that the heights are consistent, allowing parallel alignment offsets to be calculated utilising the coupling efficiencies between the fibres. The design was based on the principles of a fibre array, where the active fibre is placed within a dummy fibre array that is singulated in half. The array halves

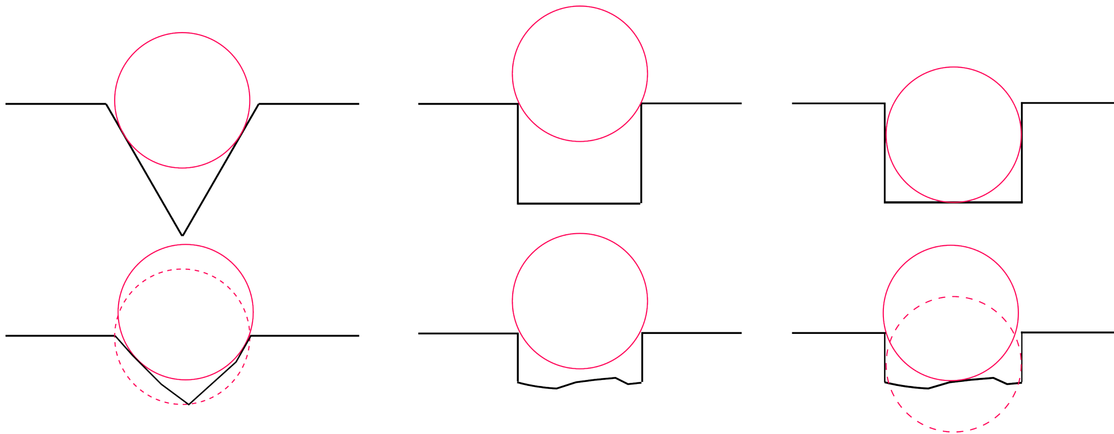

FIGURE 6.2: Schematic displaying the principles of an optical-fibre in a V-Groove and a U-Groove. The top row displays the idealised U- and V-Grooves, with the bottom row displaying fibres sat in worn U- and V-Grooves. The dashed line indicates the initial position of the fibre in the V-groove indicating a displacement, whereas the fibre on top U-Groove fibre remains fixed in place.

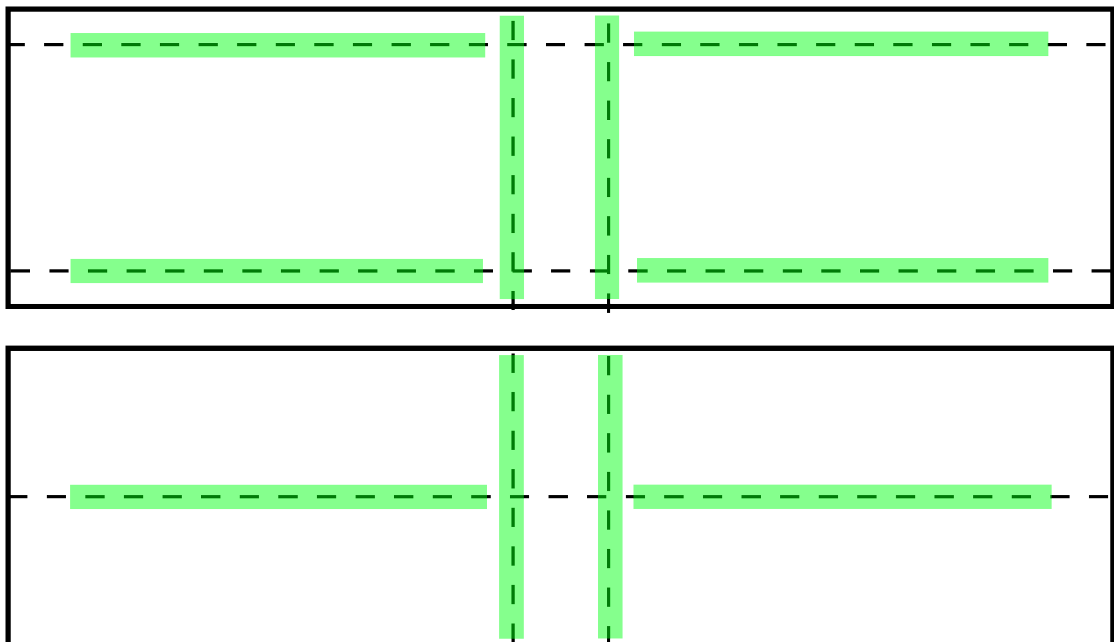

FIGURE 6.3: U-grooves in a ″n″ (top) and ″T″ (bottom) layout, as highlighted in green.

are then mounted on a base plate with fibre dowels and machined, spaced trenches to obtain the target gap as shown in Figure 6.4.

The designs are based around having U-Grooves in ″n″ or ″T″ layouts on the underside of the array and topside of a base-plate. These grooves combined with fibre dowels as the interlocking mechanism will fit together as displayed in Figure 6.3. The T's are arguably kinematic, due to having 6 contact points to restrain the 6 degrees of freedom, however, the lengths of the fibre involved make the contact points extend over a relatively large area. The ″n″s are not kinematic due to having 8 contact points for 6 degrees of freedom, but are semi-elastically averaged, allowing for more stability.

To achieve a 20 μm gap between the optical fibres, the blade kerf has to be known and accounted for in advance. A test cut in the target material is performed with the planned singulation blade, and the kerf is measured with the ZeGage. Figure 6.4a shows the first step of the fabrication of the assembly, starting with a 100 mm by 25 mm silica rectangle (AB).

Silica was utilised due to the materials' high strength, temperature resistance/low expansion and vacuum stability. Atom traps require vacuum and thermal stability. Usually atom systems are baked out to minimise outgassing, then pumped down to low temperatures. Thermal expansion coefficients are to be matched or kept similar to maintain alignment during these extreme temperature swings. Silica is chosen to enable the usage of matching expansion coefficient glass frit solders for bonding. For these platform tests, UV curable resins were used to quickly fabricate test assemblies. This was because of the ease of use and because they are curable through the silica. A low viscosity UV-glue has been chosen due to the limited space, and for the glue to wick along the fibre.

A rectangle was singulated out of a silica wafer as displayed in Figure 6.4a, to construct the base-plate (B) and the bottom array (A) plate. Two lengthwise U-Grooves were machined in a single pass, enabling machining of parallel grooves with the same pitch (distance apart) on both base-plate and bottom array plates. This minimised the chances of errors occurring during the fabrication. Next, the rectangle was rotated 90° and the alignment U-Grooves that control the lateral offset spacing were machined, targeting a gap of 20 μm. The base-plates' (B) pair of grooves are set to 5 mm, spaced in between the middle of the base-plate. The bottom array plate had the counterpart U-grooves with spacing of 5 mm + 20 μm - singulation blade kerf machined into the middle of the other half.

The next step was to groove in the array U-Grooves on the other side of the rectangle, then singulate the rectangle into two (labelled A and B) as indicated in Figure 6.4b. The bottom array plate with the alignment features grooved in was fixed on a vacuum chuck. Active optical fibre, used for testing the coupling post-assembly, and fibre dowels were placed into the groove as required, typically one active fibre and one or more more fibre dowels for controlling constraints. A wire was used to place a very minimal amount of UV resin on the chip then the cap (C) was placed on top with a weight. It was left for a while to settle in place, then UV gun cured to be fixed in place as illustrated in Figure 6.4c.

This fibre array was singulated with the specific blade measured in a previous step between the two offset grooves. This step was illustrated in Figure 6.4. The singulation was carried out with a high-grit blade (#5000 +) at a feed rate of 0.1 $\mathrm{mm\,s^{-1}}$ to obtain optical quality finish on the active optical fibre. The array cap piece was a flat rectangle diced out of a silica wafer. The cap is flat to reduce the complexity

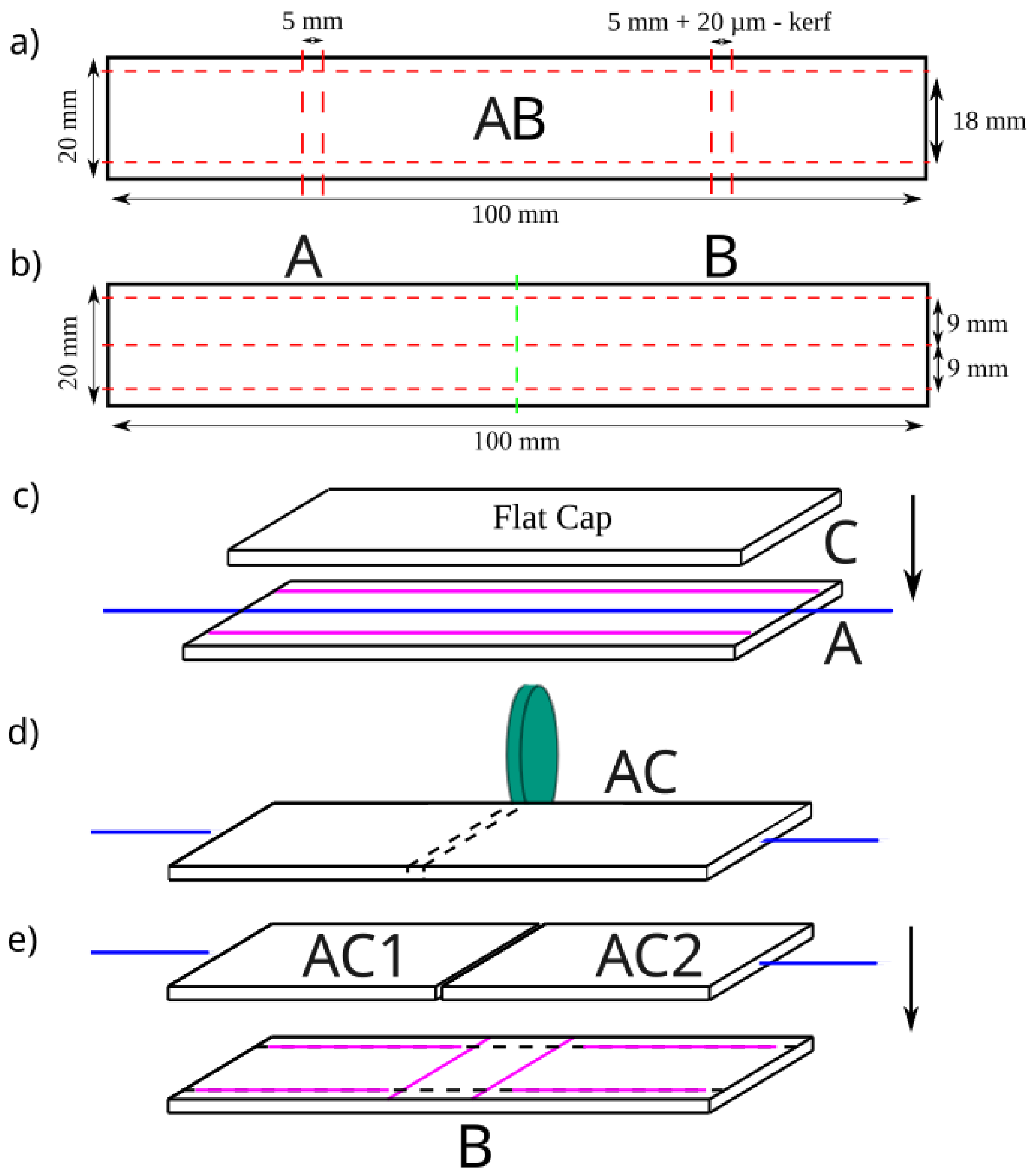

FIGURE 6.4: Fabrication steps of the passive alignment platform. Red dashed lines are machined grooves and the green dashed line is a singulation cut. a) Initial U-grooving step for creating the 3D lateral alignment features b) Fibre array component fabrication for alignment testing c) Fibre array construction d) Singulation of fibre array e) Reconstruction of fibre array to test alignment platform

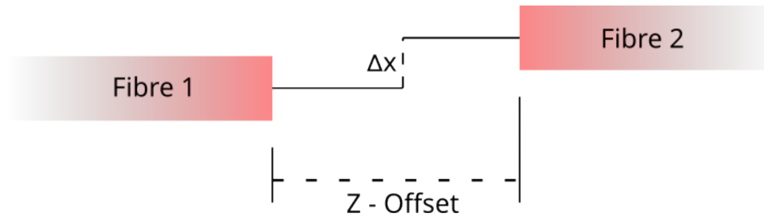

FIGURE 6.5: Diagram displaying the two relevant offsets for the parallel equation in Equation 6.1

.

of the assembly and possible causes of misalignment. There was no requirement to do this step in this order, however it makes the grooving simpler and quicker.

The final step was to assemble the test device, as depicted in Figure 6.4e. Fibre dowels were placed into the grooves as required. The array halves are then placed onto the base-plate with wire deposited UV glue - typically OP-20632 due to the low viscosity. A weight was placed on top and the device cured with a UV LED gun. The complete assembly then had fibre patch ends spliced on the active fibre as required to enable power transmission throughput to be evaluated.

6.5 Assembly Results

The assembly tests were carried out on the Loadpoint MicroAce 3 dicing saw, then switched to the DAD 3430 dicing saw for the purpose of comparison. In the interests of conciseness, only the most performant results are in Table 6.1 and will be discussed here in detail. The lateral offset equation in Equation 6.1 is used to calculate the offsets, as displayed in Figure 6.5, assuming that the fibres are parallel to one another and the Z-offset is measured by the microscope.

$$\Delta x = \sqrt{\frac{\omega_1^2 + \omega_2^2}{2} \ln \frac{\eta \left(\omega_1^2 + \omega_2^2\right)^2}{4\left(\omega_1^2 \omega_2^2\right)}} \tag{6.1}$$

Where;

$$\omega_1 = a\left(0.65 + \frac{1.619}{V^{\frac{3}{2}}} + \frac{2.879}{V^6}\right) \tag{6.2}$$

$$\omega_2 = \omega_1 \sqrt{1 + \left(\frac{Z}{Z_R}\right)^2} \tag{6.3}$$

Where a is the fibre core radius, V is the V-number (which for SMF is $\frac{2\pi n(\mathrm{NA})}{\lambda}$), Z is the gap between the top chips, Z_R is the Rayleigh length and NA is the numerical aperture.

Assembly Label	Wavelength (nm)	Fabricated On	Z Offset (µm)	Parallel Offset (µm)
1	515	MicroAce3	475	14.4
2L Graticule	515	MicroAce3	20.7	25.5
2R Graticule	515	MicroAce3	20.7	26.3
3R	1550	DAD 3430	60	180
3L	1550	DAD 3430	60	180

TABLE 6.1: Table displaying notable alignment test results of the assembly.

The early assemblies were based on T-shaped designs rather than n-shaped designs. These assemblies performed very poorly, with most failing to transmit any optical power across the 20 µm gap. The assemblies suffered from constant misalignment during fabrication due to the layers tilting, since the fibre weighed more than the array sections. As a result, the decision was made to fabricate Assembly 1 using the n-shaped design. This approach was a partial success, achieving a parallel offset of 14.4 µm. However, the Z-offset target of 500 µm was not met, being 25 µm off. The 500 µm Z-offset target was to minimise concerns about blade sidewall wear during singulation, which caused a V-shaped cut, resulting in the two halves touching in the middle and leading to significant misalignment. The unusual sidewall wear was due to hardness of silica compared to the relatively soft resin blades. the To mitigate this issue, new harder wearing nickel blades with #5000 grit were purchased and used with later work.

The MicroAce3 was calibrated according to the precision graticule (discussed in Chapter 3) and Assembly 2 was fabricated. L and R represents direction of the light propagation through the array. This instantly performed well, with a 25 µm parallel offset and the new dicing blades allowed singulation of the the Array with high perpendicularity, as indicated by the 20.7 µm Z-Offset. This was a promising test result, and the choice was made to test the platform on the DAD 3430 dicing saw, which is specified to a better straightness, allows more blade choices, and is a stiffer machine, allowing for theoretically more consistent machining.

After some test assemblies, Assembly 3 was fabricated. The alignment on this was worse than the best MicroAce3 results, with a parallel offset of 180 µm, representing an increase of over 7x. This was a surprising result, and despite multiple further assemblies, the performance did not improve. The precision graticule did not fit under the DAD 3430 camera, so an alignment wafer was made on the MicroAce3 as reference, but this did not improve the resulting platform. The reasoning for this was theorised to be a combination of the rotation stage being imprecise and the typical process flow for a dicing machine is to be aligned to existing features, which do not exist here. The next experiment shall address this.

6.6 Assembly V vs U

The aim of this experiment was to compare V-Groove and U-Groove alignment tolerances and to verify the DAD 3430s' rotation stepper accuracy. The designs were nearly exactly the same as the previous section, with three key differences, the first was that an array of fibres was coupled, instead of one. This was to test the uniformity of the machined grooves over multiple cuts with two different blades, as well as to further test the repeatability of the introduced methodology. A silicon wafer was used with a UV transparent lithium niobate cap. The silicon was far softer to machine than the silica, and so provided the best case scenario for machining with a current state-of-the-art machine. The lithium niobate was chosen to allow for the glue to be cured through the cap, enabling sufficient fixing of the assembly components for the singulation step and further assembly stages. The lithium niobate and silicon combination was also softer than silica allowing for smoother trenches and less form deviations arising from blade wear.

A 60 degree custom V-blade was obtained from DISCO for this research. A standard, flat dressed square blade was used for the U-grooves. The kerf was specified for both blades to be 115 µm for the purpose of fibre setting, and the depth of cut was calculated to be 38 µm minimum for the U-groove fab to prevent the bottom of the fibre touching the base and causing misalignment. The depth of cut should ideally be set to minimum, since cutting into a wafer has been seen to cause warpage due to stress relief, so to retain as much stiffness as possible the target depth of cut was set to 50 µm on both blades.

Two devices were fabricated, a U-groove assembly and a V-Groove assembly. 10 fibre arrays were aimed for, however, due to difficulties of fixing all the fibres in place, this was reduced to a 3 fibre array. This could be addressed in the future with more engineering. The devices were fabricated and then the rest of the steps were the same as discussed in section 6.4. Before construction of the array, the layers were profiled by the confocal scanner post-dicing to provide information on the straightness and rotational limits of the DAD 3430. After construction, the throughput's were measured, with the results discussed in the next section.

6.6.1 Assembly Results

First, the transmission results are in Table 6.2. The transmissions clearly show that two array halves have twisted significantly. The Z-Offset measurements confirm this, however, this is hard to measure due to the focusing the microscope through the array. Despite this, the parallel offset equations were still used just to compare with the prior work. The V-Grooves were more consistent with their performance, with a gentler

Chip	Wavelength (nm)	Power In (mW)	Power Out (mW)	Z-Offset Approximation (µm)	Parallel Offset (µm)
U	1550	18	2.76	59	131.3
		18	0.21	43	202.3
		18	0	28	NA
V	1550	18	0.61	26	176.4
		18	0.94	20	164.7
		18	1.86	18	144.4

TABLE 6.2: Table displaying the results of the V-Groove vs U-Groove transmission tests. NA represents sufficient mode to mode offset that no coupling was possible.

twist; however, this was still poor, with parallel offsets varying from 131 µm to undefined. This is no significant improvement over the previous work, however, the confocal scans were still analysed.

The parallelism of the V-Groove and U-Groove array components is displayed in Table 6.3. The RMS deviation of the middle of the cut from nominal position and the end to end fitted slope deviation of the cut from the first cut are displayed. The V-Groove has slightly worse RMS deviation than the U-grooves, however, is still sufficient for the alignment, being that on a local scale, it is still going to be better than this. The end to end deviations are also fantastic, being 0.111 µm and 0.161 µm on average. The end to end parallelism is extremely consistent, with minimal deviation from the mean. This rules out the array being the cause of the assembly misalignment.

The ″n″ passive alignment features were analysed for rotation errors. The misalignment error of the angles displayed in Table 6.4, and the resulting offset at the end of the chip have been calculated and tabulated in Table 6.4. The base-plate features have very good rotation errors, being 0.01° and 0.03° resulting in minimal deviation; however, the array undersides (marked as Top) have significant rotation misalignment of 0.37° and -0.32°. This results in having fibre offsets of 31 µm and 23 µm respectively at the end of the lengthwise grooves. This is certainly the reason why the DAD machined assemblies did not fit together, as the total offset is double those values, causing complete misalignment.

The cause as to why the misalignment between the Base and Top pieces is unclear, since the grooves are machined at the same time, pre-singulation, so the expectation was that they remain the same angle. Unfortunately, this is clearly not the case. Due to time constraints, this was not investigated, however, it is theorised that this is due to the forces on the chuck, causing varying amounts of backlash of the rotation stage. The results of Chapter chapter 4 also suggest using a shallow square blade at the minimum depth to seat the fibre, however, this may also cause issues with blade engagement.

V-Groove Assembly		
Trench	RMS Deviation (µm)	Slope Variation (µm)
1	1.114	0.000
2	1.207	0.032
3	1.181	-0.016
4	1.089	0.381
5	1.068	0.164
6	0.972	-0.046
7	1.028	-0.100
8	0.936	0.004
9	0.920	-0.053
10	0.981	-0.315
Absolute Mean	1.049	0.111
StdErr	0.031	0.057

U-Groove Assembly		
Trench	RMS Deviation (µm)	Slope Variation (µm)
1	0.629	0.000
2	0.691	-0.029
3	0.690	0.041
4	0.715	0.163
5	0.675	-0.048
6	0.734	0.526
7	0.703	0.309
8	0.511	0.065
9	0.768	0.273
10	0.684	-0.159
Absolute Mean	0.680	0.161
StdErr	0.022	0.065

TABLE 6.3: Table of the RMS deviation from the nominal position and end to end slope variation relative to the first trench.

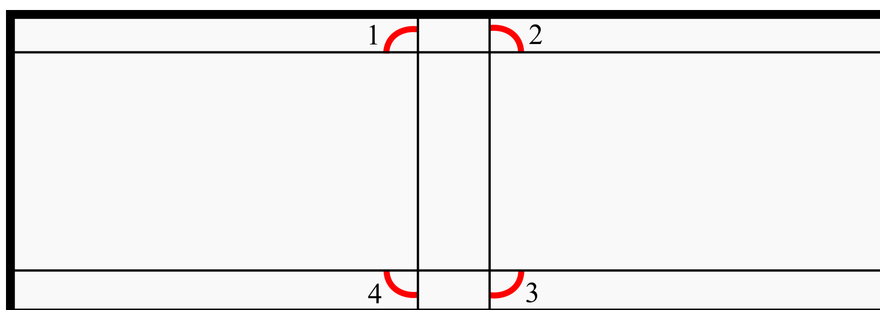

FIGURE 6.6: Diagram displaying the angles discussed in Table 6.4.

V Base	Misalignment (°)	Offset (µm)	Error (µm)
1	0.0330	0.248	0.050
2	0.0327	0.244	0.079
3	0.0326	0.243	0.147
4	0.0324	0.239	0.277
V Top	Misalignment (°)	Offset (µm)	Error (µm)
1	0.370	31.1	0.292
2	0.369	31.1	0.213
3	0.370	31.1	0.019
4	0.370	31.1	0.486
U Base	Misalignment (°)	Offset (µm)	Error (µm)
1	0.0135	0.0418	0.402
2	0.0135	0.0417	0.386
3	0.0134	0.0411	0.044
4	0.0134	0.0411	0.027
U Top	Misalignment (°)	Offset (µm)	Error (µm)
1	-0.318	23.0	0.0231
2	-0.318	23.0	0.0614
3	-0.318	23.0	0.0240
4	-0.318	23.0	0.0602

TABLE 6.4: Table of alignment errors in the assembly measured by the confocal probe, 1-4 represent the positions drawn in Figure 6.6.

6.7 Swansea SWIFT Trap

As part of a collaboration with Dr James Bateman at the University of Swansea, the standing wave optical trap was developed using the principles discussed previously. The SWIFT trap is a standing wave optical trap, consisting of 3 pairs of fibre, in a hexagonal platform. The fabrication of the trap consisted of milling and dicing. The design of the SWIFT trap allows concurrent validation of the assumptions about the machined U and V-grooves, being that the U-Grooves have better machining tolerances than the V-Grooves.

6.7.1 Fabrication

To compare the V with the U, two hexagons were fabricated in three main steps, illustrated in Figure 6.7. Two hexagons were singulated out of a silicon wafer. 3 U-Grooves and V-Grooves are machined in each wafer respectively, perpendicular and central to each of the flat sides. The U-grooves were machined in a single pass whereas the V-Grooves were machined with two passes, the first with a narrow flat blade, the second with a V-Groove. This was done to minimise tip wear on the custom

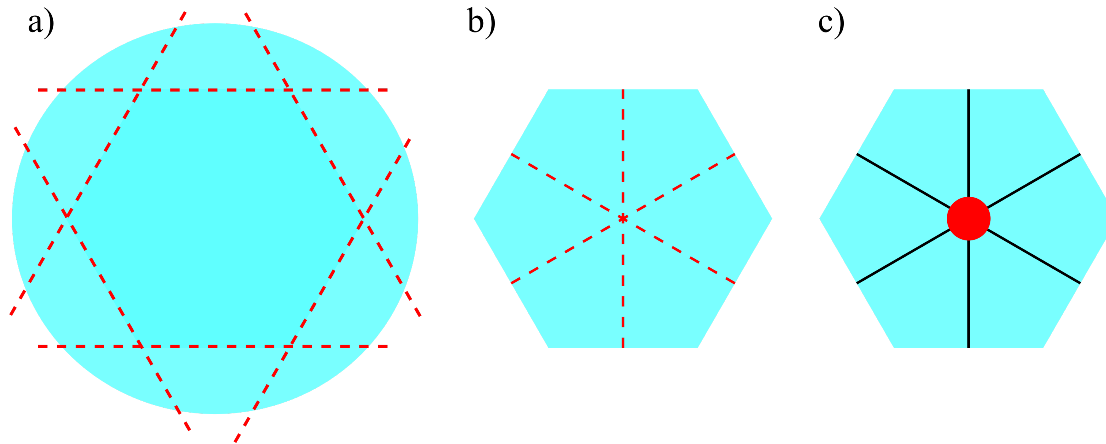

FIGURE 6.7: Schematic of the Swansea SWIFT trap fabrication process. a) A hexagon is singulated out of a silicon wafer b) U-Grooves or V-Grooves are machined into the surface c) A hole is milled in the middle for trapping purposes.

blades for further work. The rotation was carried out programmatically by DAD 3430. Finally a 3 mm hole was milled in the middle of the hexagon, where the grooves cross by Dr Paul Gow. The U-groove unit was shipped off to Swansea for further validation and results are promising.

6.7.2 Comparison of V- & U- Grooves

The experimental setup is illustrated in Figure 6.8, and an image is shown in Figure 6.9. A 10 mW 1550 nm Santec TS110 source is fed through a fibre 3dB (50:50) splitter to create a reference and signal fibre. This is to take into account the source power variation. The reference is coupled to a power meter. A length of SMF28 is used as the signal fibre. Patch ends are spliced onto the ends of the SMF28 length, of which the latter half is partially wrapped round a 12.7 mm diameter post to minimise the cladding modes. Power transmission through both the signal and reference fibres are recorded over a 10 second average. This resulted in a throughput ratio of 1.07364, which was used later to compensate for the power variation of the source.

The active fibre was cleaved, and the ends are placed into Fujikira clips. These were magnetically positioned into a translation stage, that is in turn mounted on a base plate at the required angles and approximately the right spacing. The fibre flexibility over such a distance allowed a weight to be placed onto the fibres to passively locate them within the diced grooves. This setup provides precise control of the lateral position of the fibres in the grooves, as displayed in Figure 6.9. A drop of refractive index oil (n = 1.46) is placed to eliminate air-gaps between the optical fibres. The fibres are butt-coupled against each other and the 10 second average reference and trap powers were recorded. This was repeated 3 times per numbered pair and was performed for each of the pair combinations.

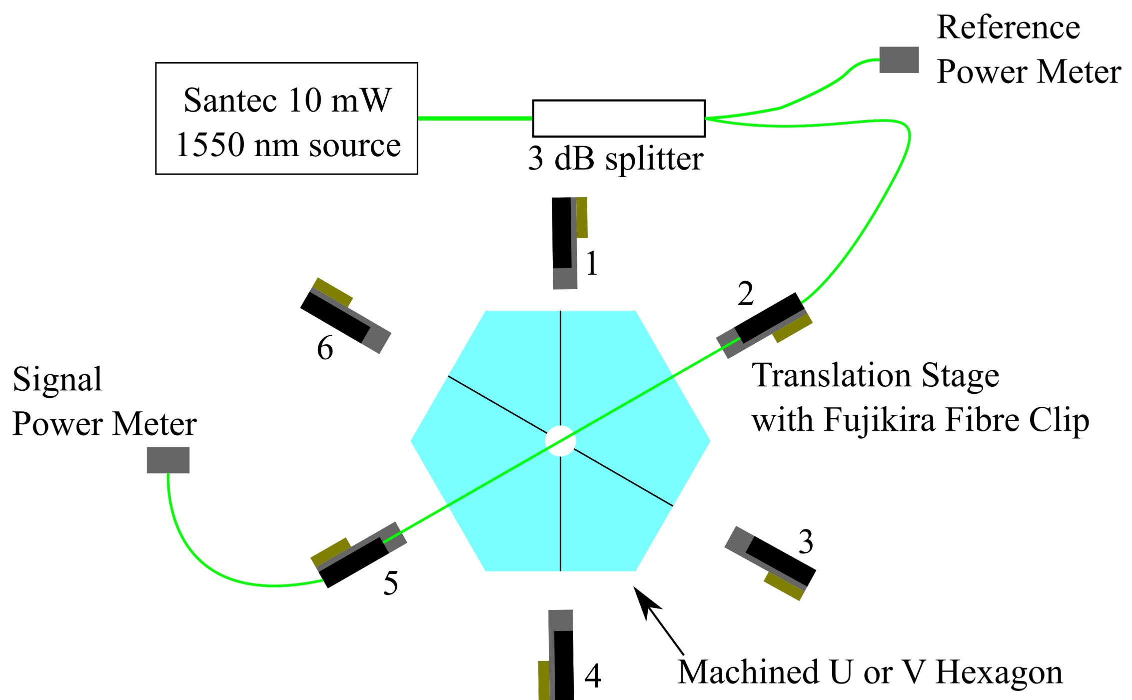

FIGURE 6.8: Schematic of the Swansea trap U-Groove vs V-Groove comparison setup. The numbers indicate the entry/exit pair of the butt-coupled fibre.

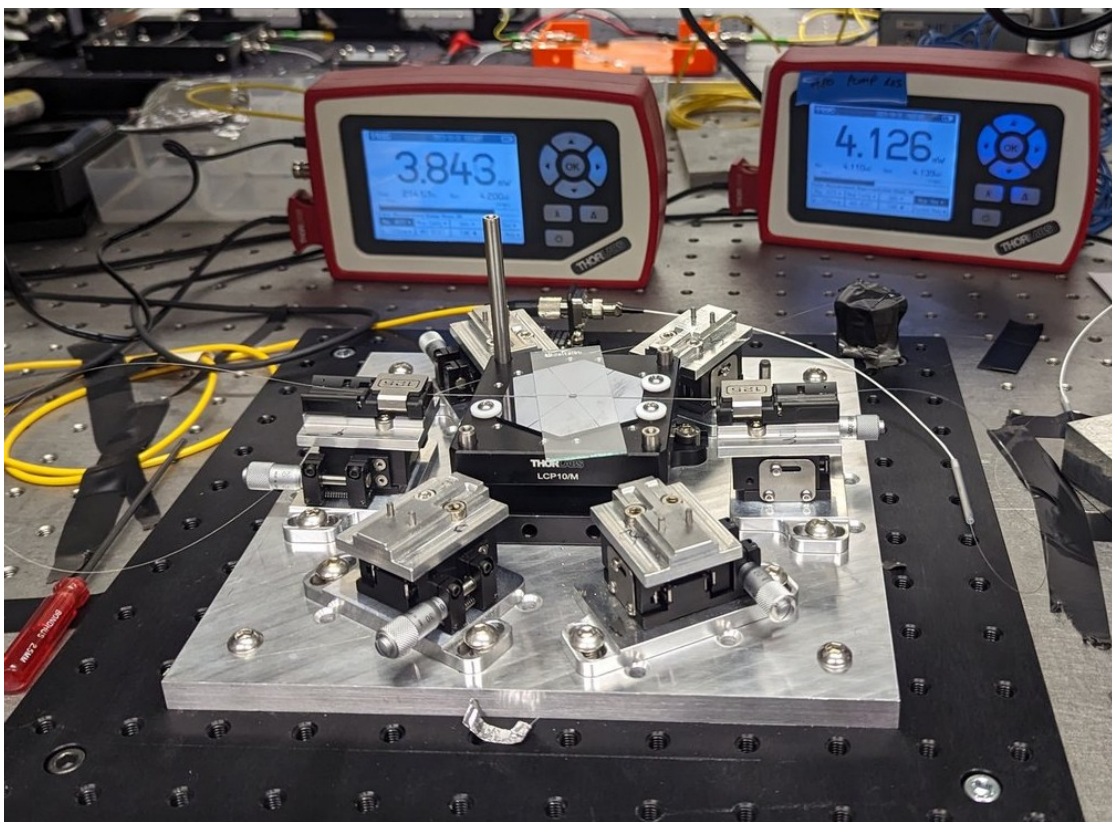

FIGURE 6.9: Photo of the Swansea swift trap alignment rig. The left and right power meters are the reference and signal fibres respectively.

The signal to reference ratio recorded earlier was used to correct for the power variation of the source, and then the transmission efficiency calculated. Considering that the fibres are butt-coupled, the parallel offset equation is simplified to Equation 6.4. Other assumptions made are that the cleave is perfect, no fibre angular misalignment and that the fibre is perfectly concentric.

$$\Delta x = \sqrt{\omega^2 \ln \eta} \tag{6.4}$$

Where;

$$\omega = a \left(0.65 + \frac{1.619}{V^{\frac{3}{2}}} + \frac{2.879}{V^6} \right) \tag{6.5}$$

Where a is the fibre core radius, V is the V-number (which for SMF is $\frac{2\pi n(\mathrm{NA})}{\lambda}$).

The experimental results are in Table 6.5. There was a noticeable difference between the V and U-Grooves. The U-Grooves have a third better parallel offset with their correspondingly improved transmission throughput. This result proves that physically machined U-Grooves are more performant and have a better defect tolerance than the V-Grooves. An improvement of transmission of 2% has been found by simply changing the blade shape from a V to a standard, cheaper square blade and changing the depth of cut. This data indicates 300 nm better alignment, almost 30%, in the alignment of fibre to fibre accuracy, which represents a significant improvement. This highlights the fibre misalignment error inherent due to wear of the blade during machining, whereas the U-Groove fibre misalignment is uncoupled from the blade wear rates due to the negligible sidewall wear.

Fibre Pair	U-Groove				V-Groove			
	Coupling Efficiency	StdErr	Parallel Offset (µm)	StdErr	Coupling Efficiency	StdErr	Parallel Offset (µm)	StdErr
1->4	0.990	0.001	0.524	0.009	0.972	0.006	0.868	0.103
2->5	0.988	0.001	0.566	0.034	0.974	0.003	0.853	0.047
3->6	0.984	0.003	0.667	0.072	0.958	0.007	1.079	0.088
4->1	0.985	0.003	0.649	0.018	0.969	0.005	0.931	0.072
5->2	0.987	0.001	0.594	0.042	0.972	0.004	0.883	0.064
6->3	0.980	0.002	0.741	0.059	0.962	0.006	1.026	0.090
Mean	0.987	0.002	0.624	0.039	0.968	0.006	0.940	0.077

TABLE 6.5: Table displaying the butt-coupled U vs V groove fibre transmission results. Due to the assumptions made, the parallel offsets are the upper bound, and the true offset may be better.

6.7.3 Conclusions

In this chapter, a novel assembly enabling 3D alignment of multiple components on a base plate has been proposed utilising optical fibre and deterministic machining. A fibre array split in half, then reassembled onto a base-plate with a target gap of 20 was used as the test component, with a target fibre to fibre accuracy of $\leq$ 0.5 μm. Multiple test assemblies were constructed, with the most performant achieving an offset of about 14 μm. This was not optically performant, and was fabricated on the MicroAce3, a less precise and less stable machine than the DAD 3430, hence was a surprising result.

Topological scans were performed utilising the confocal scanner on the most recent DAD 3430 diced alignment, and have highlighted an issue with variation on angle due to different lateral cut positioning. Locally close and parallel cuts are parallel with well below sub micron variation of the midpoint, however, when it comes to two batches of grooves machined with a substantial (10s of mm) offset from one another, there is an angle misalignment of up to 0.37°. This results in a groove misplacement of 30 μm on either of the lengthwise grooves, causing a twisting of plates to occur. This twisting action and the interplay of the components with low friction resin glues would explain the minimal lack of success. It is theorised that this is backlash caused by the DAD 3430 rotation stepper and stresses of the blade acting on the chuck. In order to resolve these issues for photonics, the next generation dicing machines should have more accurate and stiffer rotation mechanism. Also to reduce machining errors due to wafer warp, some sort of on-machine topographical scanning of both the wafer chuck and the workpiece is required to self-correct the machining positions with fine control over the height of the blade. All of these issues are theoretically solved by the UPROAR project and the recommendation is that these assembly tests are performed on that new machine.

U-grooves and V-Grooves have been compared, with a significant improvement in the machined consistency observed in the U-grooves, arising from the decoupling of the U-Groove shape from the blade wear assuming a sufficient depth, whereas a V-Groove is not decoupled and any wear would change the alignment. A 30% improvement has been obtained in unsupported fibre to fibre alignment over an unsupported gap of 3 mm, highlighting the deterministic machining capability of U-Grooves, resulting in a 2% more coupling efficiency.

References

1. Horvath GZK, Thompson R, and Knight P. Fundamental physics with trapped ions. Contemporary Physics 1997; 38:25–48

2. Wunderlich C and Balzer C. Quantum measurements and new concepts for experiments with trapped ions. *Advances in Atomic, Molecular, and Optical Physics*. Vol. 49. Elsevier, 2003 :293–372
3. Devani D, Maddox S, Renshaw R, Cox N, Sweeney H, Cross T, Holynski M, Nolli R, Winch J, Bongs K, et al. Gravity sensing: cold atom trap onboard a 6U CubeSat. CEAS Space Journal 2020; 12:539–49
4. Li D, He W, Shi S, Wu B, Xiao Y, Lin Q, and Li L. Review of atom chips for absolute gravity sensors. Sensors 2023; 23:5089
5. Dimopoulos S, Graham PW, Hogan JM, Kasevich MA, and Rajendran S. Atomic gravitational wave interferometric sensor. Physical Review D—Particles, Fields, Gravitation, and Cosmology 2008; 78:122002
6. Robinson JM, Miklos M, Tso YM, Kennedy CJ, Bothwell T, Kedar D, Thompson JK, and Ye J. Direct comparison of two spin-squeezed optical clock ensembles at the 10- 17 level. Nature Physics 2024; 20:208–13
7. Ren W, Li T, Qu Q, Wang B, Li L, Lü D, Chen W, and Liu L. Development of a space cold atom clock. National Science Review 2020; 7:1828–36
8. Burt E, Prestage J, Tjoelker R, Enzer D, Kuang D, Murphy D, Robison D, Seubert J, Wang R, and Ely T. Demonstration of a trapped-ion atomic clock in space. Nature 2021; 595:43–7
9. Monroe C and Kim J. Scaling the ion trap quantum processor. Science 2013; 339:1164–9
10. Brown KR, Chiaverini J, Sage JM, and Häffner H. Materials challenges for trapped-ion quantum computers. Nature Reviews Materials 2021; 6:892–905
11. Daley AJ. Quantum computing and quantum simulation with group-II atoms. Quantum Information Processing 2011; 10:865–84
12. Bruzewicz CD, Chiaverini J, McConnell R, and Sage JM. Trapped-ion quantum computing: Progress and challenges. Applied Physics Reviews 2019; 6
13. Graham T, Song Y, Scott J, Poole C, Phuttitarn L, Jooya K, Eichler P, Jiang X, Marra A, Grinkemeyer B, et al. Multi-qubit entanglement and algorithms on a neutral-atom quantum computer. Nature 2022; 604:457–62
14. Harsono A. Dipole trapping and manipulation of ultra-cold atoms. PhD thesis. University of Oxford, 2006
15. Beterov I, Yakshina E, Tretyakov D, Entin V, Singh U, Kudlaev YV, Mityanin KY, Panov K, Alyanova N, Andreeva C, et al. Trapping, detection and manipulation of single Rb atoms in an optical dipole trap using a long-focus objective lens. *Journal of Physics: Conference Series*. Vol. 1859. 1. IOP Publishing. 2021 :012049

16. Zhang S, Chen J, Liu C, Zhou S, Loy M, Wong GKL, and Du S. A dark-line two-dimensional magneto-optical trap of 85Rb atoms with high optical depth. Review of Scientific Instruments 2012; 83
17. Tey MK, Chen Z, Aljunid SA, Chng B, Huber F, Maslennikov G, and Kurtsiefer C. Strong interaction between light and a single trapped atom without the need for a cavity. Nature Physics 2008; 4:924–7
18. Quinto-Su P, Tscherneck M, Holmes M, and Bigelow N. On-chip optical detection of laser cooled atoms. Optics Express 2004; 12:5098–103
19. Ragg S, Decaroli C, Lutz T, and Home JP. Segmented ion-trap fabrication using high precision stacked wafers. Review of Scientific Instruments 2019; 90
20. Blakestad R, Ospelkaus C, VanDevender A, Amini J, Britton J, Leibfried D, and Wineland DJ. High-fidelity transport of trapped-ion qubits through an X-junction trap array. Physical Review Letters 2009; 102:153002
21. Wright K, Amini JM, Faircloth DL, Volin C, Doret SC, Hayden H, Pai C, Landgren DW, Denison D, Killian T, et al. Reliable transport through a microfabricated X-junction surface-electrode ion trap. New Journal of Physics 2013; 15:033004
22. Blakestad RB. Transport of trapped-ion qubits within a scalable quantum processor. PhD thesis. 2010
23. Kienzler D, Lo HY, Keitch B, De Clercq L, Leupold F, Lindenfelser F, Marinelli M, Negnevitsky V, and Home J. Quantum harmonic oscillator state synthesis by reservoir engineering. Science 2015; 347:53–6
24. Day ML, Choonee K, Chaboyer Z, Gross S, Withford MJ, Sinclair AG, and Marshall GD. A micro-optical module for multi-wavelength addressing of trapped ions. Quantum Science and Technology 2021 Feb; 6:024007. DOI: `10.1088/2058-9565/abdf38`
25. Nazir SI. Femtosecond laser-based optomechanical processes for permanent and high-precision fine alignment of optical systems. en. PhD thesis. Lausanne: EPFL, 2021. DOI: `10.5075/epfl-thesis-8694`
26. Wu M, Lin LY, Lee SS, and Pister K. Micromachined free-space integrated micro-optics. Sensors and Actuators A: Physical 1995; 50:127–34. DOI: `https://doi.org/10.1016/0924-4247(96)80096-3`
27. Mohr J, Goettert J, and Mueller A. Micro-optical devices based on free-space optics with LIGA micro-optical benches: examples and perspectives. *Micro-Optical Technologies for Measurement, Sensors, and Microsystems*. Vol. 2783. SPIE. 1996 :48–54
28. Lo JC, Lee SR, Wu J, Kim JK, and Yuen MM. Chip-on-chip 3D optical interconnect with passive alignment. *2004 Proceedings. 54th Electronic Components and Technology Conference (IEEE Cat. No. 04CH37546)*. Vol. 2. IEEE. 2004 :2015–9

29. Karppinen M, Alajoki T, Tanskanen A, Kataja K, Makinen JT, Kautio K, Karioja P, Immonen M, and Kivilahti J. Parallel optical interconnect between ceramic BGA packages on FR4 board using embedded waveguides and passive optical alignments. *56th Electronic Components and Technology Conference 2006*. IEEE. 2006 :7–pp

30. Hsiao HL, Lan HC, Chang CC, Lee CY, Chen SP, Hsu CH, Chang SF, Lin YS, Kuo FM, Shi JW, et al. Compact and passive-alignment 4-channel$\times$ 2.5-Gbps optical interconnect modules based on silicon optical benches with 45 micro-reflectors. Optics Express 2009; 17:24250–60

31. Hwang SH, Cho MH, Kang SK, Park HH, Cho HS, Kim SH, Shin KU, and Ha SW. Passively assembled optical interconnection system based on an optical printed-circuit board. IEEE photonics technology letters 2006; 18:652–4

32. Wang S, Chi S, and Cheng W. A simple passive-alignment packaging technique for laser diode modules. Materials Chemistry and Physics 1998; 56:189–92

33. Hunziker W, Vogt W, Melchior H, Buchmann P, and Vettiger P. Passive self-aligned low-cost packaging of semiconductor laser arrays on Si motherboard. IEEE Photonics Technology Letters 1995; 7:1324–6. DOI: 10.1109/68.473486

34. Papakonstantinou I, Selviah D, Pitwon R, and Milward D. Low-Cost, Precision, Self-Alignment Technique for Coupling Laser and Photodiode Arrays to Polymer Waveguide Arrays on Multilayer PCBs. Advanced Packaging, IEEE Transactions on 2008 Sep; 31:502–11. DOI: 10.1109/TADVP.2008.924243

35. Pittroff W, Barnikow J, Klein A, Kurpas P, Merkel U, Vogel K, Wurfl J, and Kuhmann J. Flip chip mounting of laser diodes with Au/Sn solder bumps: bumping, self-alignment and laser behavior. *1997 Proceedings 47th Electronic Components and Technology Conference*. 1997 :1235–41. DOI: 10.1109/ECTC.1997.606333

36. Soper N. Simulation, fabrication and assembly techniques for passive alignment of silicon photonic integrated circuits. PhD thesis. University of Southampton, 2020

37. Gurp JFC van, Tichem M, Staufer U, and Zhao J. Passive Photonic Alignment With Submicrometer Repeatability and Accuracy. IEEE Transactions on Components, Packaging and Manufacturing Technology 2013; 3:1971–9. DOI: 10.1109/TCPMT.2013.2272419

38. Krishnamoorthy AV, Cunningham JE, Zheng X, Shubin I, Simons J, Feng D, Liang H, Kung CC, and Asghari M. Optical Proximity Communication With Passively Aligned Silicon Photonic Chips. IEEE Journal of Quantum Electronics 2009; 45:409–14. DOI: 10.1109/JQE.2009.2013104

39. Gurung S. Passive alignment of micro-fluidic chips using the principle of elastic averaging. PhD thesis. Louisiana State University, Agricultural, and Mechanical College, 2007

40. Slocum A and Weber A. Precision passive mechanical alignment of wafers. en. Journal of Microelectromechanical Systems 2003 Dec; 12:826–34. DOI: 10.1109/JMEMS.2003.820289

41. Willoughby PPJ. Elastically averaged precision alignment. PhD thesis. Massachusetts Institute of Technology, 2005

42. Weber AC. Precision passive alignment of wafers. PhD thesis. Massachusetts Institute of Technology, 2002

43. Fukushima T, Hashiguchi H, Bea J, Murugesan M, Lee KW, Tanaka T, and Koyanagi M. 3D integration technologies using self-assembly and electrostatic temporary multichip bonding. *2013 IEEE 63rd Electronic Components and Technology Conference*. IEEE. 2013 :58–63

44. Cundill RT. High-precision silicon nitride balls for bearings. *Commercial Applications of Precision Manufacturing at the Sub-Micron Level*. Commercial Applications of Precision Manufacturing at the Sub-Micron Level. Vol. 1573. SPIE, 1992 Apr 1:75–86. DOI: 10.1117/12.57746

45. Ohki A, Usui M, Sato N, Matsuura N, Katsura K, and Ando Y. Fabrication of a parallel inter-board optical interconnection module using transferred multichip bonding. *2nd 1998 IEMT/IMC Symposium (IEEE Cat. No.98EX225)*. 1998 :123–6. DOI: 10.1109/IEMTIM.1998.704537

46. Park S, Lee JM, and Ko SC. Fabrication method for passive alignment in polymer PLCs with U-grooves. IEEE Photonics Technology Letters 2005; 17:1444–6. DOI: 10.1109/LPT.2005.848287

47. Poon AW, Chang RK, and Chowdhury DQ. Measurement of fiber-cladding diameter uniformity by use of whispering-gallery modes: nanometer resolution in diameter variations along millimeter to centimeter lengths. Optics Letters. 2001 Dec 1; 26. Publisher: Optical Society of America:1867–9. DOI: 10.1364/OL.26.001867

48. Zantvoort J van, Plukker S, Dekkers E, Khoe G, Koonen A, and Waardt H de. Laser supported fibre array alignment with individual fibre fine positioning. *Proceedings Electronic Components and Technology, 2005. ECTC '05.* 2005 :266–271 Vol. 1. DOI: 10.1109/ECTC.2005.1441277

49. Luetzelschwab M, Weiland D, and Desmulliez M. Submicron alignment of a two-dimensional array of multiple single-mode fibers. IEEE Photonics Technology Letters 2005; 17:2634–6. DOI: 10.1109/LPT.2005.859531

50. Williams G, Sachenik P, and Plawsky J. Photochemically processed glass-ceramic optical interconnects. *Proceedings., 39th Electronic Components Conference*. 1989 :359–61. DOI: 10.1109/ECC.1989.77772

Chapter 7

Conclusion & Outlook

This conclusion chapter will summarise the experimental chapter conclusions and then detail any future work recommendations.

In Chapter 3, a bespoke topographical tool was designed and developed around an Aerotech ABL9000 translation stage and a confocal chromatic probe. The system was validated using a precision graticule. The systems' purpose was to measure the straightness of machined features, a key parameter that has not been discussed in the literature previously within the context of ridge waveguide fabrication. As the system also provides highly accurate topographical maps of features, this tool has been utilised extensively in later chapters.

Chapter 4 discussed the long-term evolution of physical machining in lithium niobate, comparing two depths of cut (50 and 100 µm) and two blade shapes (round and square) as starting conditions. All of the conditions, except for the 50 µm deep square starting condition, ultimately converged towards the same depth, with the 50 µm deep square wearing linearly, highlighting a stable condition. The square blades proved to be the most stable, producing a more consistent form throughout the cutting distance, making them more suitable for ridge waveguide fabrication. Notably, the initial blade conditions had long-term effects on form, surface roughness, and chipping, despite the blades trending towards similar shapes within the first metre of cutting. This chapter also tested the hypothesis that the minimum blade wear rate corresponds to minimum surface roughness. This was found to be false; however, clear regime changes in lithium niobate and silicon were discovered, with low surface roughness overlapping regions of low blade wear rates. A minimum feed rate of 1 $\mathrm{mm\,s^{-1}}$ was determined for silicon with the specific RBT-6084 blade model, however, silicon exhibits anisotropic hardness due to crystal plane orientations. Further investigation is required to determine whether this anisotropic hardness has an effect on the machining parameters. Further work is also required to understand the underlying causes of these regime changes and to achieve deterministic machining.

Factors to study include the effects of different blade binders and a wider range of blade parameters in various materials, as different wear and surface roughness correlations are highly likely.

Chapter 5 directly compared ridge waveguides machined with 100 and 300 µm kerf blades, targeting the improvement of SHG performance in 1064 to 532 nm non-linear conversion. A notable average conversion improvement of 226% for the 300 µm over the 100 µm kerf machined ridges was observed. The investigation highlighted the significantly improved width uniformity as the primary cause of the improvement in optical performance, due to the superior stability of the wider blades. No significant changes in surface roughness and top-side chipping were found. Cut straightness measurements identified heavy curvature of up to 1.2 µm. One-off blade curvature has been eliminated by switching blades and performing multiple cuts. Instead, it is hypothesised to be due to bed curvature, bed mounting, or torque caused by the dicing blade. Further investigations should examine wafer curvature, bed flatness, blade curvature, and stage-to-spindle squareness in more detail for better machining of grooves and more uniform ridge waveguides, enabling significant improvements in optical conversion efficiencies.

Chapter 6 proposed and explored a novel 3D assembly enabling 3D alignment of multiple components, utilising deterministic machining of U-Grooves and optical fibres as a dowel component. The most successful assembly achieved a lateral offset of ≤ 14 µm, significantly beyond the ≤ 0.5 µm target. This was investigated using the confocal probe scanner discussed in Chapter 3, which highlighted a rotation error between two pairs of parallel cuts of up to 0.37°, a surprisingly significant value. This is sufficient to explain the poor performance of the assemblies. However, while it is hypothesised to be caused by inconsistent backlash on the rotation stepper of the dicing machine, this has yet to be confirmed.

Chapter 6 also compared U-Grooves and V-Grooves, with a notable improvement in the machining consistency of the U-Grooves, arising from the decoupling of the U-Groove shape from blade wear, assuming sufficient depth. A 30% improvement in unsupported fibre-to-fibre alignment over an unsupported gap of 3 mm was discovered, highlighting the deterministic machining capability of U-Grooves, resulting in a 2% increase in coupling efficiency.

To summarise the future work recommendations, to resolve these issues and achieve deterministic machining of brittle materials, the next generation of dicing machines should feature a more accurate and stiffer rotation mechanism, lower feed rate capabilities, and on-machine metrology. To reduce machining errors due to wafer warp and bed errors, some form of on-machine topographical scanning of both the wafer chuck and the workpiece is required, allowing for automatic correction of the

machining positions with fine control over the height of the blade. The research project UPROAR (Ultra precision machining of optoelectronics and microsystems - EPSRC EP/W024772/1) is targeting all of these issues with the aim of enabling fully deterministic machining and further exploration of the capabilities and limits of physical machining with dicing saws.

Further work is also required on blade and machine parameter studies for all of the optical materials of interest, preferably on a next-generation machine with the features discussed previously to minimise the effects of bed, wafer, and track variation. A more extensive combination of the experiments discussed in Chapter 4 (i.e. the feed rate tests for different depths of cuts, and a more detailed parameter for blade wear) are needed for a true understanding of the blade and material interactions, enabling fully deterministic machining of photonic materials.

These improvements would enable the mass production of photonic components with accurately placed, smooth, and chip-free surfaces, without the need for physical verification steps, significantly reducing manufacturing costs and time. They would also allow highly efficient ridge waveguides to be fabricated in any optical material with the appropriate blade, enabling a wide range of wavelengths to be targeted for photonic, non-linear, and quantum applications. All of this would finally enable the passive alignment of multiple complex free-space components onto a single substrate with high precision and repeatability; i.e. multiple atom or ion traps on one substrate.

Appendix A

Publications

A.1 Journal Papers

- Paul C. Gow, Glenn M. Churchill, Valerio Vitali, Thalia Dominguez Bucio, Frederic Y. Gardes, **Matthew P. D'Souza**, Periklis Petropoulos, Corin B.E. Gawith, James C. Gates. "Mechanical dicing of optical quality facets and waveguides in a silicon nitride platform", Electronics Letters Volume 60 Issue 5, March 2024

A.2 Conference Publications

- **Matthew P. D'Souza**, Glenn Churchill, Paul C. Gow, Peter G.R. Smith, Corin B.E. Gawith, James C. Gates. "Optimisation of dicing parameters for lithium niobate ridge waveguide fabrication", SPIE Photonics West, March 2024
- Corin B.E. Gawith, Noelia Palomar Davidson, Goronwy Tawy, Glenn Churchill, **Matt D'Souza**, Paul Gow, Paolo Mennea, Peter Smith, James Gates "Developing Zinc-indiffused PPLN ridge waveguides for quantum applications in the UV, visible and mid-infrared", IEEE Summer Topicals, July 2024
- James C. Gates, Noelia Palomar Davidson, **Matthew P D'Souza**, Goronwy Tawy, Glenn Churchill, Paolo L. Mennea, Peter Iveson, Peter G.R. Smith, Corin B.E. Gawith. "Non-linear Frequency Conversion Waveguides for Quantum Technology", Europhoton, August 2024
- **Matthew D'Souza**, Noelia Palomar Davidson, Glenn Churchill, Paul Gow, Lewis Wright, Peter Smith, Corin Gawith, James Gates. "Investigation of the fabrication consistency of lithium niobate ridge waveguides formed by dicing", International Micro and Nano Engineering, September 2024

- James Gates, Paul Gow, Glenn Churchill, **Matthew D'Souza**, Peter Smith, Corin Gawith. "Micromachining via diamond grinding of photonic circuit facets", International Micro and Nano Engineering, September 2024